Experimental validation of flow and mass transport in an electrically-excited micromixer

Dissertation, presented to
the Faculty of Mechanical Engineering
of the University Karlsruhe
for obtaining the academic degree

of Doctor of Engineering Sciences (Dr.-Ing.)

from

M.Sc. Hamid Farangis Zadeh

born in Sanandaj, Iran

Date of oral examination: May 30, 2005

Chairman: Prof. Dr.-Ing. H.-J. Bauer

First examiner: Prof. Dr.-Ing.habil. P. Ehrhard

Second examiner: Prof. Dr.rer.nat. V. Saile

Dedicated to Our Father

Prophet Iqbal Shábani

تقدیم بہ پدرمان

حضرت اقبال شعبانی

او دلیل نور و نور از بود او

عالمین منت گذار جود او

Abstract

Experimental validation of flow and mass transport in an electrically-excited micromixer

The experimental validation of the flow and mass transport within an electrically-excited micromixer, as proposed by (Meisel and Ehrhard 2005) on the basis of a theoretical model, is the focus or the present work. For the (local) measurement of the flow field within the micromixer we engage the micro particle image velocimetry (μPIV), proposed by (Meinhart, Wereley and Santiago 1999). For the measurement of the height-averaged concentration field we develop a micro laser-induced fluorescence (μLIF) technique (cf. (Matsumoto, Farangis Zadeh and Ehrhard 2005)).

The experiments reveal for pure pressure-driven flow, particularly at larger Reynolds numbers, secondary motion within the meander in form of so-called Dean vortices, which significantly affect mass transport. If, additionally, electroosmotic forces act on the flow, we can even in straight channel cross sections resolve complex velocity profiles, which are dominated by electoosmosis close to walls and by the applied pressure difference in the channel centre. Hence, even flow at walls against the pressure-driven main flow can be observed. Particularly within bends a complex flow structure is found, which has successfully been characterized by a number of vortex and saddle lines. A characterization of the overall mixer performance is, finally, obtained from the measured concentration fields, which allow at both the inlet and outlet cross sections to infer the so-called mixing quality. This measure indicates a substantial improvement of mixing due to the electrical excitation.

Experimentelle Validierung der Strömung und des Stofftransports in einem elektrisch erregten Mikromischer

Im Mittelpunkt der vorliegenden Arbeit stehen Validierungsexperimente zur Strömung und zum Stofftransport in einem elektrisch erregten Mikromischer. Ein solcher Mikromischer ist von (Meisel and Ehrhard 2005) auf Basis eines theoretischen Modells vorgeschlagen worden. Zur Messung des (lokalen) Geschwindigkeitsfeldes verwenden wir die sog. "micro particle image velocimetry" (μPIV), welche von (Meinhart et al. 1999) vorgeschlagen wurde. Zur Messung des höhengemittelten Konzentrationsfeldes entwickeln wir eine Technik auf Basis der laserinduzierten Fluoreszenz (μLIF) (vgl. (Matsumoto et al. 2005)).

Die Messungen zeigen für eine rein druckgetriebene Strömung, besonders bei großen Reynolds-Zahlen, Sekundärströmungen innerhalb des Mäanders in Form sog. Dean Wirbel. Diese Wirbel beeinflussen den Stofftransport erheblich. Wenn zusätzlich elektroosmotische Kräfte auf die Strömung einwirken, so finden sich bereits in Querschnitten gerader Kanalteile Geschwindigkeitsprofile, welche durch die Elektroosmose in Wandnähe bestimmt sind, während in der Kanalmitte die angelegte Druckdifferenz bestimmend bleibt. So findet sich an Wänden sogar eine Strömung, die entgegen der druckgetriebenen mittleren Strömung gerichtet ist. In den Krümmern des Mäanders können wir eine komplexe Strömungsstruktur auflösen, welche erfolgreich durch eine Zahl von Wirbel- und Sattellinien charakterisiert werden kann. Schließlich gelingt auf Basis gemessener Konzentrationsfelder eine Charakterisierung des integralen Mischerverhaltens. Hierzu bestimmen wir am Eintritts- und Austrittsquerschnitt jeweils die sog. Mischungsqualität. Diese Größe belegt, dass eine substantielle Verbesserung der Vermischung durch die elektrische Erregung erreicht wird.

Contents

1 Introduction **1**

1.1 Micromixers 1

1.2 Characterization of mixers 3

2 Theoretical aspects **7**

2.1 Electrokinetics 7

2.2 Simulation of an electrically-excited micromixer 14

3 Fabrication of the microchannels **18**

3.1 Polymer chips 18

3.2 Glass chip 20

4 Experimental techniques **23**

4.1 Experimental setup 23

4.2 Electrical field 28

4.3 Micro particle image velocimetry 32

4.4 Micro laser-induced fluorescence 39

5 Results **50**

5.1 Flow and mass transport for pressure-driven flows through the micromixer . 50

5.2 Electroosmotic flow in straight microchannel 55

5.2.1 Effects of electrical field strength 59

5.2.2 Effects of pressure-driven flow strength 61

5.2.3 Effects of oscillating electrical field 62

5.3 Electrically-excited flow within the meander 64

5.4 Mass transport through the electrically-excited micromixer 69

6 Summary and outlook **75**

7 Note of thanks **78**

Bibliography **79**

Chapter 1

Introduction

This introductory chapter consists of two subchapters. In the first subchapter the types of mixers, their differences and the reasons behind the classification are introduced. This includes a survey of the literature on micromixers. The next subchapter describes the available experimental tools to evaluate mixing performance. Again a literature survey on mixer characterization and on available measuring techniques is given. Each subchapter likewise includes to some extent macroscopic views of the matter.

1.1 Micromixers

Mixing is not only a natural phenomenon accompanying geophysical, oceanic and atmospheric flows (Ottino 1988, Plumb 1993); it is also an important step in many technological processes. Effective mixing is the basis of chemical (Fogler 1993) and food (Blakebrough 1967) processes in industry, of chemical analysis systems (Kateman and Buydens 1993), of combustion engines (Kuo 1986), and multiple other processes (Radovanovic 1986). Mixing is required to make glass (West 1984), polymer blends (Charrier 1996), and pharmaceutics (Walsh 1998). The majority of industrial processes are carried out on a macroscopic scale. There are few cases where mixing is used to obtain homogenously-distributed liquids or gases on the molecular scale (Oldshue 1983, Hu and Koochesfahani 2002). In recent years the mixing of small quantities of liquids has become technologically relevant in the context of microfluidics (Nguyen and Werely 2002), of micro total analysis systems (μTAS) (Legge 2001, Auroux, Iossifidis, Reyes and Manz 2002, Reyes, Iossifidis, Auroux and Manz 2002), and of micro synthesis and total analysis systems (μSYNTAS) (Mitchell, Spikmans, Bessoth, Manz and de Mello 2000). Theses systems not only allow performance more operations (synthesis and analysis) per time, they moreover consume fewer reagents and produce less waste at reduced energy consumption (Ramsey 1999). To reduce the

analysis and reaction time in μTAS and μSYNTAS, fast mixing of sample solution and reagent is one of the key steps (Kakuta, Bessoth and Manz 2001). Miniaturized mixers are not only used in kinetics studies (Floyd, Schmidt and Jensen 2001) and rapid chemical reactions (Hinsamann, Frank, Svasek, Harasek and Lendl 2001), they are also inseparable parts in biomedical and chemical processes (Liu, Kim and Sung 1993) and chemical sensing (Weigl, Holl, Schutte, Brody and Yager 1996, Veenstra, Lammerink, Elwenspoek and van den Berg 1999). For routine tasks, commercial micromixers are available on the market and their performance is well documented (Knight 2002).

Mixing comprises three mechanisms of mass transport: molecular diffusion, eddy diffusion and bulk convection. On the macro scale, turbulence can generate fluctuations, which lead to an intensified transport, the so-called eddy diffusion. In some distance from walls, this mechanism dominates over molecular diffusion (Lu, Ryu and Liu 2002). Further, we have convective transport of fluid elements. During transport these elements are stretched and folded, so that the length scale of segregation, i.e. the thickness of lamellae of species, decreases. Finally, on the small scale molecular diffusion degrades segregation (Kling and Mewes 2003), and hence completes mixing. On the micro scale mixing is more difficult. Although diffusion on the micro scale is effective, Reynolds numbers are typically small and the flows remain laminar. In the absence of turbulence and stirring, both eddy diffusion and bulk convection are limited, and hence, the interfacial area for molecular diffusion remains limited. Under such conditions time inefficiency becomes a major problem (Chiem, Colyer and Harrison 1997). To overcome this difficulty, imposed by the laminarity of microflows, numerous and often ingenious micromixers have been developed (Campbell and Grzybowski 2004).

Basically micromixers fall into two categories: passive mixers and active mixers (Robin, Stremler, Sharp, Olsen, Santiago, Adrian, Aref and Beebe 2000). Based on the nature of the mixing process, a categorization into static and dynamic mixers is likewise reasonable (Nguyen and Werely 2002). Passive mixing refers to processes, in which the interface between the fluids being mixed is a consequence of the flow, driven through channels of fixed geometry. Hence, passive mixers achieve mixing by virtue of their topology alone (Miyake, Lammerink, Elwenspoek and Fluitman 1993, Mensinger, Richter, Hessel, Döpper and Ehrfeld 1994, Branebjerg, Gravesen, Krog and Nielsen 1996). Repeated lamination and splitting of flows in 20-50 μm wide channels, e.g. has been used to increase the interfacial area, and thus the mixing efficiency (Schwesinger, Frank and Wurmus 1996, Ehrfeld, Golbig, Hessel, Lowe and Richter 1999). Mixing times below 100 s with fast diffusion in nozzles of a few micrometers diameter are reported by (Chaté, Villermaux and Chomez 1996, Knight, Vishwanath, Brody and Austin 1998). However, in these devices mixing is achieved at the cost of large pressure drop and potential channel clogging. The application of so-called

Lagrangian chaos or chaotic advection is a further possibility. Such a mechanism occurs even in smooth and regular flow fields (Ottino 1988) and allows to disperse fluids effectively. Three-dimensional chaotic mixing, using serpentine and twisted channels, has been achieved by (Bertsch, Heimgartner, Cousseau and Renaud 2001, Park, Kim, Park, Chung, Chung and Chang 2004). To develop strong chaotic advection, it is usually necessary to rely on complex three-dimensional microstructures, which are rarely appropriate for cheap mass production, and hence, remain limited to research applications. Recently, a relatively-simple passive micromixer with bas-relief structures has been developed by (Stroock, Dertinger, Ajdari, Mezic, Stone and Whitesides 2002).

Active mixing refers to processes in which the interfaces interact with the flow and modify it (Chaté et al. 1996). Active mixers either do have moving parts or use externally-applied forcing via e.g. pressure or electromagnetic fields (Evans, Liepmann and Pisano 1997, Lee, Tabling, Shih and Ho 2000, Oddy, Santiago and Mikkelsen 2001). Active mixing is usually achieved by periodic perturbation of the flow field. In time-dependent flows, chaotic advection may also be engaged to improve mixing. Several fluid actuation methods have been demonstrated, including heat pulses (Choi and Ahn 2000), differential pressure variations (Hosokawa, Fujii and Endo 1999, Deshmukh, Liepmann and Pisano 2001), ultrasonic and piezoelectric actuation (Moroney, White and Howe 1991, Zhu and Kim 1998, Woias, Hauser and Yacoub-George 2000), evaporation (Evans et al. 1997, Tsai and Lin 2001), magnetic actuation (Suzuki and Ho 2002), and electrokinetic actuation (Lee, Deval, Tabling and Ho 2001, Meisel and Ehrhard 2005). One important advantage of active mixers is that they can be activated when needed. Furthermore, time and length of the channel, required for mixing, are clearly reduced against passive mixers (Park et al. 2004). On the other hand, active mixers require external power and control.

For the prediction of mass transfer and reaction progress in micromixers, several models and simulations are in literature (Hong, Thiffeault, Fréchette and Modi 2003, Jen, Wu, Lin and Wu 2003, Wang, Iovenitti, Harvey and Masood 2003, Meisel and Ehrhard 2005). Beyond the pure theoretical simulation, several concepts have been verified experimentally, namely (Zalc, Szalai, Muzzio and Jaffer 2002b, Bottausci, Cardonne, Mezic and Meinhart 2003, Hong, Choi and Ahn 2004, Wong, Ward and Wharton 2004b).

1.2 Characterization of mixers

The experimental characterization of liquid mixers on the macro scale in most publications relies on the measurement of (Oldshue 1983):

- power consumption (Hari-Prajitno 1999),

- pressure drop (Zalc et al. 2002b),
- concentration (Zhang, Schneider and Collicott 1995),
- temperature (Hatch, Sowa, Samuelson and Holdeman 1995),
- velocity (Olsen and Dutten 2003).

All these quantities somehow reflect the mixer performance and, from their measurement results other parameters like mixing time or mixing quality can be inferred. For instance, from velocity field information or from concentration field information, the mixing quality can be inferred. Mixing time is defined as the time required to obtain a defined mixing quality. Hence, mixing time in all cases relies on of mixing quality. Mixing quality, in general, is defined based on the difference of the real concentration field and the ideal (perfectly-mixed) concentration field. Hence, concentration field measurements are the most natural access to mixing quality. Direct measurements of the concentration field involve colorimetric methods, which rely on color species (Melton, Lipp, Spradling and Paulson 2002), or distributed (local) sensors within the mixer (Espinosa-Solares, Brito-De la Fuente, Tecante, Medina-Torres and Tanguy 2002).

The power consumed by a mixer is typically obtained from impeller torque, impeller shaft speed and measurements of electrical power, consumed by motors or pumps (Oldshue 1983). These methods have little effect onto the flow in the mixer and no contact of measuring device and fluid is needed. Thermocouples and thermistors are common tools for measuring temperatures in mixers (Maruyama, Suzuki and Mizushina 1981, Espinosa-Solares et al. 2002). They offer point measurements and a direct contact with the flow is needed, with possible effects onto the flow. For an electrolyte, concentration measurements in mixers can also be based on capacitive methods (Kramers, Baars and Knoll 1953). Electrical resistance tomography likewise allows the measurement of concentration fields (Holden, Wang, Mann, Dickin and Edwards 1998). Unfortunately, both of these methods introduce perturbations into the flow, are expensive, and have limited resolution (Zalc, Szalai, Alvarez and Muzzio 2002a). Optical techniques such as the Schlieren technique (Dalziel, Hughes and Sutherland 2000) or laser-induced fluorescence (LIF) (Koochesfahani and Dimotakis 1986) are other methods to visualize or measure concentration fields in liquid mixers. These optical methods are typically non-intrusive. For the measurement of fluid velocities in mixers, methods such as Pitot tubes (Oldshue 1983) and hot-wire anemometry (Bakker, LaRoche and Marshall 1998) are typically applied. In all cases a direct contact of flow and probe is necessary and point information on the velocity is obtained. Streak line photography, laser Doppler anemometry (LDA), and particle image velocimetry (PIV) (Oldshue 1983)

are the most common optical measuring techniques for the flow (field) in mixers. For streak line photography, small particles are added to the mixing liquids. Photographs with known exposure time, illuminated by a light sheet, allow determining the lengths of particle paths and averaged velocities fields in the respective plane can be inferred. This method is of limited value, since optical access from several sides is needed and the technique lacks high accuracy. LDA uses the Doppler frequency shift of scattered light from moving particles in the fluid. This technique provides highly-accurate data on the local velocity (point measurement), and two-dimensional and three-dimensional velocity vectors can be measured with very little disturbances to the flow (Oldshue 1983). The major disadvantages of LDA are the high costs and the time, required to pointwise scan velocity fields. PIV relies on a similar principle as streak line photography. For PIV, the movement of particles within a light sheet is recorded at two times, with an appropriate time interval between the images. Statistical methods (cross correlation) allow determining the average particle movement at a specific location. Hence, two-dimensional (and even three-dimensional) velocity fields are captured instantaneously. While PIV has advantages over LDA with regard to field measurements and lower costs, it does not provide such a high temporal resolution as LDA.

For micromixers, field measurements of velocity and concentration are essential for characterization. The size of sensors in comparison to the width of the microchannels, generally excludes intrusive measuring techniques for such investigations. It appears, therefore, mandatory to apply non-intrusive experimental techniques to analyze the flow and transport phenomena in such small devices. Moreover, full-field measurements are of advantage, as they provide detailed information on the entire device at the cost of reduced temporal resolution. High temporal resolution is typically not an important aspect in such small-scale (laminar) flows. In recent years some macroscopic field measurement techniques have been adapted to microchannels. Even though, optical point measuring techniques such as LDA can be miniaturized to some degree, the size of the measuring volume remains relatively large and limits the number of fringes (Nguyen and Werely 2002). Hence, the accuracy of a μLDA system remains limited. More promising methods for flow field measurements involve the scalar image velocimetry (SIV), the molecular tagging velocimetry (MTV), and the microscopic particle image velocimetry (μPIV) (Meinhart, Wereley and Santiago 2000b). SIV images the transport of a passive scalar and, from an inversion of the transport equation, the velocity field can be inferred (Nguyen and Werely 2002). SIV takes advantage of molecular tracers, which should remain strictly passive within the flow. Any interaction of the tracers with the solid structure, with force fields, or strong diffusion can significantly lower the accuracy and spatial resolution of the measurements. The spatial resolution can reach about 20 μm (Paul, Garguilo and Rakestraw 1993). For MTV particular fluorescent or phosphorescent molecules are excited by a pattern of light, e.g. a line or a grid projected

into the flow. After excitation the pattern is imaged twice at a known time interval. Cross correlation of the patterns, afterwards, allows the patterns to infer the local velocity vectors (Gendrich, Koochesfahani and Nocera 1997). In principle, MTV can be used within microchannels at a spatial resolutions of about ten micron (Meinhart et al. 2000b). μPIV is a conventional PIV system, which additionally involves a microscope, volume illumination, and fluorescent seeding particles. Fluorescent techniques, hereby, allow for the separation of the weak light from the (small) particles, guarantee a high signal-to-noise ratio, and hence improve the spatial resolution (Meinhart et al. 1999). μPIV offers detailed two-dimensional velocity field measurements at spatial resolution of about one microns (Meinhart, Wang and Turner 2003). μPIV allows the inference velocity field data from different depths of a microchannel, hence provides two components of the velocity field in the entire fluid volume.

There are several articles in the literature, addressing to some extent the measurement of concentration fields in microchannels. (Gaskey, Vacus, David, Villermaux and André 1990) engage a fluorescence technique to capture local and time-dependent concentration in a 30 μm-diameter test volume of liquid in a turbulent macroscopic flow. Such a technique could be applied to microflows to capture averaged concentration in microchannels. (Oddy et al. 2001), through a microscope, use epi-illumination to obtain qualitative information on concentration fields in micromixers. (Holden, Kumar, Castellana, Beskok and Cremer 2003) use two fluorescent dyes to (qualitatively) visualize a fixed concentration array, achieved in a number of parallel channels. (Yamaguchi, Takagi, Yamashita, Nakumura, Maeda, Sotowa, Kusakabe, Yamasaki and Morooka 2004) and (Park et al. 2004) use confocal microscopy to infer fluorescence intensity patterns in cross sections of a meander channel and qualitatively compare to computational concentration fields. (Fletcher, Haswell and Zhang 2003) rely on a Raman microscope spectrometer to monitor concentration fields of various reactants in a microreactor. It is, however, evident from most of the above articles that qualitative rather than quantitative information on the concentration fields is obtained.

Chapter 2

Theoretical aspects

In this chapter the theoretical background of electrokinetics and its applications are discussed. The chapter is divided into two subchapters namely electrokinetics and electrically-excited micromixer. The basic concepts of electrokinetics will be introduced in the first subchapter. The next subchapter covers the simulation studies and related results, which have to be validated experimentally.

2.1 Electrokinetics

Most of the systems in microfluidics need selected fluid or particle motion to perform for example fluid delivery, droplet creation, mixing or separation. In some cases such actions have to be controllable. Due to reduction in length scale some of the techniques used in conventional laboratories become ineffective and can not be simply transferred into microfluidic systems. Electrokinetics is especially effective on the microscale. For instance, since pressure-driven flows in microchannels cause high velocity gradients and increase dispersion, transport can be accomplished by electrokinetic-based techniques without such drawbacks. Generally, electrokinetic phenomena (Probstein 2003) relate to the motion of fluids, subjected to an (external) electrical field. First of all the concept of an electrical double layer (EDL) has to be discussed. Most substances acquire electrical charges at their surface when brought in contact with an electrolyte. The effect of any charged surface is to influence the distribution of the nearby ions in the electrolyte. Counterions (ions of opposite charge to that of the surface) are attached to the surface while coions (ions of like charge) are repelled from the surface. The EDL is a region close to the charged surface in which there is an excess of counterions to neutralize the surface charge, and these ions are distributed in a diffuse manner. Evidently there is no electrical neutrality within the EDL because the number of counterions is large compared to the number of coions (Probstein 2003). These

counterions form an inner and an outer layer, termed Stern layer and Gouy-Chapman layer (Adamson and Gast 2004). The immobile counterions adsorbed at the surface form the Stern layer. The Gouy-Chapman layer comprises the diffuse and mobile counterions, which are set in motion upon the application of an external electric field. In models of the EDL the shear plane, which separates the Stern and Gouy-Chapman layers, coincides with the plane where the fluid obeys the no-slip condition. The electrical potential at this plane is called zeta potential, ζ. Fig. 2.1 presents (a) the structure of the EDL at a negatively charged wall, (b) the electrical potential associated with the EDL. The magnitude of the electrical potential decays with increasing distance from the wall to zero, so that the bulk fluid far from the wall is electrically neutral.

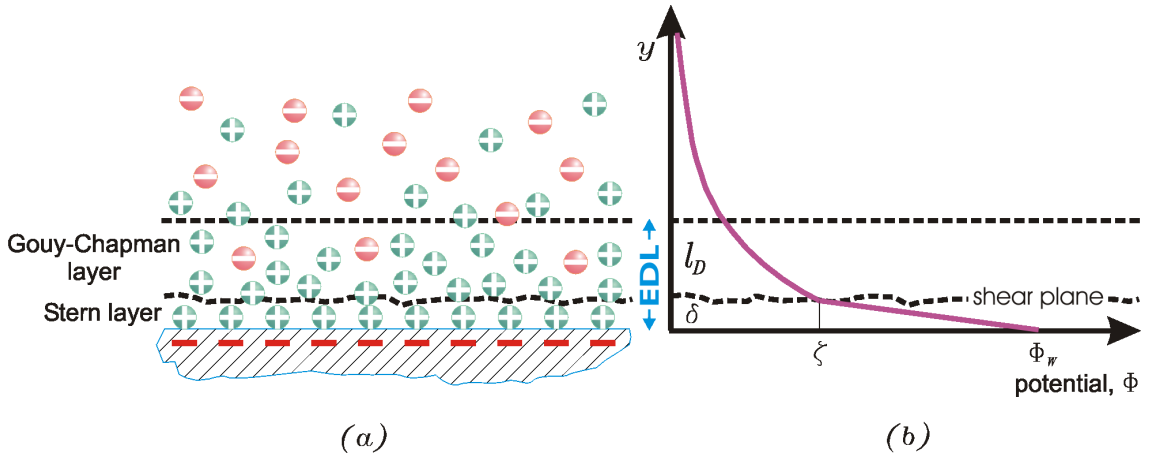

Figure 2.1: (a) EDL, Stern and Gouy-Chapman layers at a negatively-charged wall, (b) electrical potential versus distance from the wall.

Following (Probstein 2003), the conditions within the EDL (precisely in the Gouy-Chapman layer) can be quantified. For this purpose the so-called Debye-Hückel approximation is invoked. We discuss these conditions for the simple case where two types of ions with opposite charges and identical valence are present. The Debye-Hückel approximation assumes a statistical (Boltzmann) distribution of these ions in wall-normal direction, hence there is a dilute concentration of these ions, in conjunction with electrical neutrality far away from the wall. Given these assumptions, the electrical potential ϕ, which is dependent only on the wall-normal coordinate y, can be described by the Poisson equation

$$\frac{d^2\phi}{dy^2} = \frac{Fzc}{\epsilon\epsilon_0}, \tag{2.1}$$

where F is the Faraday's constant, z is valence number, c is the molar ion concentration

and $\epsilon\epsilon_0$ is the dielectric property of the electrolyte. For small zeta potentials (typically $\zeta < 25\ mV$), a simple solution can be derived for the above Poisson equation

$$\phi = \phi_W \exp(-\frac{y}{l_D}) \tag{2.2}$$

for the wall-normal variation of the electrical potential. Here, ϕ_W is the potential at the wall (precisely at the shear layer) and l_D is the Debye length. The Debye length can be expressed as

$$l_D = \sqrt{\frac{\epsilon\epsilon_0 \mathbb{R}T}{2F^2 z^2 c}}, \tag{2.3}$$

where $\mathbb{R}$ is the gas constant and T is the actual temperature.

To summarize, at electrically-insulating walls adjacent to a liquid containing ions (electrolyte) one can expect an electrical double layer. Such a layer has roughly a thickness of l_D, whereas the electrical potential decreases exponentially from its value at the wall towards zero in the (electrically-neutral) bulk of the liquid. Therefore, this layer is electrically not neutral and allows for electrical forces.

We shall now discuss phenomena, which may develop as consequence of electrical double layers. These phenomena can be classified into seven types (Probstein 2003, Wong, Wang, Deval and Ho 2004a). In the following these types and their applications are reviewed.

I. Electroosmosis is the movement of a liquid (within a microchannel) due to the application of an external electrical field. The electrical field is applied parallel to the channel axis, as shown in Fig. 2.2. Electroosmotic flow typically exhibits a plug-like velocity profile (Fig. 2.2). The Helmholtz-Smoluchowski relation provides the amplitude u_{eo} of the electroosmotic (axial) velocity. The equation of motion for an incompressible liquid at a low Reynolds number, which is typical for microflows, and in the absence of a pressure gradient is

$$\mu \nabla^2 \mathbf{u} = -\rho_E \mathbf{E}, \tag{2.4}$$

where $\mathbf{u}$ is the velocity vector, μ is viscosity, ρ_E is electrical charge density, and $\mathbf{E}= (E_x, E_y)$ is the applied electrical field. For a long slender channel we have $v \ll u$, and together with the relation between the electrical charge density and the electrical potential we obtain the one-dimensional approximation

$$\mu \frac{\partial^2 u}{\partial y^2} = \epsilon \epsilon_0 \frac{\partial^2 \phi}{\partial y^2} E_x. \tag{2.5}$$

Here, x and y are wall-tangential and wall-normal coordinates, u is the (wall-tangential) axial velocity component, and E_x is the axial component of the electrical field vector (Fig. 2.2).

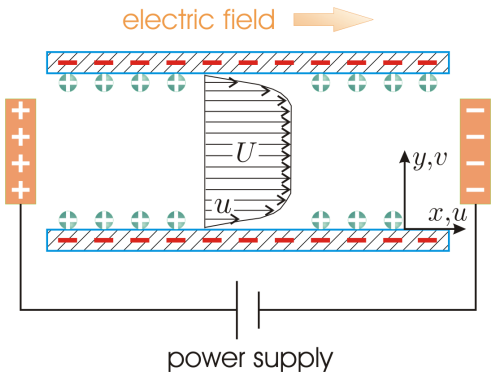

Figure 2.2: Electroosmotic flow of liquid within a channel subjected to an external electrical field.

Eq. (2.5) can be solved under the no-slip condition at the wall ($y = 0, u = 0$) and a shear-free flow condition far away from the wall ($y \to \infty, \partial u/\partial y \to 0$). Furthermore, Eq. (2.2) serves to determine the electrical potential ϕ. Therefore, the electroosmotic velocity u_{eo} can be obtained from the solution $u(y)$ as

$$u_{eo} = u(y \to \infty) = -\frac{\epsilon \epsilon_0 \zeta E_x}{\mu}. \tag{2.6}$$

The electroosmotic mobility (u_{eo}/E_x) and the zeta potential ζ are two important parameters for the characterization of electroosmosis. For cases where Joule heating is negligible, the electroosmotic mobility is considered to be constant for a given wall material and liquid (electrolyte). This is equivalent with a constant zeta potential and constant material properties ϵ, μ. The zeta potential, hereby, can be measured indirectly using velocity or flow rate measurements. Once u_{eo} is measured with a known electrical field strength E_x and material properties ϵ, ϵ_0, and μ, the zeta potential can be readily inferred. For example with a typical zeta potential of about $\zeta = 100\ mV$ and an electrical field of $E_x = 1\ kV/m$, we obtain (using water) an electroosmotic velocity of $u_{eo} = 0.1\ mm/s$, a fairly small value. Electroosmotic flow is commonly used for sample injection in electrophoretic separation devices (Yang, Fu and Lee 2002). Further, using silica particles, packed in a fused silica capillary, helps in porous glass structures to provide a high surface-to-volume ratio,

and to maximize the electroosmotic effect for pumping applications (Zeng, Chen, Jr. and Santiago 2001). Glass is a typical material used in electroosmotic devices as it typically exhibits a large zeta potential in contact with common liquids. Recently, modern fabrication techniques have been applied to produce such devices on polymeric materials, and electroosmotic flow in polymers has been likewise investigated (Henry, Waddell, Shreiner and Locascio 2002). Electroosmosis has also been used to generate instabilities within mixing flows on the micro scale. Active micromixers made of glass and polymers based on such instabilities are presented by (Oddy et al. 2001). Electroosmosis also has been used for dewatering of soils, mine tailings and waste sludge (Probstein 2003). The above phenomenon of electroosmosis is likewise termed DC electroosmosis.

Electroosmosis at high-frequency alternating electrical fields (up to 1 MHz) is likewise observed (Wong et al. 2004a, Ramos, Morgan, Green and Castellanos 1998). The origin of AC electroosmosis is similar to DC electroosmosis. The forces onto the liquid within the EDL do not act in an EDL at passive walls (as in DC electroosmosis) but in the EDL at the electrode. The electrodes, however, change their polarities at high frequency. Since both the direction of the electrical field and the polarity of charges within the EDL are oscillated at high frequency, the direction of the driving force remains unaffected by such oscillations. Forces within the EDL at electrodes are typically directed tangential towards the center of the electrodes, due to the electrical field, setup between two electrodes. This leads e.g. to double-vortex flows over the electrode, with the potential to aggregate specific species above the center of the electrode. The effect has a strong dependency on the applied oscillation frequency and conductivity (ion strength) of the liquid. The applied voltage is much lower than for DC electroosmosis, which is of advantage with regard to possible electrolysis.

II. Electrophoresis is the motion of charged particles in a liquid, subjected to an external electrical field (Fig. 2.3). This movement can be classified into two regimes, based on the particle size compared to the Debye length. The first regime deals with ions whose diameter is much smaller than l_D. The motion of such particles can be described by a simple balance between electrostatic forces and viscous drag forces associated with the size of the particles.

The electrophoretic velocity u_{ep} of such small particles is a function of the effective diameter of the particles d, their total charge q, the liquid viscosity μ, and the applied electrical field E as given by

$$u_{ep} = \frac{qE}{3\pi\mu d}. \tag{2.7}$$

Typically, for d the Stokes diameter, i.e. the diameter of a sphere of equal drag, in this equation is used. The quantity $q/3\pi\mu d$ or μ_{ep} within Eq. (2.7) is usually termed electrophoretic

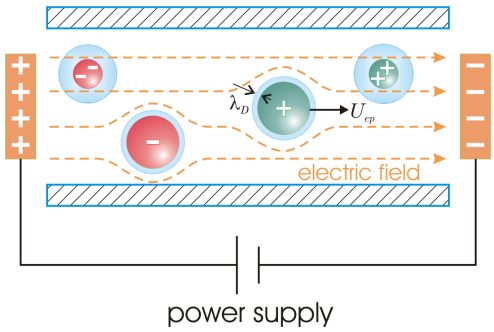

Figure 2.3: Electrophoretic motion of particles within a capillary, subjected to an external electrical field.

mobility. The second regime relates to electrophoresis of relatively large particles, e.g. large solid particles, compared to the Debye length. Here, u_{ep} is affected by the electrostatic forces due to the surface charge and due to the electrical double layer, and the viscous drag associated with both the motion of the particle and the ionic cloud around the particle. For large particles, the ionic cloud around particle can be approximated by the EDL relations for a flat plate (Eqs. (2.1-2.3)) and the electrophoretic velocity for such a situation becomes

$$u_{ep} = \frac{\epsilon\epsilon_0\zeta E}{\mu}. \tag{2.8}$$

Both Eq. (2.7) and Eq. (2.8) demonstrate the direct proportionality between electrophoretic velocity u_{ep} and applied electrical field E, which defines the electrophoretic mobility μ_{ep} in the form

$$\mu_{ep} = \frac{u_{ep}}{E}. \tag{2.9}$$

The most common application of electrophoresis is the separation of particles ranging from simple ions to large molecules like DNA or protein. This separation is typically achieved by the so-called capillary electrophoresis (Beale 1998). In addition to the separation of particles, electrophoretic forces can also position molecules to desired locations with properly designed devices (Wang, Wong and Ho 2002).

III. Dielectrophoresis is the movement of polarizable particles, suspended in a polarizable liquid, both subjected to a diverging electrical field (Pohl 1978). If the particles are more polarizable than the liquid, a motion of the particles towards the higher-field-strength region is induced. This is called positive dielectrophoresis. In the opposite case (negative dielectrophoresis) the movement is towards the lower electrical field strength.

Dielectrophoresis has been employed for variety of tasks, e.g. manipulation and translation of submicron objects (Hughes, Morgan and Rixon 2001). Translational motion generated

by dielectrophoresis can also be used to enhance mixing in microflows (Deval, Tabeling and Ho 2002).

IV. Electrothermal flows arise from temperature gradients in the liquid, generated by Joule heating. Temperature gradients induce local changes in electrical conductivity, permittivity, viscosity, and density of the solution, which in turn can generate forces that act on the bulk fluid (Melcher and Firebaugh 1967). Conductivity gradients, for example, produce free-volume charges and Coulomb forces while a permittivity gradient produces dielectric forces. The temperature rise can be estimated by

$$\Delta T \sim \frac{\sigma V_{rms}^2}{k}, \tag{2.10}$$

where σ is the electrical conductivity, V_{rms} is the root mean square voltage and k is the thermal conductivity. Based on this phenomenon, micropumping, e.g. by an arrangement of Peltier- and thermistor-elements into a semiconductor surface has been achieved (Fuhr, Schnelle and Wagner 1994).

V. Electrowetting is the modification of the surface property of a dielectric film (between a hydrophobic and a hydrophilic state) by means of an electrical field (Moon, Cho, Garrell and Kim 2002). Contact angles of liquid droplets on surfaces can be controlled by an electrical potential, according to the Lippman-Young equation

$$\cos\theta_V - \cos\theta_0 = \frac{\epsilon\epsilon_0 V^2}{2\gamma t}, \tag{2.11}$$

where θ_V is the contact angle due to an applied electrical potential V, θ_0 is the contact angle in the absence of an electrical field, γ is the surface tension at the liquid/gas interface, t is the thickness of the insulating layer, and $\epsilon\epsilon_0$ is the dielectric property of the layer.

Electrowetting is a promising actuation technique, since it requires low power, is highly reversible, and can be used with a broad variety of fluids. Creation, transportation, cutting, and merging of liquid droplets by means of electrowetting have been reported (Cho, Moon and Kim 2003). Mixing of fluorescent dyes (Fan, Hashi and Kim 2003) and separation of particles (Cho and Kim 2003) on digital fluidic chips are other applications.

VI. Sedimentation potential is the electrical potential, which develops due to the movement of charged particles within a stationary liquid (Probstein 2003). So, it can be viewed as the opposite effect of electrophoresis.

VII. Streaming potential is the electrical potential, which develops due to the movement of liquid (and hence charges) along a charged wall. The potential gradient appears typically along the wall (Probstein 2003). This effect can be viewed as the opposite effect of electroosmosis.

2.2 Simulation of an electrically-excited micromixer

Based on a theoretical model, (Meisel and Ehrhard 2005) propose a micromixer, which takes advantage of time-dependent electroosmotic motion within microchannels. In detail, by means of two-dimensional simulations the authors investigate, how oscillatory electrical fields applied to the flow can enhance the mixing processes in microchannel. Instead of assuming electroosmotic slip at the microchannel wall or resolving the EDL by numerical methods, the proposed model by (Meisel and Ehrhard 2005) engages matched-asymptotic expansions to treat the EDL. Given the extremely thin EDL, i.e. $l_D \ll d_0$, where d_0 is channel width (Fig. 2.4), the solution for the full flow is obtained by asymptotically matching the separate solutions in the wall layer (EDL) and the channel core. For the flow field immediately at the wall (Meisel and Ehrhard 2005) find the approximation

$$u_W \cong \frac{q_W l_D E_x}{\mu}(\exp(-\frac{y}{l_D}) - 1), \tag{2.12}$$

$$v_W \cong 0, \tag{2.13}$$

with $q_W = \epsilon\epsilon_0\zeta/l_D$, the charge density (per unit area) at the wall, $\epsilon\epsilon_0$ the dielectric material constant within the liquid, ζ the zeta potential, l_D the Debye length, and μ the dynamic viscosity of the liquid. $u(W)$ and $v(W)$ are the velocity components in wall-tangential and wall-normal directions, y is wall-normal coordinate with its origin on the wall, and E_x is the local wall-tangential electrical field strength. The above velocity field corresponds to a rapid increase of the tangential velocity u_W across the Debye layer, while no normal velocity v_W is present in this layer.

This matched-asymptotic approach has been validated by (Meisel and Ehrhard 2005) for the case of a developed flow between two parallel plates. In the presence of a wall-tangential electrical field (Meisel and Ehrhard 2005) find identity between the matched-asymptotic solution and the exact analytical solution.

(Meisel and Ehrhard 2005) have designed two mixers with geometries capable to improve mixing efficiency by means of an external electrical field. Both geometries feature a Y-form mixer with different common channels. The first design, after the merging of both liquids, engages a straight common channel with a cylindrical obstacle in the middle. An oscillatory electrical field perpendicular to the main flow is applied to excite the flow around the cylinder. This yields jets emerging vertically from the cylinder walls and penetrating into the flow around the obstacle. By means of this secondary flow the virtual interface

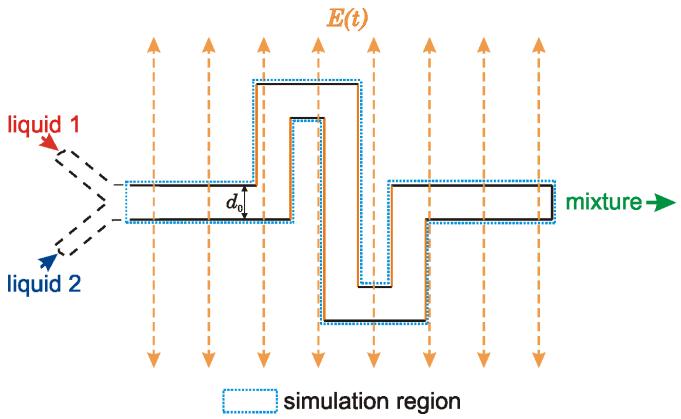

Figure 2.4: Schematics of the design for the simulation of mixing in a meander channel.

between the liquids is stretched and folded. Thus, diffusion and consequently mixing are improved. The second design engages a meander with 90° bends (Fig. 2.4) in the common channel, where both liquids meet. Here also a vertical oscillatory electrical field is applied and the forces within the EDLs at the walls parallel to the field produce jets, which penetrate into the main flow at each meander corner. This process also stretches and folds the virtual interface between the liquids, and mixing efficiency improves due to more effective molecular diffusion. We shall discuss the simulation results regarding the second (meander) mixer design in more detail, since the present experiments relate to this specific geometry.

As an example (Meisel and Ehrhard 2005) simulate the mixing process in a meander mixer made of glass with a channel width of $d_0 = 200\ \mu m$. The mixing liquids are water, the channel Reynolds number is $Re = d_0 u_0/\nu = 10$, and the Schmidt number is $Sc = \nu/D = 100$. Here, u_0 is the mean forced-flow velocity, ν is kinematic viscosity, and D represents the diffusivity of the liquids. The forced flow is chosen weak (small Re), so that a secondary flow with comparable amplitude can be easily excited. The vertical oscillatory field has an amplitude of $E_y \simeq 1200\ V/mm$ at frequency of $f = 1.4u_0/d_0$. The wall charge is assumed to be $q_W = 5 \times 10^{-3}\ C/m^2$ and the Debye length is $l_D \simeq 50\ nm$.

Fig. 2.5 presents the streamlines of the pressure-driven flow through the meander mixer without electrical excitation, at a channel Reynolds number of $Re = 10$. This flow is laminar and steady from left to right, and obviously is not appropriate for effective mixing, since the virtual interface between the liquids and diffusion remain small. Only small vortices are present in the corners, extending only into one of the liquids.

The consequence of an applied vertical oscillatory electrical field can be inspected in Fig. 2.6. Here, instantaneous streamlines of the flow during one period of electrical excitation are given. We recognize the vertical electrical field to induce (time-dependent) acceleration

of the liquid adjacent to the vertical (field-parallel) walls within the meander. This sets up a time-dependent secondary flow of comparable amplitude, which should stretch and fold the virtual interface between the mixing liquids.

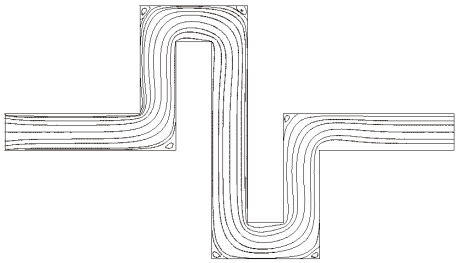

Figure 2.5: Streamlines of the laminar and steady pressure-driven flow ($Re = 10$) through the meander mixer without electrical field.

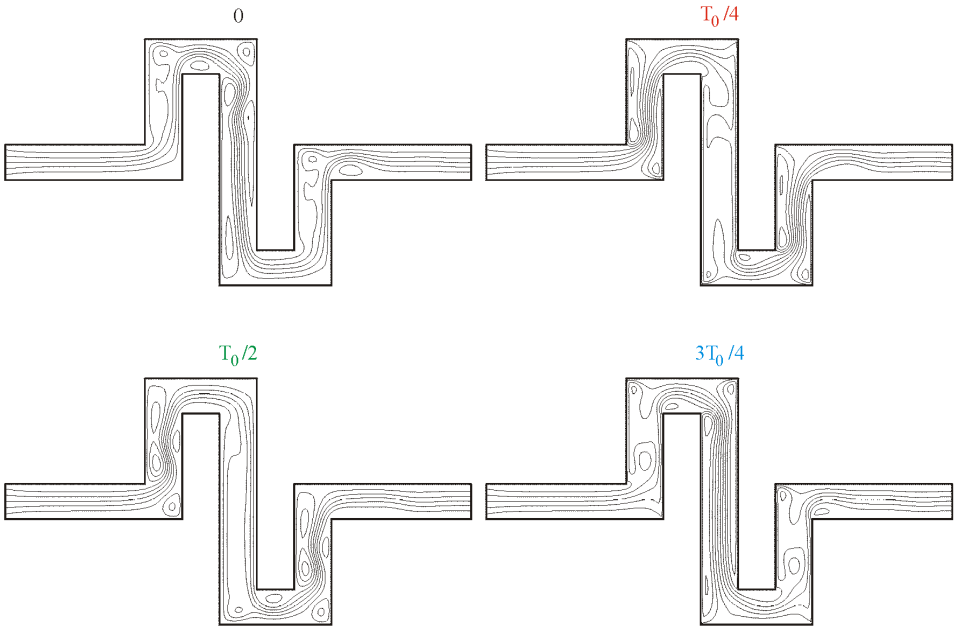

Figure 2.6: Streamlines of the unsteady flow through the meander mixer during one period (T) of electrical excitation.

(Meisel and Ehrhard 2005) have investigated the effect of the flow fields, given in Fig. 2.5 and 2.6, on the concentration field and the mixing process. In Fig. 2.7 the concentration field of the steady pressure-driven flow is given, corresponding to the flow field in Fig. 2.5. The concentration in this figure is color-coded, i.e. liquid 1 has concentration $C = 1$ and is coded in red, whereas liquid 2 has concentration $C = 0$ and is coded in blue. As the

liquids meet within the common channel, they build up a concentration boundary layer, which thickens slightly as we move downstream. Across this concentration boundary layer (formerly termed virtual interface) little diffusion and therefore little mixing occurs due to the limited area. For the electrically-excited and time-dependent flow field in Fig. 2.6, in contrast, the situation is greatly different. From the instantaneous concentration field in Fig. 2.8 we recognize that the virtual interface between both liquids is greatly stretched and folded. Hence, diffusion across this virtual interface can act effectively and leads to almost perfectly mixed liquids (corresponding to green) at the exit of the meander.

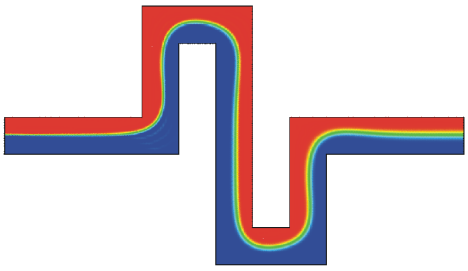

Figure 2.7: Concentration field of the steady pressure-driven flow through the meander without electrical field.

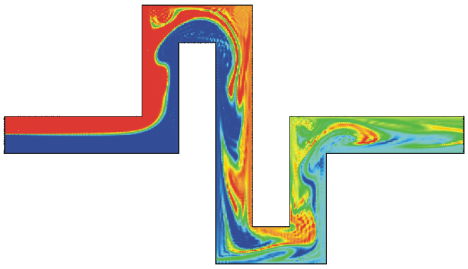

Figure 2.8: Instantaneous concentration field of the electrically-excited time-dependent flow.

It is found by (Meisel and Ehrhard 2005) that the amplitude and the excitation frequency play important role for the mixing improvement. The area of the virtual interface between the liquids can be maximized if an optimal frequency is chosen. Placing more obstacles into the common channel (first design) or adding more bends to the meander (second design) helps to increase mixing efficiency even more. Here, particularly the optimization of obstacle distance or meander length allows taking advantage of spatial resonance.

Chapter 3

Fabrication of the microchannels

In this chapter the fabrication processes of the micromixers for our experimental studies are explained. Prior to the main investigations on the electrically-excited micromixer, different types of microchannels have been tested to evaluate the selected measuring systems performances. All the necessary microchannels and electrodes are placed on chips of an area $66 \times 26\ mm^2$ (the LIGA standard format). Different optically-transparent materials are used and three types of chips are fabricated. In addition to the test chips, which are made of polymer (polysulfone, PSU) and do not contain electrodes, two other chips made of polymer and glass with electrodes are produced. This chapter is split into two subchapters, where the first subchapter explains the test chip and the applied fabrication process for the polymer chips with and without electrodes. The second subchapter discusses how the glass chip is produced.

3.1 Polymer chips

We start our experimental work by using a test chip containing different microchannels. This chip features three types of channels, namely a zigzag channel, a simple straight channel, and a Y-form mixer with a straight common channel. Fig. 3.1 presents a sketch of the test chip. All of the channels, which have trapezoidal cross section, are engraved on the chip. The mixer and the zigzag channels have a width of 90 μm at the lower and 120 μm at the upper base. The straight channel is narrower and it has a lower base width of 35 μm and an upper base width of 50 μm. All channels have the same depth of 100 μm (Fig. 3.2).

This chip is made of PSU, which is an optically-transparent polymer. The microchannels on the chip are produced by the hot embossing method. Hot embossing is a technique to fabricate high-precision and high-quality plastic microstructures (Heckele, Bacher and Müller 1998). In this method a molding tool, the so-called mold insert is pressed with high

force into a thermoplastic material, which is heated above its softening temperature. This process is performed inside an evacuated chamber. The metallic mold insert in our case has been produced by precision milling at the IMVT, an institute at the Forschungszentrum Karlsruhe (FZK). The hot embossing and covering processes have been done at the IMT, another institute at FZK.

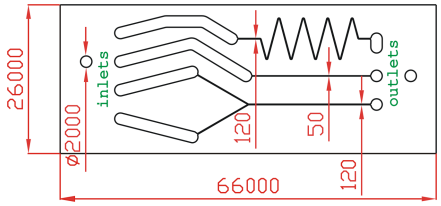

Figure 3.1: Top view of the test chip containing a zigzag channel, a straight channel, and a Y-form mixer. All lengths are given in μm.

For sealing the microchannels on this chip a thin piece of PSU with a thickness of 375 μm and identical dimensions as the chip has been chosen and by using a double-coated industrial tape (3M^{TM}) both pieces are adhered to each other. This tape (film) is optically clear and it is made of polyacrylate. A cross section of the covered channel with related dimensions is presented in Fig. 3.2.

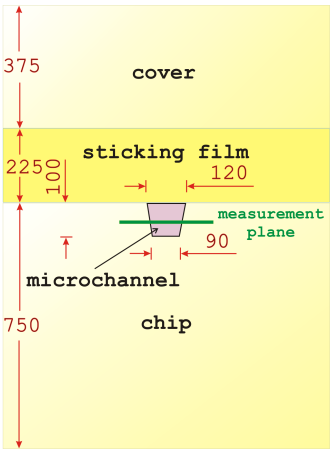

Figure 3.2: Cross-section view of the test chip, covered by a thin PSU foil to form closed microchannels. All lengths are given in μm.

The first micromixer with a meander in the middle of the common channel and two electrodes for electrical excitation is produced by the same fabrication method, namely the hot embossing technique. Two chips made of PSU and polymethylmethacrylate (PMMA) with the same thickness of 500 μm are fabricated (Fig. 3.3). The corresponding mold insert is

produced by precision diamond milling at the IMVT. For these micromixers another sealing process (Truckenmüller, Henzi, Herrmann, Saile and Schomburg 2004) is applied due to some problems with the double-coated industrial tape. In this new covering method the surfaces of the chip and the cover are modified by UV light. Subsequently, the layers are thermally bonded at moderate temperatures. For covering, a similar material as used for the chip is applied and for good optical quality a thickness of 380 μm is chosen. All these steps, namely hot embossing and covering, are performed at the IMT. The geometry of the meander is identical with the geometry engaged in the simulation, except the outer corners, which are rounded. A sketch of the meander is presented in Fig. 3.5. The channels of the micromixer have square cross sections of 110×110 μm^2 area. Two brass wire electrodes of $80\mu m$ diameter are installed within two side channels parallel to the common channel. The distance between these electrodes is 1410 μm. Prior to the sealing these wires are fixed inside the side-channels and their free ends can be accessed through two small holes in the chip. On the backside of the chip the ends of each wire are connected to the outside by an electrically-conductive glue.

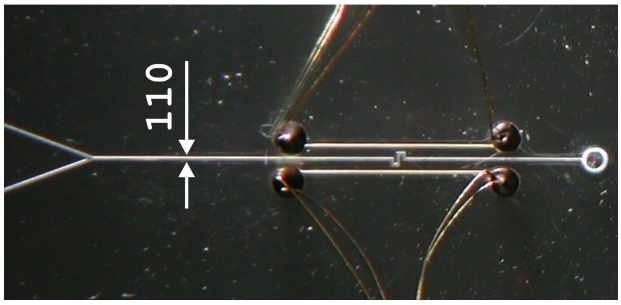

Figure 3.3: PMMA micromixer with meander channel. The brass electrodes are located parallel to the common channel.

3.2 Glass chip

The glass micromixer also has the same geometry as the polymer micromixer. It has been manufactured by *mgt mikroglas technik AG* (Mainz, Germany), a company that applies the FOTURAN selective etching process in the development of microstructured glass components. FOTURAN is a photosensitive glass, which reacts to UV light with a wavelength of around 310 nm (Freitag, Dietrich and Scholz 2000). During a lithographic process the glass is exposed through a quartz mask with a structured metal chromium layer. This mask shows the structures of the microchannels, which have to be etched into the substrate. Subsequently, the substrate is heated up to 600 $°C$, so that the exposed parts of the glass

crystallize while the non-exposed parts retain their glass structure. Finally, the crystallized parts are etched away in a solution of hydrofluoric acid (Fig. 3.4).

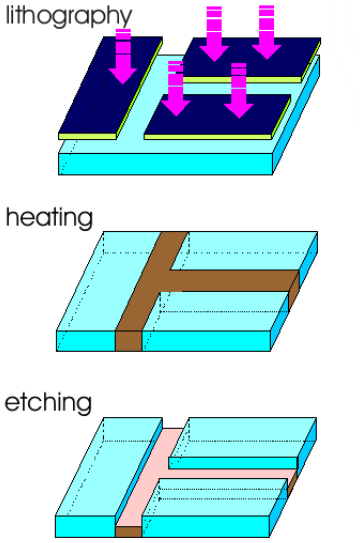

Figure 3.4: Lithography, heating and etching processes on FOTURAN. First FOTURAN glass is exposed to UV light. The exposed parts of the glass crystallize during the heat treatment. Finally crystallized parts are etched away.

In the glass chip two electrodes (two gold wires of 50 μm diameter) are placed in two side-channels and can be connected to a DC voltage supply at the chip rims (Fig. 3.5). This chip consists of three glass layers, namely cover, mixer and base. In Fig. 3.5 a sketch of the layers, their position and size is separately illustrated. A magnified view of the meander shows its geometry in detail. For producing these microchannels, the channel structures are etched into a piece of glass. Afterwards two glass layers (the cover and the base) are attached from top and bottom to the structured glass to seal the produced microchannels and to form close channels. The cover has a thickness of 1000 μm and it is made of B270 glass, which allows a good optical access. It is important to use a good transparent glass as cover, since through this part all images are taken. The mixer layer is made of FOTURAN with a thickness of 110 μm, which results in a square microchannel of 110×110 μm^2 cross section. The channels of the mixer and also the side channels for the electrodes are etched through this part. There are two larger channels connected to the Y-mixer for distributing liquids. The merging channels of the Y-mixer comprise an angle of 40° and the meander is located at distance X downstream of this junction point (Fig. 3.5). For a flexible investigation on flows at different Reynolds numbers within the meander two glass chips with different distances X, namely $X = 130$ μm and $X = 17000$ μm are employed. The base is also made of FOTURAN with 1000 μm thickness. Two inflow and one outflow holes are drilled

into the base. Besides, two larger holes are drilled through the finished chip for precise positioning on the investigation table.

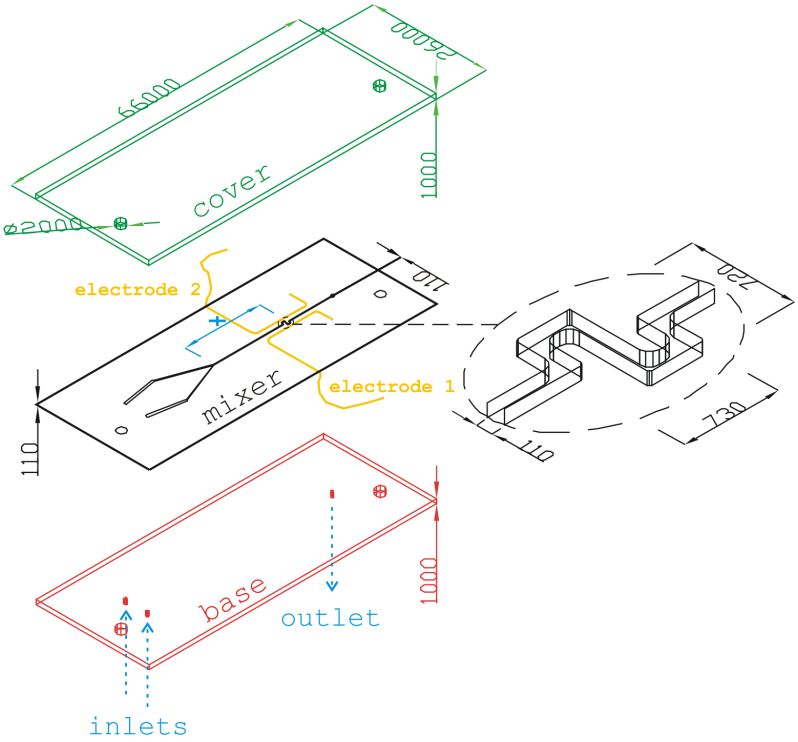

Figure 3.5: A sketch of the glass layers and electrodes used in the glass micromixer fabrication. X is the distance between the meander and the intersection of the Y-mixer. All measures are given in µm.

Chapter 4

Experimental techniques

We use two optical measuring techniques for both the velocity field and the concentration field. Based on a commercial particle image velocimetry (PIV) system, we obtain a μPIV system by incorporating a microscope and some optics in the illumination path. We further develop a micro laser-induced fluorescence (μLIF) system, based on the identical microscope and optics as engaged for the μPIV system. The light source used for the μPIV system is a double-pulse Nd:YAG laser, and for the μLIF we use a continuous-wave (CW) Argon laser. The principles of both measuring systems and their performances are separately discussed in two subchapters. Prior to these subchapters, the experimental setup and the delivery systems are introduced.

4.1 Experimental setup

Our experimental setup is presented in Fig. 4.1. To deliver liquids into the mixer, two different systems are applied to cover a wide range of Reynolds numbers. For small Reynolds numbers we engage a gravity-driven flow with the two inlet reservoirs positioned at a defined height above the outlet reservoir. For large Reynolds numbers ($Re \geq 1$), two syringe pumps are used instead. The liquids are driven through the two mixer inlet channels and leave the micromixer through the common channel. To setup the electrical field, a DC power supply and an amplifier are used, which allow to produce voltages of up to 5kV. Using a function generator in conjunction with a relay, we are able to switch polarity of the electrodes at defined frequencies. In summary, by these means an oscillating electrical field is applied to the micromixer, whereas the oscillation is in a square-signal fashion. The micromixer chip is fixed onto a PMMA connecting support by means of a PMMA cover, screws and o-rings. This support contains channels, connected to the chip for delivering and discharging the liquid.

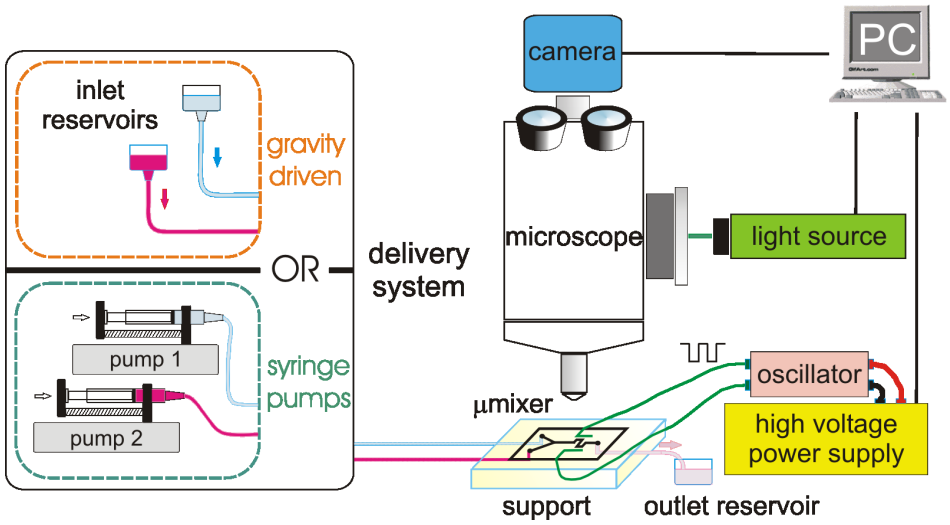

Figure 4.1: The experimental setup used for the velocity and concentration field measurements. Liquids are delivered into the micromixer by means of either syringe pumps or a gravity-driven system.

Two adjustable syringe pumps (KdScientific, USA) are applied to deliver the liquids at flow rates in the range $\dot{V} = 0.05 - 7.00\ ml/h$ with an accuracy of $\Delta\dot{V} \simeq \pm 0.03\ \mu l/h$. We use glass microsyringes (volume 10 and 50 μl) for lower flow rates and plastic syringes for higher flow rates. At very low flow rates the characteristics of the stepper motors lead to pulsating flows delivered to the micromixer. For that reason, at very low flow rates, we engage a gravity-driven system, which allows non-pulsating steady flows. Two reservoirs are connected to the inlets of the micromixer and one reservoir to the outlet (Fig. 4.1). Both pumping systems have been tested by means of a precision balance (Sartorius). This balance has an accuracy of $\pm 0.01\ mg$ and it is able to communicate via a RS232 serial interface (Fig. 4.2) with LabVIEW, the applied data processing software (National Instrument, USA). After converting the measured mass flow rates to volumetric flow rates, the volumetric flow rates are compared to the preset flow rates of the syringe pumps. The agreement is better than 99.98 % for the glass syringes and better than 99.95 % for the plastic syringes.

The gravity-driven delivery system is calibrated by mass flow measurement at several flow rates. Firstly, in the outlet reservoir the evaporation rate of water is measured (Fig. 4.3). Secondly, after connecting all reservoirs the levels of the inlet reservoirs are adjusted at different heights above the outlet reservoir, namely in the range $0 \leq \Delta h \leq 100\ mm$. Fig. 4.3 presents the measured mass for a period of 1252 seconds at several water levels Δh. The data are already corrected by the evaporation rate, such that e.g. for $\Delta h = 0$ a constant mass is observed. We clearly recognize that in all cases a smooth steady flow (straight

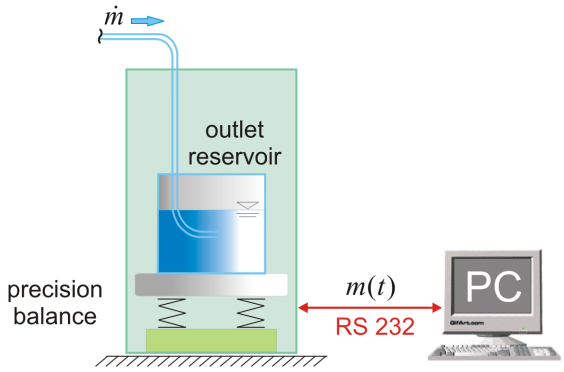

Figure 4.2: By a precision balance the mass flow rate delivered by both pumping systems is measured.

lines in Fig. 4.3), whereas from the slope the (constant) mass flow rate, $\dot{m}$ can be easily inferred. Based on the mass flow rates, $\dot{m}$, other parameters such as the volumetric flow rate $\dot{V} = \dot{m}/\rho$ ($\rho_{water(25°C)} = 0.99707\ g/ml$) and Reynolds number can be calculated. The Reynolds number for a rectangular channel is

$$Re = \frac{u_{mean} d_h}{\nu}, \tag{4.1}$$

where u_{mean} is the mean velocity in the microchannel, $d_h = 2d_1d2/(d_1+d2)$ is the hydraulic diameter of the channel and ν is the kinematic viscosity ($\nu_{water(25°C)} = 0.893 \times 10^{-6}\ m^2/s$). The Reynolds numbers obtained for different water levels Δh are plotted in Fig. 4.4. We recognize at good accuracy a linear dependency.

For optical access an inverted microscope (Leica DMIRM, Germany) is selected. Air microscope objectives (Leica) with different magnification (M), numerical aperture (NA), and appropriate for fluorescence measurements are applied. Table 4.1 presents the applied objectives, relevant NA, and depth of field (d_{total}) for each case. The depth of field of a standard microscope objective is given (Inoué and Spring 1997) by

$$d_{total} = \frac{\lambda_{emi} n}{NA^2} + \frac{en}{M\ NA}, \tag{4.2}$$

where n is the refractive index of the medium between the meander channel and the objective, λ_{emi} is the wavelength of the light imaged by the optical system in vacuum, and e is the smallest distance, which can be resolved by a detector located in the image plane of the microscope. In our case $n_{air} = 1.00$, $\lambda_{emi} = 610\ nm$, and $e = 6.45\ \mu m$.

Inside the microscope a combination of a green filter, a red filter, and a beam splitter build up an epi-fluorescent imaging system (Fig. 4.5). Through the green filter only green illuminating light (λ_{ill}) passes and e.g. the surrounding light is blocked. The beam splitter guides

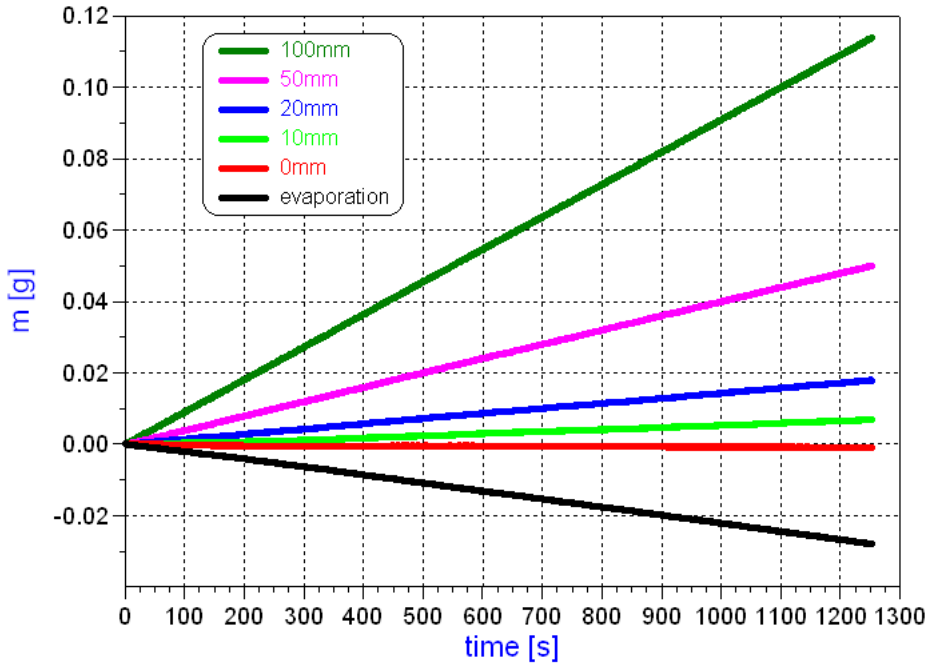

Figure 4.3: Measured mass for several water levels Δh. The evaporation rate of water in the outlet reservoir is measured (black line) and subtracted.

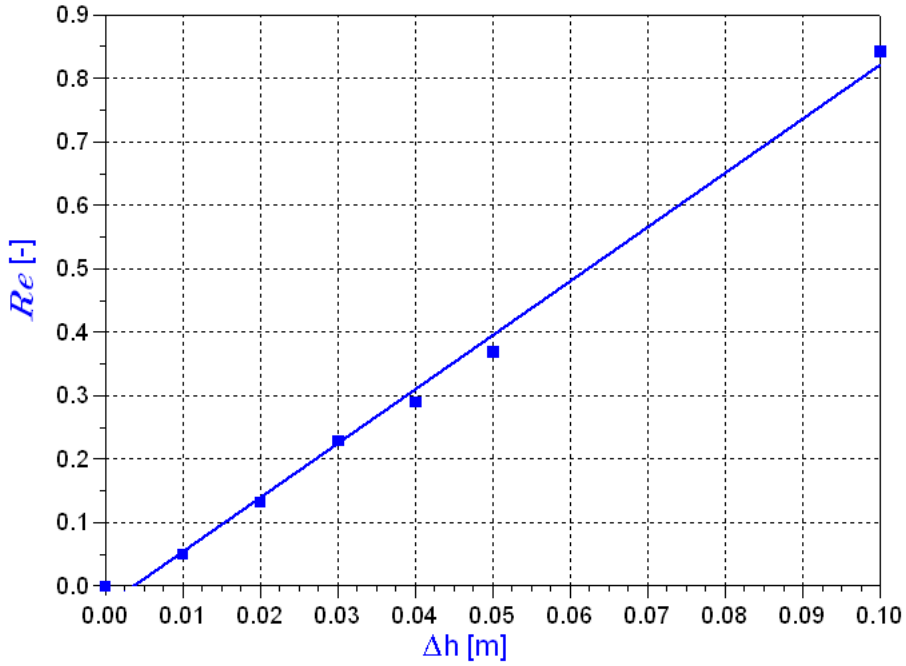

Figure 4.4: Reynolds numbers for different water levels using the gravity-driven system.

M	NA	d_{total} $[\mu m]$
5	0.15	35.72
10	0.30	8.92
20	0.40	4.61
40	0.60	1.96
63	0.70	1.37

Table 4.1: The applied microscope objectives, their numerical aperture and corresponding depth of field.

the passed light (λ_{ill}) coaxially through the objective into the micromixer for illumination. After absorption of the green light by either the microparticles or the fluorescent dye, red light is emitted (λ_{emi}). The red light passes through the beam splitter and the red filter and reaches the CCD camera. The red filter allows only emitted light to pass to the CCD camera and it blocks the scattered or reflected green light or surrounding light. Therefore, on the CCD camera a pure (red) fluorescent image is recorded, containing only information from the fluorescent microparticles or the fluorescent dye.

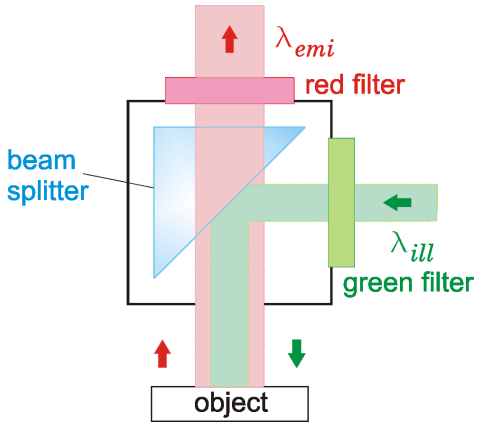

Figure 4.5: Epi-fluorescent cube inside the microscope, used for the velocity and concentration field measurements.

We use a high-performance cooled interline CCD camera (Image Intense, PCO, Germany) with 1376×1040 *pixels* and 12-bit readout resolution to record the images. The acquired images from the camera are transferred to a PC for the velocity or concentration measurements. The software DaVis 6.2 (LaVision, Götingen) is applied for further processing of the images. All timing, synchronization, and control of the camera, the electrical excitation and the lasers are achieved by a programmable timing unit (PTU) card, installed on the

PC, in conjunction with the DaVis software.

4.2 Electrical field

The glass chips, presented in section 3.2, both feature embedded electrodes on both sides of the meander channel. In principle, these electrodes are suitable to set up an electrical field within the chip, which is similar to the idealized electrical field, employed in the simulations of (Meisel and Ehrhard 2005) (cf. section 2.2). During the first experiments we realized, however, that the field even with an applied potential difference of 5 kV is very weak. The electroosmotic effects caused by this weak field, lead to small secondary velocities, which appear to be at the limit of measurability. For that reason, a more detailed analysis of the electrical field within the glass chip is conducted.

The situation within the glass chip is sketched in Fig. 4.6. In a cross section orthogonal to the channel axis (Fig. 4.6a), we recognize the two wire electrodes, positioned in square channels to both sides of the liquid-filled microchannel. The electrical field due to an applied potential difference between both electrodes is qualitatively sketched in Fig. 4.6a. As we are interested in the electrical field strength within the microchannel, it is sufficient to concentrate onto a slab of height d_W, as sketched in Fig. 4.6b. This slab certainly provides a good estimate for the local field strength within the liquid (water). The slab, however, will not reflect the overall capacity or resistance between both electrodes, as large parts of the glass chip are ignored. In detail, the overall capacity of the arrangement will be larger than for the slab and the overall resistance will be smaller than for the slab.

Both the liquid part and the glass part of the slab, electrically can be viewed as a capacitor, arranged parallel to a resistor. The equivalent electrical circuit, therefore, has the form given in Fig. 4.6c. For the glass part, the specific conductivity is $\rho_G = 8.1 \times 10^{10}\ \Omega m$, the specific dielectric constant is $\epsilon_G = 6.5$, and the distance is $d_G = 645\ \mu m$. Moreover, the dielectric constant for vacuum is $\epsilon_0 = 8.85 \times 10^{-12}\ As/Vm$, the length of the electrode is $l_E = 11\ mm$, and the thickness of the slab is $d_W = 110\ \mu m$. Hence, the capacitance and resistance of the glass part can be computed. We find

$$R_G = \frac{\rho_G d_G}{l_E d_W} = 4.3 \times 10^{13}\ \Omega, \tag{4.3}$$

$$C_G = \frac{\epsilon_G \epsilon_0 l_E d_W}{d_G} = 0.11\ pF. \tag{4.4}$$

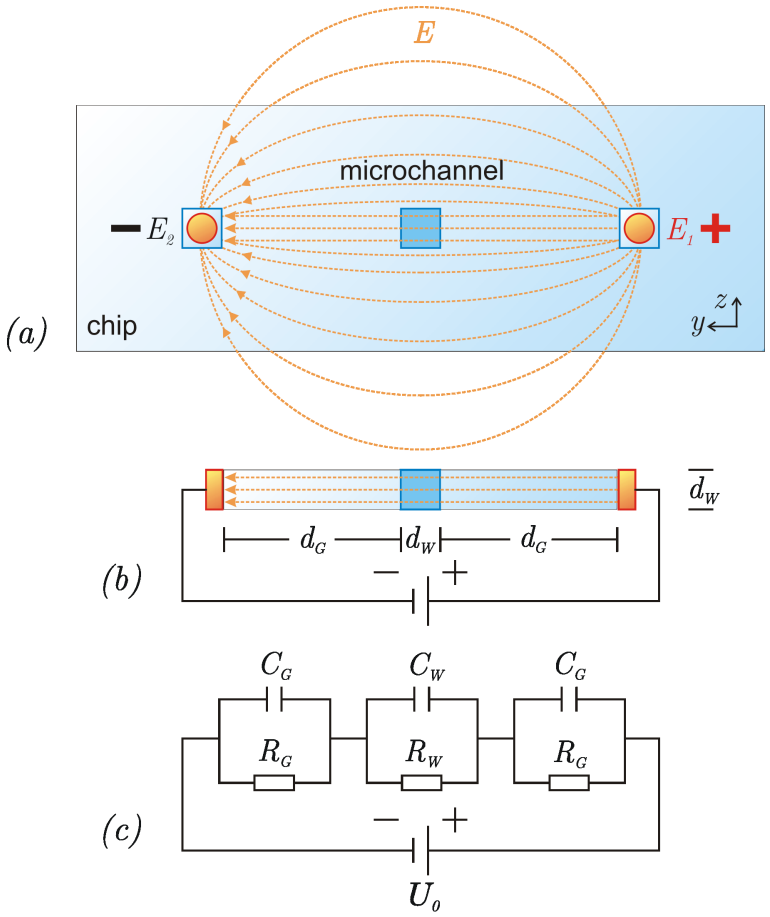

Figure 4.6: (a) Cross section of the glass chip with microchannel and wire electrodes, (b) simplified slab model for the situation between both electrodes, (c) equivalent electrical circuit for the slab model.

Similarly, for the liquid part we use the properties of deionized water, namely $\rho_W = 1.8 \times 10^5\ \Omega m$, $\epsilon_G = 82$, and $d_W = 110\ \mu m$, to obtain

$$R_W = \frac{\rho_W d_W}{l_E d_W} = 1.6 \times 10^7\ \Omega, \tag{4.5}$$

$$C_W = \frac{\epsilon_W \epsilon_0 l_E d_W}{d_W} = 8.0\ pF. \tag{4.6}$$

The overall ohmic resistance of the electrical circuit in Fig. 4.6c, thus, is $R_{tot} = 8.6 \times 10^{13}\ \Omega$, and the overall capacitance is $C_{tot} = 0.05\ pF$. Measurements at the actual glass chip give the values $R_{tot} > 3.0 \times 10^9\ \Omega$ (not measurable) and $C_{tot} = 0.35\ pF$. The large value of the

measured capacitance is not surprising, since the complete glass chip acts as capacitor and the slab capacitance should be smaller.

The time constant of a RC circuit allows to access, on which time scale the capacitor is discharged by the current through the resistor. For both parts we find the values

$$t_G = R_G C_G = 4.73\ s, \tag{4.7}$$

$$t_W = R_W C_W = 0.13\ ms. \tag{4.8}$$

Hence, for times $t \gg t_G,\ t_W$ after switching on a DC voltage U_0, the situation is purely governed by the ohmic resistances. Based on that situation, we find for the voltage U_W across the liquid part

$$U_W = 3.72 \times 10^{-7}\ U_0, \tag{4.9}$$

and an electrical field strength in the water of

$$E_W = \frac{U_W}{d_W} = 3.38 \times 10^{-3}\ m^{-1} U_0. \tag{4.10}$$

This estimate clarifies that, e.g. with an applied voltage of $U_0 = 5\ kV$, we reach only a field strength of $E_W = 16.9\ V/m$.

There is a second option to set up an electrical field, by immersing electrodes directly into the liquid (water). This set up is sketched in Fig. 4.7a. In both inlet reservoirs electrodes are immersed and connected to one potential. The electrode in the outlet reservoir is connected to a second potential. As electrodes we use gold wires of diameter 50 μm. All liquid-filled parts essentially act as resistors, namely the two parallel inlet tubes (R_1), the microchannel inside the chip (R_2), and the outlet tube (R_3). Therefore, we can to first approximation draw the equivalent electrical circuit as given in Fig. 4.7b.

With the cross-section area of the tubes $A_1 = A_3 = 1.96 \times 10^{-7}\ m^2$, length $l_1 = l_3 = 6.5\ cm$, channel length $l_2 = 6.3\ cm$ and cross-section area $A_2 = 1.21 \times 10^{-8}\ m^2$, we obtain for the resistances

$$R_1 = R_3 = \frac{\rho_W l_1}{A_1} = 5.97 \times 10^{10}\ \Omega, \tag{4.11}$$

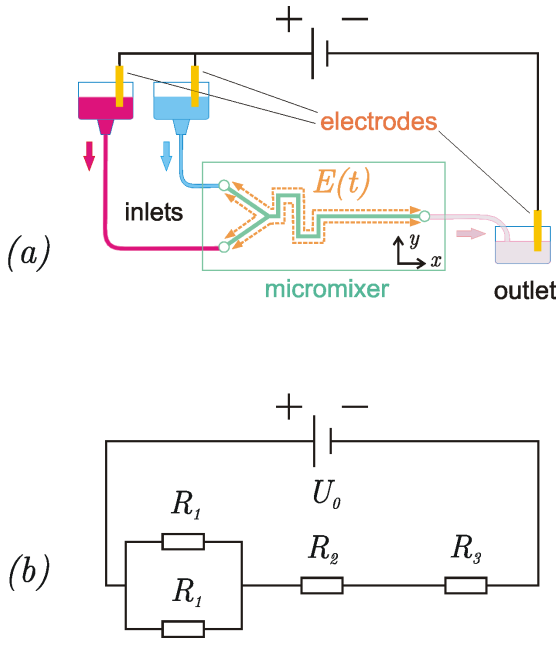

Figure 4.7: (a) Schematics of the electrical excitation by means of immersed electrodes, (b) equivalent electrical circuit for the immersed electrodes.

$$R_2 = \frac{\rho_W l_2}{A_2} = 9.2 \times 10^{11}\ \Omega. \tag{4.12}$$

Hence, a voltage of

$$U_2 = 0.91\, U_0 \tag{4.13}$$

drops along the microchannel of length l_2. The resulting electrical field strength in the water is

$$E_2 = \frac{U_2}{l_2} = 14.68\, m^{-1} U_0. \tag{4.14}$$

This estimate gives a field strength of $E_2 = 72.3\ V/mm$ for an applied voltage of $U_0 = 5\ kV$. This is a dramatic improvement by more than three orders of magnitude, if compared to the above setup (Fig. 4.6).

In summary, we have engaged for all experiments the electrical setup as sketched in Fig. 4.7a, as it provides a much stronger local field within the microchannel.

4.3 Micro particle image velocimetry

Particle image velocimetry (PIV) has been introduced briefly as method for velocity field measurements in the first chapter. In this subchapter the general concept of PIV is explained and the microscopic modifications of PIV are discussed. The results of first μPIV measurements, the accuracy of the measurement system, and some problems during the work with the test chip are presented. PIV in the passed two decades has become a powerful optical measuring technique for two-dimensional and three-dimensional flow studies, additionally offering a high spatial resolution. In a PIV system a pulsed light sheet illuminates a seeded flow and at each pulse a CCD camera captures an image of this flow. Two consecutive images at times t_1 and t_2=t_1+Δt are taken and afterwards subdivided into so-called interrogation areas (IAs), as shown in Fig. 4.8.

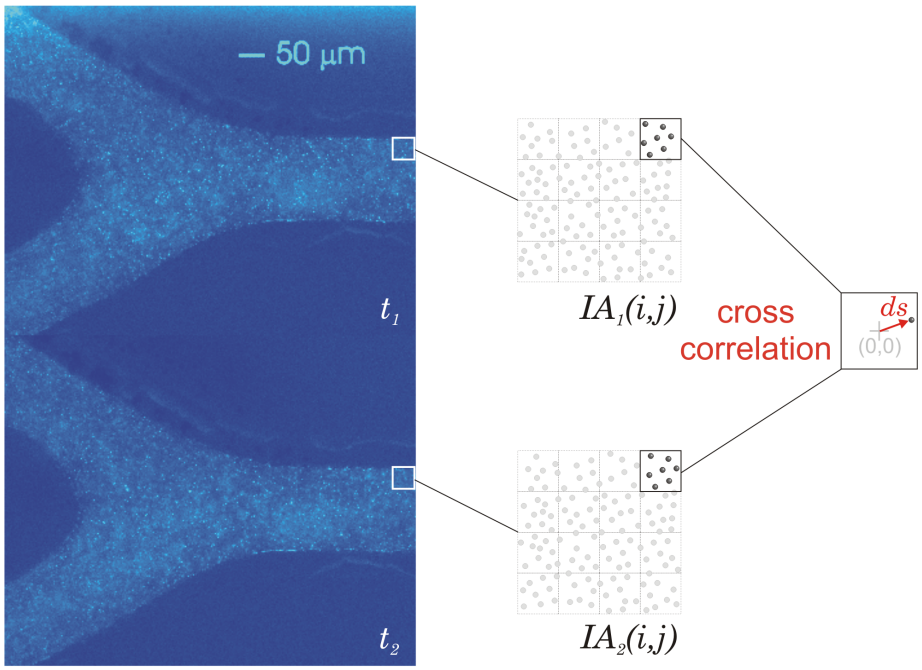

Figure 4.8: In PIV two consecutive images taken at times t_1 and $t_2 = t_1 + \Delta t$ are divided into small interrogation areas (IAs). From a cross-correlation of an IA at times t_1 and t_2 the average displacement vector is inferred.

The interrogation areas at times t_1 and t_2 are used to infer the movement of particles by means of statistical methods, i.e. by means of cross-correlation. As an example, in Fig. 4.8 the result of a cross-correlation process in PIV is depicted. In details, the correlation $CC(m,n)$ of two images of an interrogation area (IA) of size $p \times q$ *pixels*, taken at two

different times t_1 and t_2, is defined by

$$CC(m,n) = \sum_{i=1}^{p} \sum_{j=1}^{q} IA(i,j) \cdot IA(i+m, j+n). \tag{4.15}$$

The correlation $CC(m,n)$ exhibits a maximum, where the patterns in $IA(i,j)$ and $IA(i+m, j+n)$ are most similar. Since the pattern in IA is given by the particles, the offset of the maximum (m^*, n^*) allows to determine the averaged displacement vector $ds = (m^*, n^*)$ of the collective of particles within the respective IA. With known magnification M, and elapsed time between the images $\Delta t = t_2 - t_1$, the mean velocity vector $\overline{u}_{IA}$ of the respective interrogation area can be computed via

$$\overline{u}_{IA(i,j)} = \frac{ds}{M\Delta t}. \tag{4.16}$$

By means of subpixel interpolation, more accurate velocities can be inferred. The complete velocity field of the image is obtained by repeating the cross-correlation for each interrogation area.

In normal PIV, the pulsed light is usually provided by a laser beam, which is expanded by cylindrical lenses to form a light sheet with a thickness of around one millimeter. This thickness of the light sheet must be smaller than the depth of field of the imaging system. The camera is positioned perpendicularly to the light sheet. All seeding particles within the light sheet produce focused images, and therefore background noise from unfocused particles, is minimized (Adrian 1991). In general, too high particle concentration increases background noise due to unfocused particles between the camera and the light sheet. This reduces the visibility of the focused particles. Too low particle concentration causes a poor statistical basis, and therefore, unreliable results. Generally, 10-30 particles within an interrogation area are considered optimal for an accurate PIV image evaluation. The size of the particles must be small enough, that they follow the flow and do not disturb the flow significantly. On the other hand, the particles have to be large enough to scatter sufficient light for image recording. In summary, the choice of the size of the evaluation area, the time interval Δt, and the particle size and concentration are crucial, if highly-accurate PIV measurements are considered.

In microfluidic channels the above PIV setup is extremely difficult, since a light sheet of a few micron thicknesses can hardly be spanned up. Instead, volume illumination has to be applied for microchannels. Depending on the depth of field of the imaging system, two possibilities arise: (a) All particles within the channel are focused, if the depth of field is larger than the depth of the microchannel under investigation. (b) Only particles within the depth of field are focused, and the rest of particles remains unfocused and

produces background noise. This is the case, where the depth of field is smaller than the microchannel depth. Obviously, the second situation allows inference of velocity data from different depths of the microchannel, whereas the first situation provides only depth-averaged velocity data. In microscopic PIV measurements, moreover, the size of particles is drastically reduced. For microchannels application (Meinhart et al. 1999) in a 300 μm wide channel find particles of 200 nm diameter to be adequate for accurate measurements. Since the diameter of the particles is below the wavelength of the illuminating light (e.g. $\lambda_{ill} = 532\ nm$), the elastic scattering of light at particles is not effective. To solve this problem, fluorescent submicron particles, imaged by means of an epi-fluorescence technique, can be used (Meinhart et al. 1999). In summary, a combination of volume illumination and an epi-fluorescence technique is the foundation of a μPIV system. The μPIV system applied in our flow studies is schematically illustrated in Fig. 4.9.

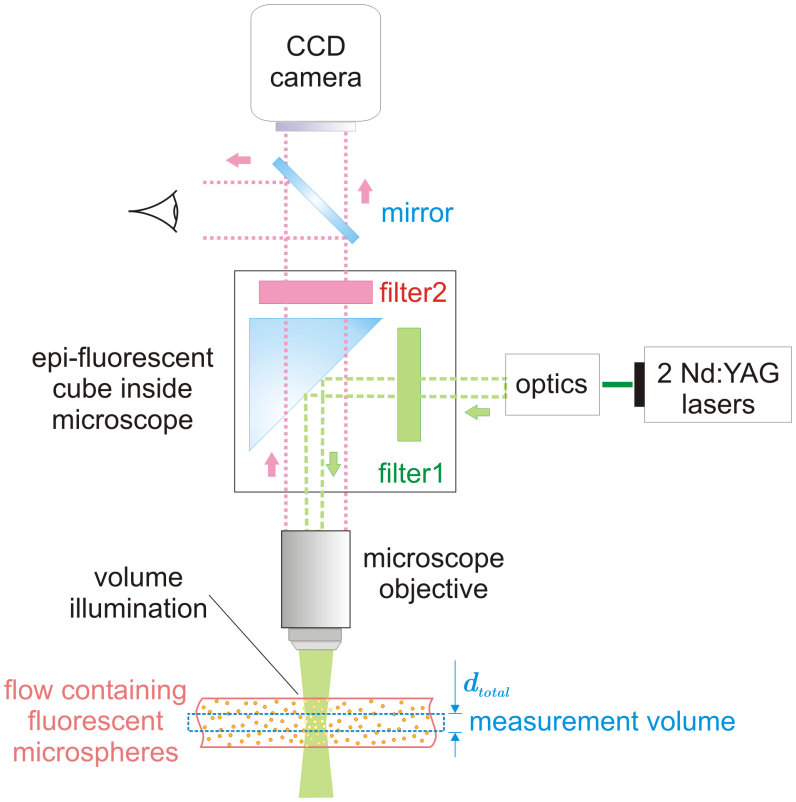

Figure 4.9: The applied μPIV for microflow investigations.

As light source we use two identical Nd:YAG lasers (model Solo-PIV, New Wave, Inc., USA), which deliver their light pulses along the same optical path. This is achieved by a system of (semitransparent) mirrors. The illuminating light ($\lambda_{ill} = 532\ nm$) is expanded and guided into the microscope by means of a collimator. The light passes through the green filter

of the epi-fluorescent cube within the microscope and coaxially progresses through one of the microscope objectives into the microchannel. The entire volume of the microchannel within the field of view is illuminated and the microparticles in this volume absorb the green light and emit red light ($\lambda_{emi} = 612\ nm$), due to their fluorescence properties. The particles within the focal plane are, firstly, imaged in a sharp fashion. Secondly, they receive the most intense (focused) illumination, and therefore emit at high intensity. The red emitted light passes through the microscope objective and the red filter of the epi-fluorescent cube into the CCD camera. We use fluorescent polymer microspheres (Duke Scientific Cooperation, USA) with diameters $d_p = 200$, 500, and 1000 nm. These particles are made of polystyrene, which has a density of 1.05 g/cm^3. Optimal excitation for these particles is by green light ($\lambda_{ill} = 542\ nm$), for emitting red at $\lambda_{emi} = 612\ nm$. We keep the ratio of particle volume to interrogation volume in the range $0.05 - 0.07$ %. Such a moderate particle concentration ensures a high signal to noise ratio, with relatively low background noise. Such a particle concentration leads e.g. to $3-5$ particles in an interrogation volume of $4.8 \times 4.8 \times 14.7\ \mu m^3$, when 500 nm particles and the $20\times$ objective are used.

μPIV measurements in flows with velocities below 10 $\mu m/s$ become inaccurate due to Brownian motion (Santiago, Wereley, Meinhart, Beebe and Adrian 1998). Since the seeding particles become small, the potential of random collisions between fluid molecules and seeding particles increases. Hence, collisions lead to statistical velocity fluctuation of the seeding particles around the mean velocity. Einstein's diffusion coefficient (Einstein 1905) for diluted suspensions, D, shows the inverse proportionality of particle size and diffusion

$$D = \frac{\kappa T}{3\pi\mu d_p}, \tag{4.17}$$

where κ is the Boltzman constant, T the absolute temperature, and μ the dynamic viscosity of the fluid. Following (Santiago et al. 1998) the relative error due to Brownian motion ε_B can be estimated by

$$\varepsilon_B = \frac{1}{u}\sqrt{\frac{2D}{\Delta t}}. \tag{4.18}$$

This equation shows that fast flows (large u) are less affected by Brownian motion. Moreover, the error can be reduced with large time periods Δt between the images (for cross correlation). This is not too helpful, since large u typically requires small Δt in PIV measurements, to keep the particle displacement at a reasonable fraction of the interrogation area. The error due to Brownian motion arises from molecular collisions within the fluid, and, therefore, averaging over groups of particles or averaging in time reduces this error (Santiago et al. 1998). The diffusion uncertainty is proportional to $\varepsilon/\sqrt{N}$, in which N is the total number of particles in the average. Ensemble averaging in steady flows also helps

to reduce the background noise. From N computed cross correlation functions $CC_k(m,n)$, the averaged correlation function is simply defined by

$$CC_{avg}(m,n) = \frac{1}{N}\sum_{k=1}^{N} CC_k(m,n). \tag{4.19}$$

Due to the depth of field within the microscope setup, μPIV delivers velocity information from a measurement volume. The thickness of the measurement volume is termed depth of correlation, δz_C (Fig. 4.9). δz_C is independent from the magnification M and can be inferred from

$$\delta z_C = \frac{3n\lambda_{emi}}{NA^2} + \frac{2.16 d_p}{\tan\theta} + d_p. \tag{4.20}$$

In Eq. (4.20) n is refractive index, λ_{emi} the wavelength of the emitted light, NA the numerical aperture, d_p the particle diameter, and θ the collection angle of the optical system (Meinhart, Wereley and Gray 2000a). θ can be derived from $\tan\theta \simeq \sin\theta = NA/n$. A strong dependency of δz_C on NA is obvious from Eq. (4.20). Further, large particle diameters d_p increase δz_C. For example, for 200 nm particles and the 5× objective ($NA = 0.15$) we get $\delta z_C = 84.68$ μm, and for 1000 nm particles and the 63× objective ($NA = 0.70$) depth of correlation falls to $\delta z_C = 7.83$ μm. In table 4.2 a list of numerical apertures of the applied microscope objectives and δz_C for particles with diameters in the range $200 - 1000$ nm is given. It is important to note that the depth of correlation, rather than the depth of field in table 4.1, presents a reasonable estimate for the thickness of the measuring volume.

NA	δz_C $[\mu m]$
0.15	84.68 - 97.00
0.30	22.04 - 28.60
0.40	12.75 - 17.87
0.60	6.02 - 9.70
0.70	4.56 - 7.83

Table 4.2: The numerical apertures of objectives and the corresponding depths of correlation for microparticles in the range $d_p = 200 - 1000$ nm.

By means of averaging and without any filtering, we try to characterize how accurate our μPIV system works. Here, the effect of averaging on the reduction of errors, associated with Brownian motion and unfocused particles, is tested. For this purpose the steady flow of water, seeded with fluorescent particles ($d_p = 1$ μm), through the straight channel is investigated. This flow is chosen, because an analytical (series) solution exists for comparison.

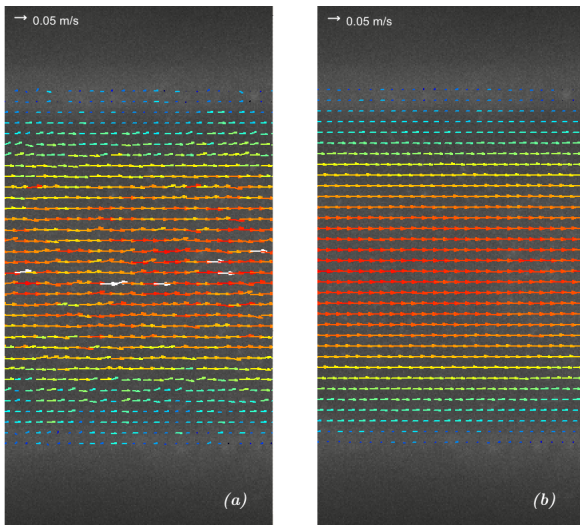

Figure 4.10: Comparison of the velocity field of the flow within a straight channel at $Re = 3.17$ *inferred (a) from a single (instantaneous) measurement, and (b) from an ensemble average over 120 measurements.*

A volumetric flow rate of $\dot{V} = 1\ ml/h$ is selected which corresponds to $U_{mean} = 27.7\ mm/s$ and $Re = 3.17$. The $20\times$ microscope objective is used and we adjust the measurement plane at the mid-height level of the channel, with a depth of correlation of $\delta z_C = 17.87\ \mu m$. In this experiment 120 double images with a time interval of $\Delta t = 75\ \mu s$ are taken, whereas 2 s elapses between each measurement. For the μPIV evaluation an interrogation area of 16×16 *pixels* and with 50 % overlap is selected. Fig. 4.10a shows an instantaneous velocity field, inferred from a single measurement, which appears noisy and does not present the vector field of a steady flow. The velocity field of the ensemble-averaged measurement is presented in Fig. 4.10b. These results indicate that ensemble averaging technique is a promising method to reduce noise. To quantify the deviation from the steady flow field, the velocity profiles obtained from these measurements are compared to the theoretical solution. For this purpose the y-coordinate is nondimensionalized by the channel width d and the velocity is nondimensionalized by the theoretical mean velocity U_{mean}. All profiles are plotted in Fig. 4.11.

The theoretical solution in the middle of a square channel is given by the series (Müller and Bühler 2001)

$$\frac{u_{th}(y)}{U_{mean}} = 2\sum_{k=1}^{N} \frac{\sin\lambda_i}{\lambda_i^3}\{1 - \frac{\cosh(\lambda_i \frac{y}{d})}{\cosh(\lambda_i)}\}, \tag{4.21}$$

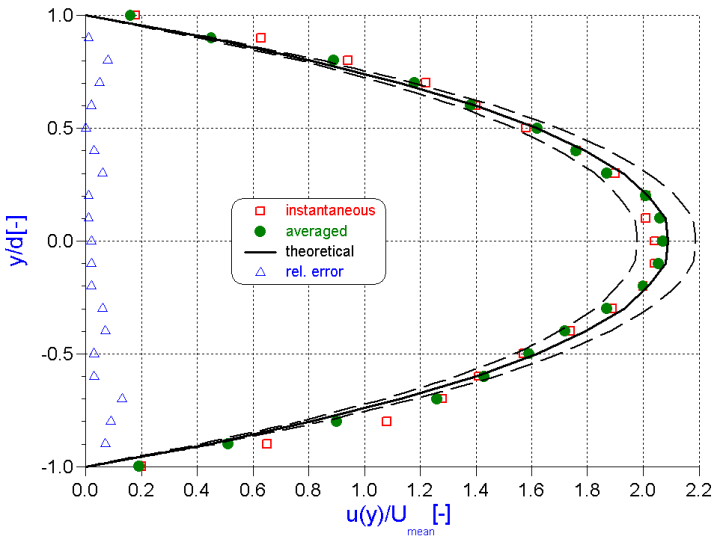

Figure 4.11: Comparison of the velocity profiles of the flow within a straight channel with $d = 100\ \mu m$, $Re = 3.17$. Instantaneous μPIV measurements, ensemble average of 120 measurements and theoretical solution are plotted, the dashed lines show ± 5 % deviation from the theoretical solution. The relative error is likewise given as function of y/d.

with

$$\lambda_i = \frac{(2i+1)\pi}{2}. \tag{4.22}$$

A single velocity profile is randomly taken from 120 flow field measurements and plotted in Fig. 4.11 by the symbols □ . The ensemble-averaged velocity profile from 120 measurements is given by the symbols ●. The solid line represents the theoretical profile obtained from Eq. (4.21). By comparing the theoretical curve and the averaged profile (symbols ●), a good agreement is obvious, while the single profile (symbols □) exhibits considerably more scattering. We define the relative error by

$$\varepsilon_B = \frac{\mid u_{th} - \overline{u_{exp}} \mid}{u_{th}}, \tag{4.23}$$

and include this information, encoded as symbols △, in Fig. 4.11. Additionally, ± 5 % error margins around the theoretical solution are given as dashed lines. Obviously, in the middle region of the microchannel the error is well below ± 5 %, while particularly at the walls the error gets larger. The overestimation of velocities close to walls, however, is a problem which appears at all measuring techniques with a finite measuring volume, and therefore is not surprising. The reason for the error in the channel core is manifold. Unfocused particles outside the measuring volume, too much or too few particles in some interrogation

areas, or Brownian motion are just a few candidates. From Eq. (4.17) and (4.18) the error due to Brownian motion can be estimated to be less than ± 0.5 % for the case of the straight channel (Fig. 4.11). Generally, within all the measurements presented in chapter 5, the error due to Brownian motion is estimated based on Eq. (4.18) to be in the range $0.003 \leq \varepsilon_B \leq 0.05$ %.

As discussed in section 2.1, particles subjected to an electrical field may undergo electrophoretic motion, depending on their electrophoretic mobility. We aim to measure flow fields both without and with electrical field application by means of μPIV. It is, therefore, important to ask, what effect the electrical field has onto the seeding particles used. For that reason, in a preliminary experiment, we fill the glass micromixer with a mixture of deionized water and microspheres of diameters $d_p = 0.2, 0.5, 1\ \mu m$. Electrodes are installed within one inlet channel and the outlet channels and all inlet and outlets are sealed with glue. The system, after some time, assumes a motionless state, except for some Brownian motion of zero mean velocity. If now an oscillatory electrical field of amplitude 14.5 V/mm and a frequency of 0.5 Hz is applied, we observe small but measurable movements of the particles. Velocities of the 1 μm particles reach 7.7 $\mu m/s$, and velocities of the 0.2 μm particles reach 5.8 $\mu m/s$. Comparing these electrophoretic velocity amplitudes with typical velocities during the flow field measurements reveals, that the error in all cases is less then 0.7 %.

In summary, an accurate velocity measurement system for microflows, by means of microscopic particle image velocimetry (μPIV), has been achieved. Microparticles with different diameters (0.2, 0.5, 1 μm), microscope objectives with different magnification and numerical aperture and, hence, different thickness of the measuring volume have been tested. Further, an ensemble averaging technique has been employed to remove error, e.g. resulting from Brownian motion. All measurements have been successfully validated against a theoretical solution within a square-cross-section microchannel. The μPIV system offers reliable results with less than ± 5 % error and high spatial resolution of 2 μm. Additionally, velocity information as close as 2 μm from the wall can be obtained.

4.4 Micro laser-induced fluorescence

For mass transport investigations in micromixers or in microseparation devices, it is important to capture likewise the concentration fields within these channels. For this reason, we develop a concentration field measurement technique, based on fluorescence intensity.

A schematics of the concentration field measurement system is presented in Fig. 4.12. Although a continuous-wave Argon laser (Model 2550, Spectra-Physics, USA) operating at

about 0.8 W ($\lambda_{exi} = 514\ nm$) is used as light source, the optical arrangement and recording process is almost identical as in the μPIV case. For the concentration measurements we apply the 5$\times$ microscope objective, which offers the largest field of view. Since the fluorescence technique, outlined below, collects fluorescence light from all depths of the microchannel, the focal plane of the microscope is adjusted 7 μm above the channel.

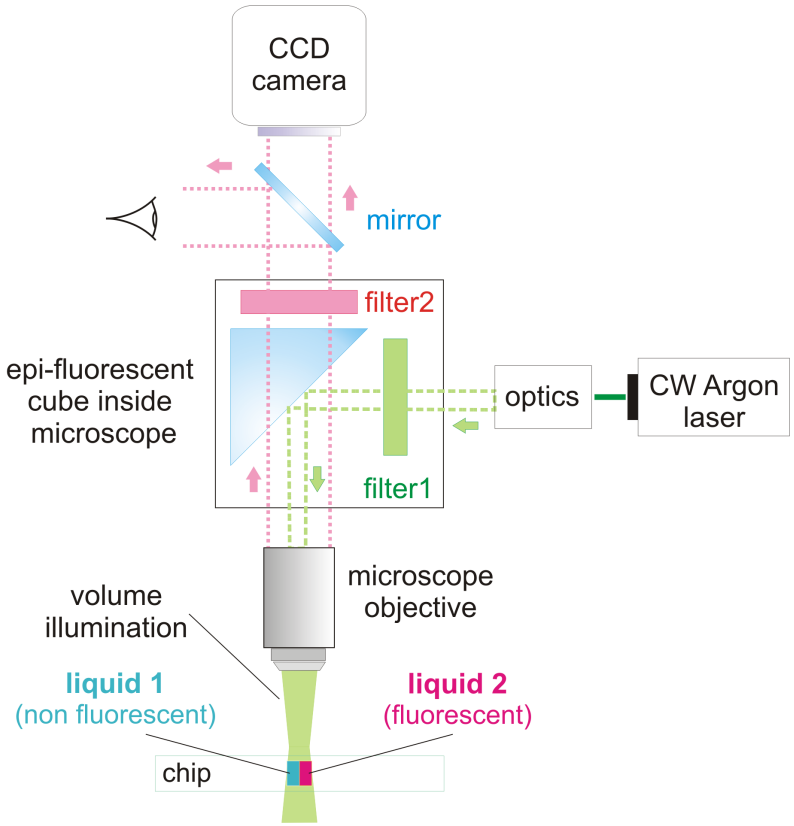

Figure 4.12: Schematics of the concentration field measurement system.

We use deionized and filtered water as non-fluorescent liquid and a solution of Rhodamine B in deionized water at a concentration of up to 0.35 g/l as fluorescent liquid. Rhodamine B is a water-soluble fluorescent dye, which can be excited by green light and emits red light ($\lambda_{emi} = 610\ nm$). The quantum yield of Rhodamine B at low concentrations is about $\phi = 0.97$. The quantum yield depends on the type of excitation (continuous wave, pulsed, etc.), the selected solvent, and weakly on concentration (Bindhu and Harilal 2001).

Fig. 4.13 shows an instantaneous fluorescence intensity field, taken from the junction of the Y-mixer on the PSU test chip. Both liquids, namely water and a solution of Rhodamine B in ethanol, are pumped at a volumetric flow rate of $\dot{V}_i = 1\ ml/h$. We recognize that fluorescence is able to detect concentration (of ethanol). However, we likewise recognize intensity fluctuations within regions of certainly homogeneous concentration. This is a

result of several imperfections, as e.g. non-homogeneous illumination, which needs to be corrected for a reliable measuring system.

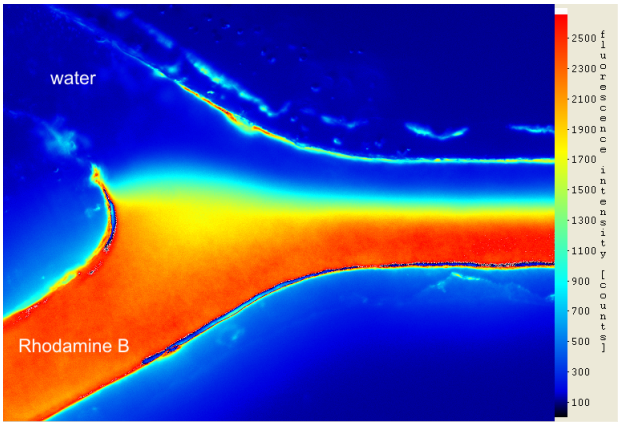

Figure 4.13: Instantaneous fluorescence intensity field, resulting from the mixing of water and a Rhodamine B solution in ethanol, both pumped at $\dot{V}_i = 1\ ml/h$.

The relation between the measured fluorescence intensity and the concentration field for this specific setup can be inferred theoretically, as shown by (Matsumoto et al. 2005). Following (Rost 1991) and (Walker 1987), the fluorescence intensity I_f, emitted due to an excitation intensity I_e, can be expressed as

$$I_f = I_e \phi \epsilon_e c, \tag{4.24}$$

where c is the concentration of the fluorescent dye, ϕ the quantum yield and ϵ_e the molar absorption coefficient of the excitation laser light. Eq. (4.24) is the leading term of a Taylor series and, thus, holds for dilute solutions (small c). The relationship between the concentration field of a fluorescent dye and the measured fluorescence intensity is strongly dependent on the optical arrangement. In typical concentration measurements on the macro scale, a planar laser light sheet illuminates a measuring plane, and a camera picks up the fluorescent light from a direction perpendicular to the light sheet (Houcine, Vivier, Plasari, David and Villermaux 1996). For concentration measurements in microchannels there is usually no room to span up a light sheet. Instead, one possibility is to deliver the laser light through the objective lens and to illuminate the entire field of view. In the context of fluorescence microscopy, the illumination parallel to the direction of observation is termed epi-illumination (Rost 1992). Fig. 4.14 shows the optical arrangement and gives a schematic representation of the measurement principle.

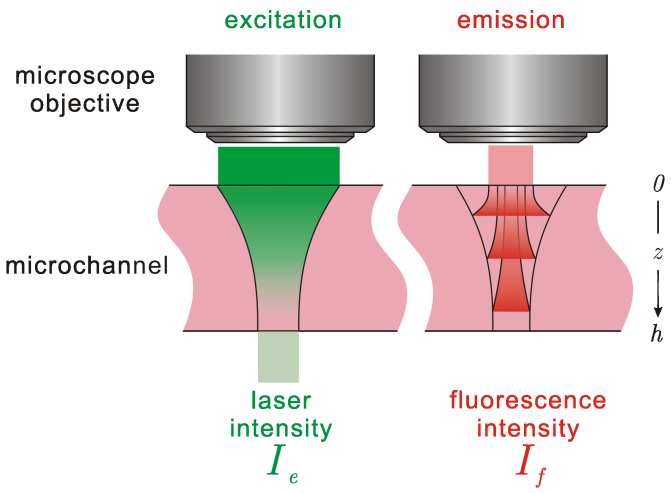

Figure 4.14: Schematic representation of the measurement principle. The intensities of the illuminating light (left part) and of the emitted light (right part) are both illustrated through the width of the beams.

The excitation laser light enters the microchannel through the objective lens and is attenuated as it travels along the z-axis. The attenuation of intensity is associated with the absorption by the fluorescent dye and can be described by the Beer-Lambert law

$$dI_e = -I_e c \epsilon_e dz. \tag{4.25}$$

If the concentration c is constant in z, the solution of the differential Eq. (4.25) is readily given by

$$I_e = I_0 \exp\left(-\epsilon_e c z\right), \tag{4.26}$$

where I_0 is the excitation light intensity at $z = 0$. As a consequence, fluorescent light I_f is emitted from each depth of the microchannel, according to the excitation light intensity I_e and the concentration c, as expressed in Eq. (4.24). The fluorescent light is also attenuated along its path back to the microscope, which can be described by

$$dI_f = I_f c \epsilon_f dz. \tag{4.27}$$

Here ϵ_f is the molar absorption coefficient of the fluorescent light. The fluorescence light intensity arriving at $z = 0$, using equations (4.24, 4.26, 4.27), can be expressed as

$$I_{f0} = I_0 \phi \epsilon_e c \exp\left(-[\epsilon_e + \epsilon_f] c z\right). \tag{4.28}$$

Since at $z = 0$ fluorescent light arrives from all locations z within the channel, the total intensity I_{total} can be determined from integration

$$I_{total} = \int_0^h I_{f0} dz = I_0 \phi \frac{\epsilon_e}{\epsilon_e + \epsilon_f} \left\{ 1 - \exp\left(-hc \left[\epsilon_e + \epsilon_f \right] \right) \right\}. \tag{4.29}$$

The above total intensity, however, cannot be detected by a CCD camera without further distortions: (i) the optical path and the CCD camera do not operate in an ideal manner and lead to a registration distortion $\alpha(x, y)$, (ii) the CCD camera will record a superimposed background image $\beta(x, y)$ due to the fluorescent emission from the structure material, and (iii) the illumination intensity will not be constant in the field of view, such that a distribution $I_0(x, y)$ is really present. Therefore, the registered intensity will be

$$I = I_0 \alpha \left\{ \beta + \phi \frac{\epsilon_e}{\epsilon_e + \epsilon_f} \left[1 - \exp\left(-hc \left[\epsilon_e + \epsilon_f \right] \right) \right] \right\}, \tag{4.30}$$

which has the form

$$I = I_0(x, y) \alpha(x, y) \left[\beta(x, y) + C_1 \phi \left\{ 1 - \exp\left[-C_2 c(x, y) \right] \right\} \right]. \tag{4.31}$$

From Eq. (4.29), obtained for constant concentration along the optical path, it is obvious that the total fluorescence intensity field is linked to the height-averaged concentration field. If concentration varies monotonously along the optical path (along z), a weighted average of concentration will be obtained, with the fluid close to the objective having a stronger effect. As long as the solution of the fluorescent dye is dilute, the effect of weighting will be marginal and both weighted average and normal average will be almost identical.

The relationship inferred in Eq. (4.30) is of limited value since a number of unknown quantities, namely the illumination intensity $I_0(x, y)$, the registration distortion $\alpha(x, y)$ and the background image $\beta(x, y)$ are present in this equation. Therefore, it appears reasonable to establish this relationship between the measured fluorescence intensity field and the concentration field experimentally through calibration measurements for the actual system. We run a set of calibration measurements for identical conditions immediately before the actual measurements. For that purpose, we use a number of solutions of defined concentration of Rhodamine B in distilled water, namely $c_i = 0.07, 0.14, 0.21, 0.28\ g/l$, as well as $c_{min} = 0$ and $c_{max} = 0.35\ g/l$. The solutions are pumped through both entry channels of the mixer until a homogeneous and steady concentration field is established within the meander section (and all other parts of the microfluidic chip). For each concentration c_i an image $I_i(x, y)$ is taken, while for the extreme values of concentration c_{min}, c_{max} typically fifteen

images are taken and averaged intensity fields $\bar{I}_{min}(x,y)$ and $\bar{I}_{max}(x,y)$ are computed. This helps to eliminate temporal laser intensity fluctuations and pixel noise. The normalized fluorescence intensity fields

$$G_i(x,y) = \frac{I_i(x,y) - \bar{I}_{min}(x,y)}{\bar{I}_{max}(x,y) - \bar{I}_{min}(x,y)} \tag{4.32}$$

are inferred from this. The experimental results for $G_i(x,y)$ are summarized in Fig. 4.15. It should be noted that Eq. (4.32) reflects a calibration of each pixel, using the (local) intensities at the extreme concentrations c_{min} and c_{max}. This represents a spatially–dependent calibration. The measurements employ six test areas of typically 100×200 μm (about 150×300 $pixels$) within the meander, and the averaged normalized fluorescence intensities in these test areas are plotted as open circles in Fig. 4.15. We recognize an increase of the normalized intensities with increasing concentration until saturation occurs around $c \simeq 0.2$ g/l, as can be seen in Fig. 4.15. The scatter of the data for the various test areas is less than ± 4 %.

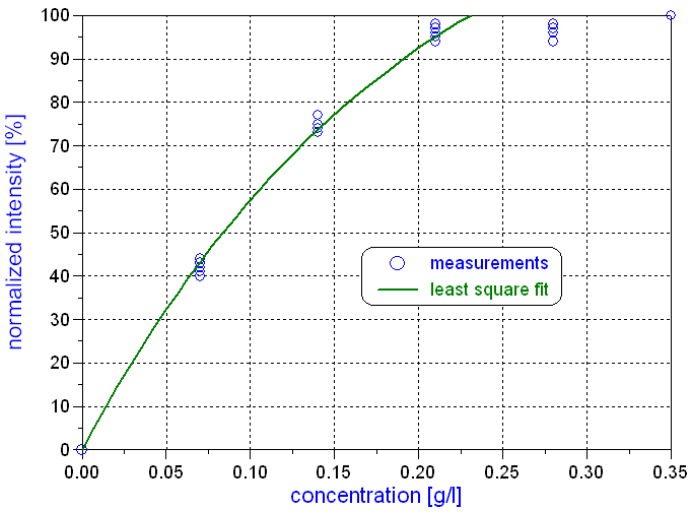

Figure 4.15: Normalized fluorescence intensity as function of concentration: open circles are measured values, evaluated and averaged across six test areas, the solid line gives the least-square fit.

From our images at defined concentrations, we can infer more detailed error estimates for this measuring technique. Obviously, the scatter of the data in Fig. 4.15 should depend on the size of the test area. In other words, large test areas through averaging should exhibit smaller errors. This error reduction - of course - is at the cost of reduced spatial resolution in actual field measurements. Therefore, we have likewise analyzed our images with test

areas of different size and the largest errors are summarized in table 4.3. As expected, the error increases for small test areas, but remains less than -4.3 % / $+ 5.9$ % in all cases.

test area $[pixels]$	error [%]
10×10	-4.3 / +5.9
100×100	-3.7 / +5.2
150×300	-3.8 / +3.3

Table 4.3: Concentration field measurement error.

Theoretically, we can likewise express the expected normalized fluorescence intensity field by introducing Eq. (4.31) into Eq. (4.32). Assuming an approximately constant quantum yield ϕ, we find for $c_{min} = 0$

$$G(x,y) = \frac{1 - \exp\left[-C_2 c(x,y)\right]}{1 - \exp\left[-C_2 c_{sat}\right]}. \tag{4.33}$$

This equation clarifies that a number of unknown quantities as $\alpha(x,y)$, $I_0(x,y)$, $\beta(x,y)$, C_1, ϕ have been eliminated and a direct functional relationship $G(x,y) = f[c(x,y)]$ with two unknown constants C_2, c_{sat} is established. Within Eq. (4.33), c_{sat} accounts for the saturation. We determine these constants by a least–square method, applied to the experimental data in the range $0 \leq c \leq 0.21\ g/l$, and obtain $C_2 \simeq 5\ l/g$ and $c_{sat} \simeq 0.23\ g/l$. The correlation (Eq. (4.33)) is likewise plotted in Fig. 4.15 as a solid line.

A series of measurements with different channel Reynolds numbers is selected to demonstrate the potential of the above measuring technique. For this purpose pump 1 is filled with pure water and pump 2 is filled with a solution of 0.21 g/l Rhodamine B in water. Both pumps deliver completely identical volumetric flow rates $\dot{V}$, whereas the range of flow rates allows to cover the Reynolds number range $0.11 \leq Re \leq 27$. The Reynolds number in the common channel upstream of the meander is defined by Eq. (4.1), with the average velocity in the channel $u_{mean} = 2\dot{V}/(d_1 d_2)$. As both pumps provide identical volumetric flow rates somewhat downstream of the the Y-junction in the straight common channel, at least in the channel center, both liquids flow parallel at identical velocities. Thus, within most of this straight channel, purely diffusion is responsible for the mass transport between both liquid streams. This is not true as soon as the liquids enter the meander, where secondary flows arise.

Fig. 4.16 shows two examples for the normalized fluorescence intensity field. For the large Reynolds number of $Re = 11$ (Fig. 4.16b) we recognize two layers of liquid, the lower layer at intensities around 100 % (corresponding to 0.21 g/l) and the upper layer at an intensity

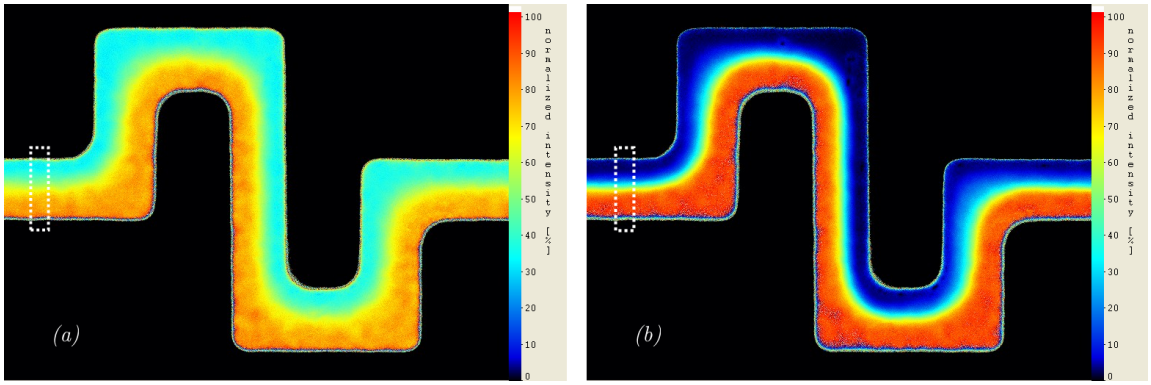

Figure 4.16: Normalized fluorescence intensity fields within the meander channel, obtained for the cases (a) $Re = 1.3$ and (b) $Re = 11$.

around 0 %. Between both layers a thin concentration boundary layer is obvious. For this large Reynolds number, diffusion in the upstream common channel does not have enough time to achieve significant mixing between both layers. In contrast, for $Re = 1.3$ (Fig. 4.16a) diffusion has more time to flatten the concentration gradients and, thus, the intensity field and the concentration field appear more balanced. For even smaller Reynolds numbers, namely for $Re = 0.11$ and $Re = 0.4$, we find homogeneous intensity fields, indicating perfect mixing and a homogeneous concentration field within the complete meander.

From the given normalized fluorescence intensity field, via

$$c(x,y) = -\frac{1}{C_2} \ln \{1 - G(x,y) + G(x,y) \exp [-C_2 c_{sat}]\}, \tag{4.34}$$

we can infer the height-averaged concentration field $c(x,y)$. As an example, we shall discuss concentration profiles across the straight channel, immediately before it enters the meander. In detail, the profiles are inferred by averaging 35 rows of pixels (corresponding to $\sim 20\ \mu m$) within the respective region (marked rectangular regions in Fig. 4.16). Averaging several wall-normal rows clearly reduces noise and, hence, error within the wall-normal profiles (table 4.3 and the respective error discussion). This averaging happens at the cost of lower spatial resolution in the wall-tangential direction. This loss of spatial resolution, however, is not critical as there is little variation in the wall-tangential direction. Overall, this procedure allows subsequently for a more accurate determination of the (wall-normal) concentration gradient in the channel center.

In Fig. 4.17 a set of concentration profiles from the middle region of the channel is extracted for the range $0.4 \leq Re \leq 27$ of Reynolds numbers. Even though we have averaged 35 rows of pixels in the (horizontal) y-direction, the spatial resolution in the (vertical) x-direction remains at $0.63\ \mu m/pixel$. The measured data are given as closed circles of various colors.

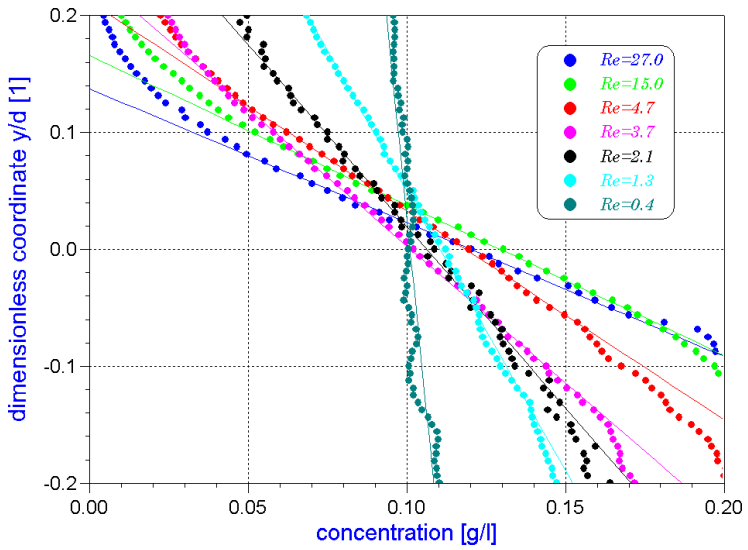

Figure 4.17: Concentration profiles for various Reynolds numbers.

We recognize for $Re = 0.4$ an almost homogeneous concentration of $c \simeq 0.1\ g/l$, indicating perfectly-mixed fluids. With increasing Reynolds numbers the concentration gradient in the channel center steepens. For the largest Reynolds number this corresponds to a situation of two layers at constant concentration $c = 0$ and $c = 0.21\ g/l$ with a thin intermediate concentration boundary layer (blue closed circles and line). From the experimental data points (closed circles) in all cases a linear behavior of concentration in the channel center is obvious, although not all profiles are perfectly symmetric around the channel center $x/d_1 = 0$. Therefore, we infer a linear regression curve from the experimental data with linear behavior. These least-square curves are plotted in Fig. 4.17 as solid lines of corresponding color. A comparison of both the linear regression curve and the experimental data points reveals that in all cases a perfect description is obtained in the center region of the channel. The measured concentration gradients are in the range $0.17 \leq \partial c/\partial x \leq 3.98\ mg/(l\ \mu m)$ for the investigated range of Reynolds numbers.

From the concentration gradients, inferred from the linear regression curves, it appears straight forwards to compute the thickness δ of the concentration boundary layer. We utilize the linear regression curves to infer δ, because by statistical means it provides a more accurate value for the concentration gradient and because the measured profiles (partly) exhibit saturation outside the channel center. The result is plotted in dimensionless form δ/d_1 in Fig. 4.18 as function of Reynolds number. The experimental data (closed circles), plotted in double-logarithmic fashion, with reasonable accuracy follow the dependency $\delta/d_1 \propto Re^{-1/2}$, which is likewise given in Fig. 4.18 as a solid line. From simple physical reasoning, the diffusion length, measured by the thickness of the concentration boundary

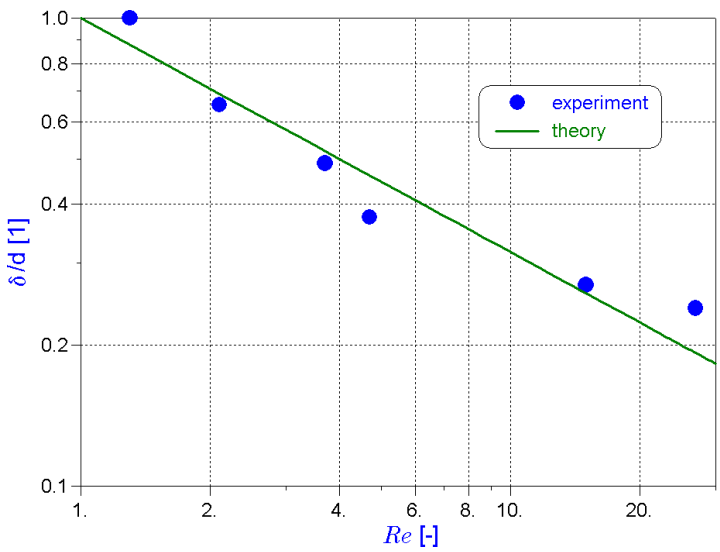

Figure 4.18: Thickness of diffusion boundary layer δ as function of Reynolds number.

layer δ, and diffusion time t_d are related via

$$t_d \sim \frac{\delta^2}{D}, \tag{4.35}$$

with diffusivity D. On the other hand, the time over which diffusion is active in the present mixer corresponds to the transport time t_t of the liquids between the Y-junction and the measuring cross section (distance $l = 17\ mm$). With the transport time

$$t_t = \frac{l}{\bar{u}} = \frac{d_h l}{\nu Re}, \tag{4.36}$$

in conjunction with Eq. (4.35), the dependency

$$\frac{\delta}{d_1} \sim \frac{\sqrt{d_h l}}{d_1} Sc^{-1/2} Re^{-1/2} \tag{4.37}$$

is readily inferred. Here $Sc = \nu/D$ is the Schmidt number. The agreement between the experimental data and the theoretical expectation verifies that the spatial concentration gradients have been determined at good accuracy. In detail, the deviation of the experimental boundary layer thickness from the theoretical curve is less than ± 18 %. This deviation is not caused by the measuring error alone. It likewise reflects the difference between the real (diffusion-dominated) transport from the Y-junction to the measuring section and the simple diffusion analysis engaged to derive Eq. (4.37). Moreover, the determination of spatial gradients appears more critical than the determination of the scalar field itself.

In summary, we have developed a measuring system for microchannels, which allows via a fluorescent dye marker to measure height-averaged concentration fields (of the marked liquid). Measurements offer a good spatial resolution of 0.63 $\mu m/pixel$ and a reasonably-good accuracy with errors less than typically ± 6 %. The measuring system has been verified for a diffusion-dominated problem of two parallel streams of two liquids, where diffusion can be characterized likewise analytically. The agreement between experimental measurements and a simple analytical model is good. Several averaging techniques have been proven to increase accuracy and/or to reduce noise: (i) ensemble averaging of several measured concentration fields greatly eliminates (for steady situations) noise in the fluorescence intensity, (ii) averaging several rows of pixels allows to obtain more accurate profiles, whereas spatial resolution along the profile remains high, and spatial resolution normal to the profiles is reduced.

Chapter 5

Results

The discussed measuring techniques, namely μPIV and μLIF, are engaged to study the flow and mass transfer in various parts of the micromixer, with and without electrical excitation. The results in this chapter are presented in four subchapters, covering (a) the flow and mass transport through the meander at large Reynolds number for pressure-driven flow, (b) the electroosmotic flow in a straight microchannel, (c) the flow within the meander due to electrical excitation, and (d) the mass transport within the meander due to electrical excitation.

5.1 Flow and mass transport for pressure-driven flows through the micromixer

The focus of the first investigations lies on the flow and mass transport within the meander part of the micromixer for a pressure-driven situation. Here, particularly the range of large Reynolds numbers is of interest, since at large Reynolds numbers we expect secondary three-dimensional flows, induced at the bends, which might be helpful for the mixing. For the investigations we use the glass micromixer with $X = 17000\ \mu m$, as outlined in section 3.2. Further, the two syringe pumps deliver identical volumetric flow rates into both inlets of the micromixer. Both liquids are deionized water, whereas one is marked with Rodamine B. The selected parameters for the optics and the PIV evaluation during this investigation are as follows: microscope objective 10×, 25 double frames are taken in each level and are ensemble averaged, the time interval between two images of a double frame is $\Delta t = 10\ \mu s$, the sampling frequency for these 25 double frames is 3.3 Hz, and the interrogation area is of size $16 \times 16\ pixels$.

Concentration fields within the meander are presented in Fig. 5.1, where (a) shows the result for $Re = 27$ and (b) shows the result for $Re = 42$. As for the case of smaller

Reynolds numbers (cf. section 4.4), we recognize a thin concentration boundary layer at the left entrance of the meander. In contrast to the findings at lower Reynolds numbers, downstream of the first bend a much wider, apparently mixed, region is obvious, which persists through the complete meander. At the exit of the meander the boundary-layer situation seems to reappear. For the interpretation of these concentration fields we have to recall that the method provides only height-averaged concentration fields.

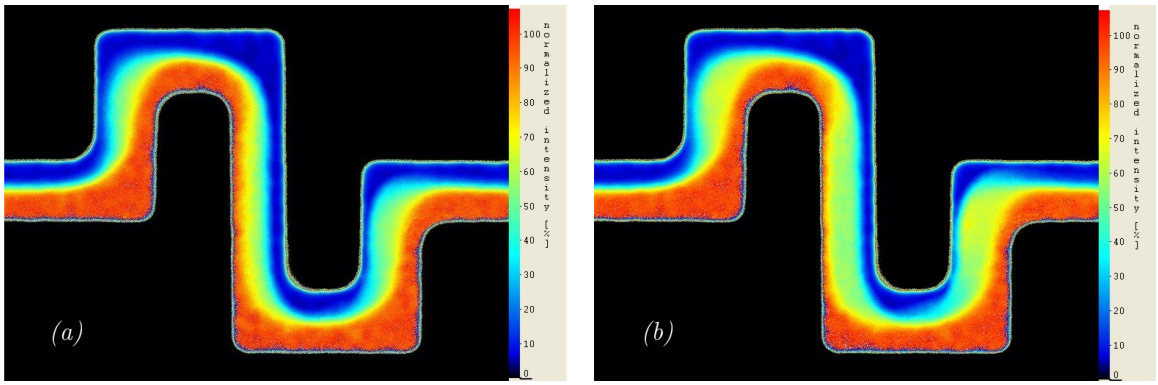

Figure 5.1: Concentration fields of flows at (a) Re=27 and (b) Re=42 within the meander part of the micromixer.

Hence, we assume that secondary three-dimensional flows, induced at the bends, are responsible for the observed (integrated) concentration fields. Such secondary flows may cause concentration variations along the optical path, which cause the apparently-mixed regions. To clarify these questions, the velocity field has to be measured. For this purpose we deliver through inlet 1 pure water and through inlet 2 water seeded with 500 nm particles (instead of Rhodamine B), both at identical volumetric flow rates. The partial seeding of liquid 2 (red in Fig. 5.1) allows us to follow liquid 2 through the meander, whereas we obtain no velocity information from liquid 1 (blue in Fig. 5.1). From the bottom to the top of the channel we measure the velocity fields at 17 levels with $d_z \simeq 6.5\ \mu m$. Hereby we observe that the portion of the channel occupied by liquid 2 changes from level to level, indicating a real three-dimensional flow situation. One example of the velocity field in the level 40 μm above the bottom wall of the meander is depicted in Fig. 5.2. This level is not at mid-height of the meander channel, but 15 μm below. We recognize that liquid 2 at the first bend has moved inwards, while liquid 1 occupies the outer region of the bend. This can be inferred from the dark region, since liquid 1 is not seeded. Downstream, liquid 2 several times changes the side of the channel, before it leaves the meander in the expected fashion, namely in the portion occupied by the red liquid in Fig. 5.1. Liquid 1 occupies everywhere the complementary portion of the channel, typically visible as dark areas.

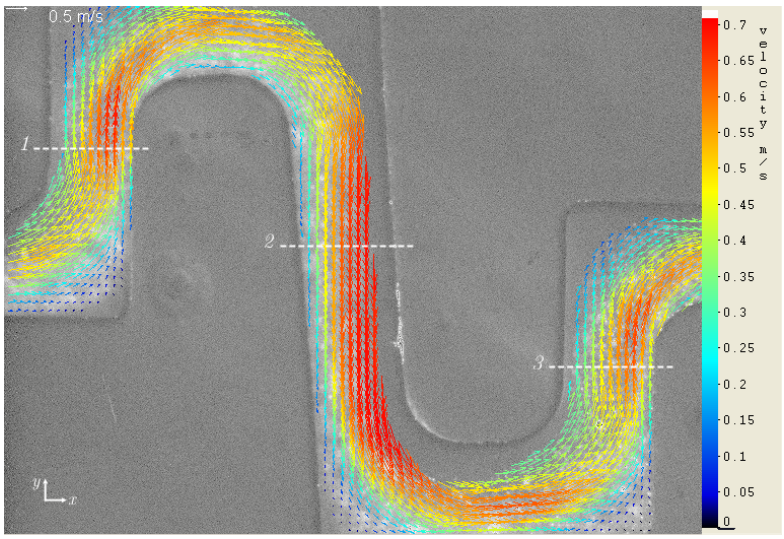

Figure 5.2: Averaged velocity field of the flow (Re=42) at a level 40 μm *above the bottom wall. All velocity information is from liquid 2 (red in Fig. 5.1), whereas dark regions appear where liquid 1 (blue in Fig. 5.1) is present.*

While Fig. 5.2 provides some insight into the flow in different levels above the bottom wall, it is possible to infer the fully three-dimensional velocity profiles in the sections *1-3* (dashed lines in Fig. 5.2) from the measurements performed at 17 levels. The results are presented in Fig. 5.3. The profile in section *1*, immediately after the first bend to the left, clarifies that liquid 1 penetrates in the channel mid-height into liquid 2 outwards, while liquid 2 moves inwards at both the bottom and the top walls. This appears clearly related to so-called Dean vortices. Dean vortices are due to the interplay of centrifugal forces and the no-slip condition at walls. Consequently, a pair of Dean vortices arises in bends, directed outwards in the channel center and recirculate along the walls. The profile in section *2*, after two bends to the right, shows the opposite effect. Now liquid 2 penetrates back outwards into liquid 1. A similar situation as in section *1* can be observed in section *3*, which again is the consequence of two bends to the left. The above observations are mostly taken from the areas occupied by liquid 1 or 2. Additionally, the velocity profiles of liquid 2 indicate complex behavior, as e.g. all velocity maxima are shifted outwards due to centrifugal forces. Moreover, profiles with two separate maxima are present in sections *1* and *3*.

While Fig. 5.3 shows the velocity profiles within liquid 2, we can infer from the seeding particle distribution which portions of the cross section are occupied by liquid 2. This clarifies even more, how both liquids flow through the meander. The results of these evaluations are given in Fig. 5.4. We recognize at the entrance of the meander both liquids layered, whereas pure water (liquid 1) is marked blue and the seeded water (liquid 2) is marked

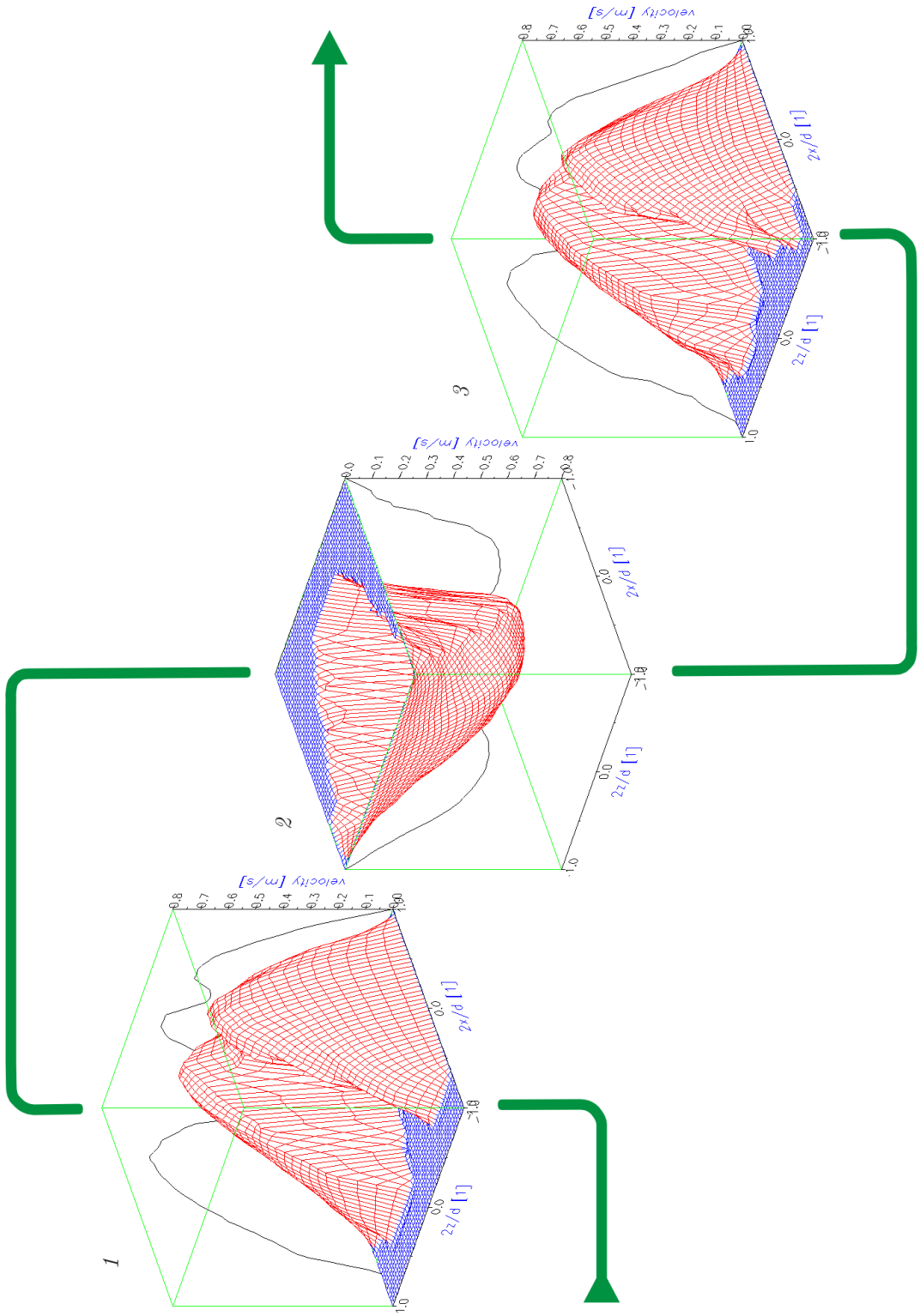

Figure 5.3: Axial velocity profiles of liquid 2 (Re=42) at the middle of the vertical channels. 1 and 3 give the profiles within the short channels and 2 shows the profile within the long channel.

red (Fig. 5.4a). In section *1* we clearly recognize, how Dean vortices move liquid 1 (blue) outwards in the center and liquid 2 (red) inwards at the channel walls (Fig. 5.4b1). In section *2* the Dean vortices move liquid 2 (red) outwards and recirculate liquid 1 (blue) along the walls. In section *3*, finally, the situation is similar to section *1*. In summary, all sections recover the findings already inferred from the velocity profiles in Fig. 5.3 in an even clearer fashion. It should be kept in mind, however, that a sharp threshold value for the particle concentration defines the boundary between both liquids. As this threshold value is picked arbitrary, the information in Fig. 5.4 cannot be quantitative with regard to the boundary position and, moreover, the real boundary between both liquids is not sharp but affected by diffusion.

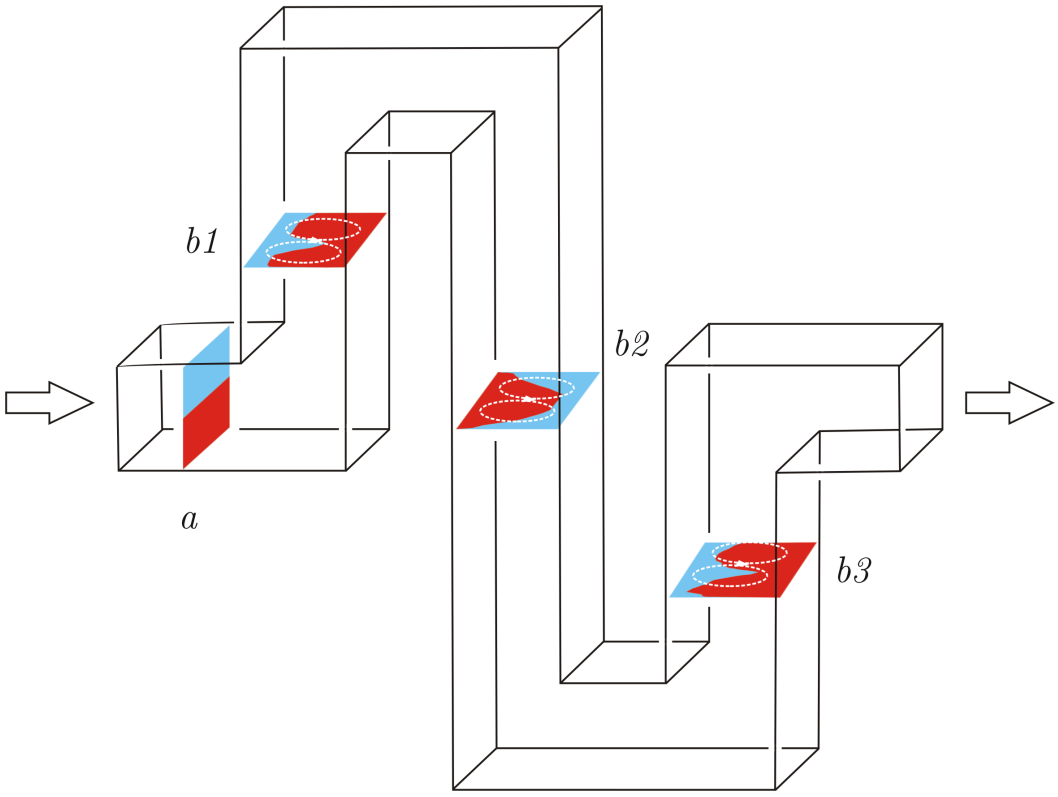

Figure 5.4: Cross sectional view of the particle distribution, marking liquid 2 (red). The cross sections are taken before the entrance of the meander (a) and at sections 1-3 within the meander (b).

To summarize, the investigations within the meander part of the micromixer for pressure-driven flows demonstrate that the combination of μLIF measurements and μPIV measurements are a powerful tool, which allows to access even concentration and flow information for really three-dimensional situations. The μPIV, used with one seeded liquid and with

scanning of the complete cross section in 17 levels, provides the additional information, needed to interpret the concentration field appropriately. From the combined information, the virtual interface between both liquids, the existence of Dean vortices, and the consequences for the height-averaged concentration fields can be understood.

5.2 Electroosmotic flow in straight microchannel

Within this section we discuss the effect of an electrical field onto the flow in a straight microchannel. For that purpose we engage a straight microchannel, made of glass with a cross section of $110 \times 110\ \mu m$, and apply a voltage in the range $0.5 - 1.5\ kV$ between channel inlet and channel outlet. To pronounce the electroosmotic effects, we pick generally low Reynolds numbers for the pressure-driven flow, and superimpose the electroosmotic flow onto that weak pressure-driven flow. As liquid we use deionized water, which has a low electrical conductivity. The low electrical conductivity has two advantages: (i) we minimize electrical currents through the liquid, and hence minimize Joule heating, (ii) we obtain a thick electrical double layer, and hence strong electroosmotic effects.

The parameters for the optics and PIV evaluation for this investigation are as follows: microscope objective 20×, 40 double frames are taken at each level and are ensemble averaged, at 15 levels of the channel the flow is measured at $\delta_z = 15.98\ \mu m$, the time interval between two images of a double frame is $\Delta t = 2\ ms$, the sampling frequency for the double frames is 4 Hz, and the interrogation area is of size 16×16 $pixels$. A mixture of microspheres of diameter 0.5 μm and 1 μm is used for seeding the liquids, the ratio of particle volume and interrogation volume is around 0.06 %.

At a Reynolds number $Re = 0.1$, we firstly measure the pressure-driven flow. The result at the level $2z/d = 0.5$ in the channel is given in Fig. 5.5a. The coordinate system has its origin at the channel axis $y = 0$, $z = 0$, therefore, marks the center of the channel. $2z/d = 0.5$ is just between the mid-height level and the top wall. We recognize a steady flow profile, with a maximum velocity of about 1 mm/s in the middle of the channel ($y = 0$), and vanishing velocities at the walls. This profile appears roughly parabolic. For the second measurement we have the channel inlet at a negative potential and the channel outlet at a positive potential, whereas the potential difference is 1.0 kV, yielding an electrical field of strength $E = -14.68\ V/mm$ within the channel. The electrical potentials at the inlet and the outlet are realized by gold electrodes, immersed into the corresponding reservoirs. The result for this negatively-directed electrical field vector is presented in Fig. 5.5b. We recognize near both walls of the microchannel electroosmotic flow to the left, i.e. against the pressure-driven flow. In the middle of the channel ($y = 0$), due to the pressure field, the flow

is still to the right, again featuring a roughly parabolic profile around the middle region. The case of a positively-directed electrical field with $E = +14.68\ V/mm$ is finally investigated, and the result is presented in Fig. 5.5c. Here, near both walls an electroosmotic movement of the liquid to the right is obvious, leading likewise to larger velocities in the middle of the channel. The parabolic form of the velocity profile across the channel appears to be preserved.

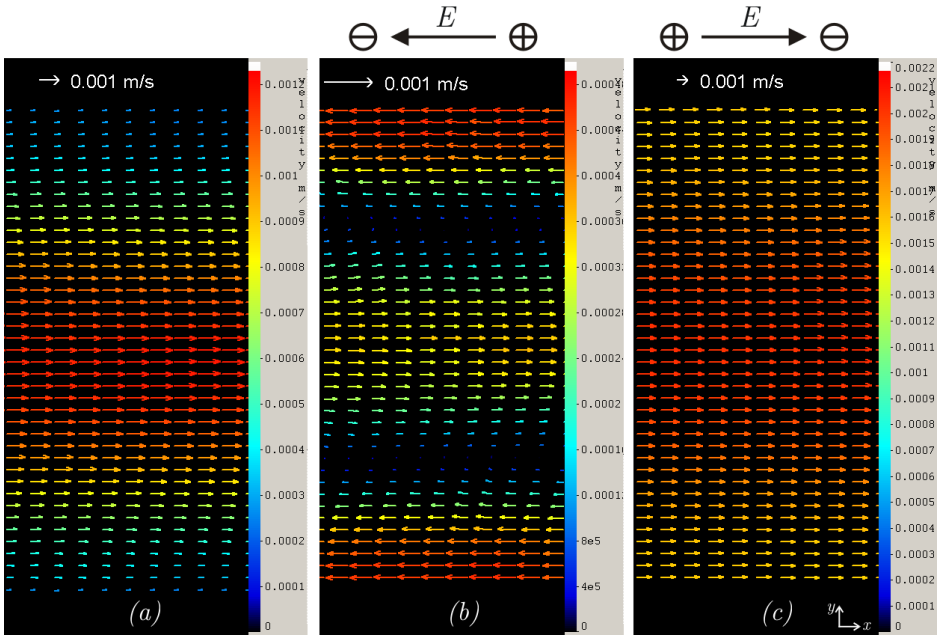

Figure 5.5: Velocity fields of the flow at Re=0.1 at the level 2z/d=0.5 of a straight channel: (a) without electrical field, (b) subject to an electrical field $E = -14.68\ V/mm$, and (c) $E = +14.68\ V/mm$. Note the different vector scales, indicated by the reference vector.

Fig. 5.6 compares the axial velocity profiles, already presented in Fig. 5.5, within one diagram quantitatively. The black curve, without electrical field, shows the pressure-driven flow at $Re = 0.1$. The profile appears roughly parabolic, the velocity in the middle is $u \simeq 1.2\ mm/s$. The green curve, obtained for a positively-directed electrical field, clearly gives larger velocities of up to about 2 mm/s in the middle. The origin of the faster flow lies in the electrical double layer, where the axial velocity rises rapidly to a value of 1.4 mm/s. The opposite effect, namely negative velocities close to the walls, is caused by a negatively-directed electrical field (red curve). Negative velocities of up to $-0.6\ mm/s$ at the walls are responsible for velocities of only 0.3 mm/s in the middle of the channel. It should be noted that the velocity values directly at the walls cannot be obtained by the μPIV system. They have been set to zero manually.

It is obvious, both in Fig. 5.5 and Fig. 5.6, that the electrical field causes movement of

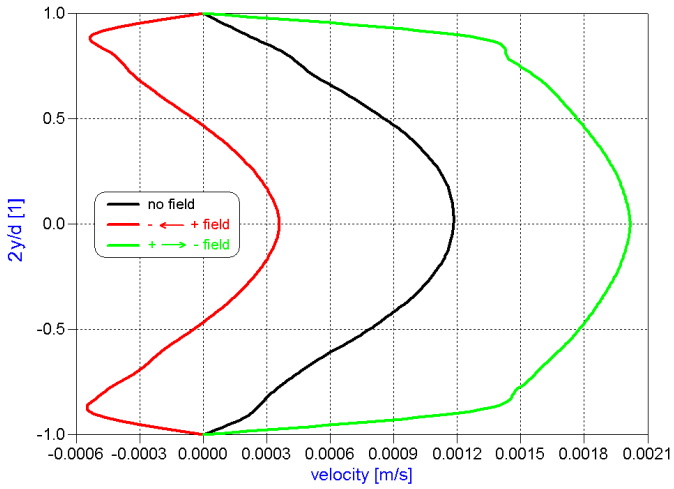

Figure 5.6: Axial velocity profiles of the flow at Re=0.1 at the level 2z/d=0.5 of a straight channel. The black curve relates to the steady flow without electrical field, the red curve is obtained for $E = -14.68\ V/mm$, and the green curve is obtained for $E = +14.68\ V/mm$.

the liquid near the wall in either direction, depending on the direction of the electrical field. The combination of glass and water is characterized by negative electrical charges at the glass surface (wall). These negatively-charged walls accumulate positive charges within the water, i.e. H_3O^+ ions, next to the walls, leading to a positively-charged layer. The application of a positively-directed electrical field causes forces onto these ions, which tend to move these ions (and layers) towards the cathode at the outlet, i.e. in the positive $x-$direction. The opposite direction of the electrical field inverts the forces onto the layer next to the walls and a complex velocity field, directed at the walls to the left and in the middle of the channel to the right, is the consequence.

As we have performed velocity measurements at 15 levels of the microchannel in the range of $-1 \leq 2z/d \leq 1$, we can moreover present the axial velocities within the complete cross section of the channel. These data are plotted in Fig. 5.7. The pressure-driven flow, given in Fig. 5.7a for $Re = 0.1$, appears parabolic in shape, to good approximation symmetric with regard to both axes, and features a maximum velocity in the center of the channel of about 1.7 mm/s. The application of the electrical field $E = -14.68\ V/mm$ results in the flow, given in Fig. 5.7b. We recognize again a profile, symmetric to both axes, with negative velocities at the walls and a center velocity of about $1mm/s$. A closer inspection of the wall regions reveals that particularly within the corners the electroosmotic flow is more pronounced than in the middle of the walls. This certainly is caused by a thicker, positively-charged layer of liquid within the corners. The application of the field $E = +14.68\ V/mm$, finally, results in the flow, given in Fig. 5.7c. The axial velocity profile remains symmetric

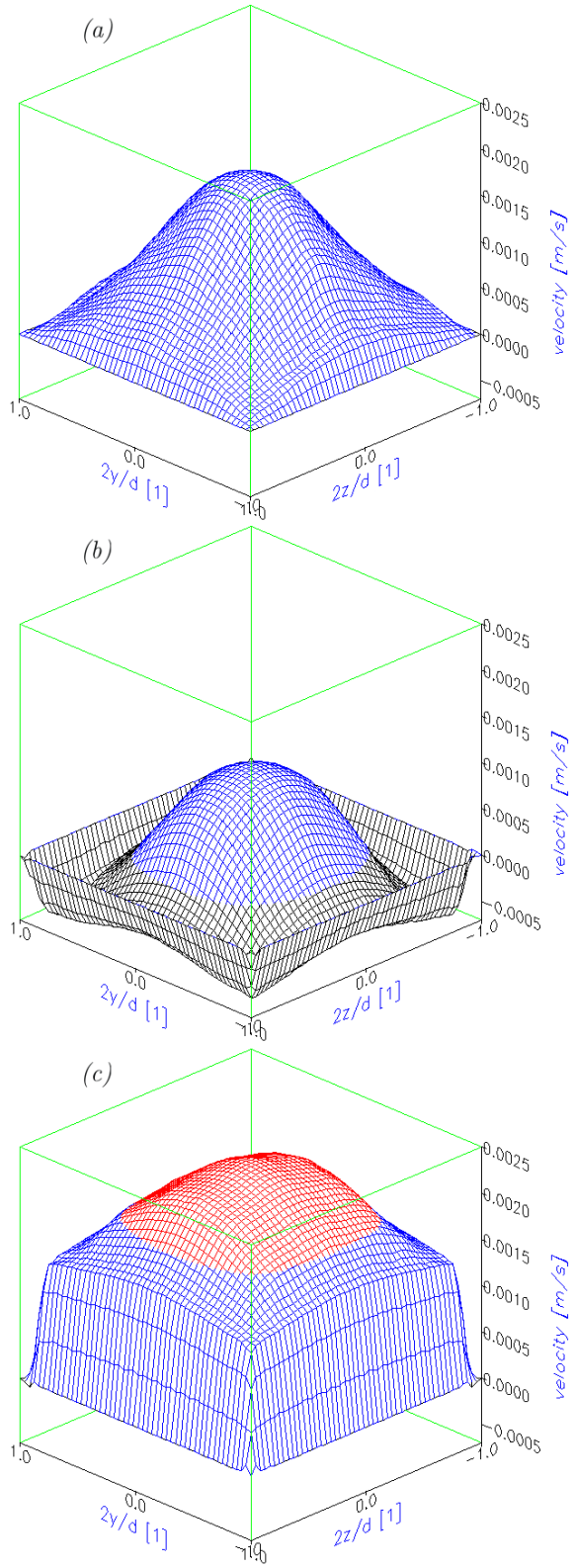

Figure 5.7: Axial velocity profiles of the flow at Re=0.1 for a straight channel: (a) without electrical field, (b) subject to an electrical field of $E = -14.68\ V/mm$, and (c) subject to an electrical field of $E = +14.68\ V/mm$.

around both axes, with steep velocity gradients at the wall, caused by electroosmosis, and a maximum velocity of about 2.4 mm/s in the center of the channel. The measurement in Fig. 5.7 already suggest that the electroosmotic contribution to the axial velocity field can be extracted by subtracting the velocity field of the pressure-driven flow (Fig. 5.7a) from the velocity fields, obtained in presence of the electrical fields (Fig. 5.7b and c). Indeed, we have extracted two such electroosmotic contributions to the velocity field from the respective differences. The absolute values of both electroosmotic contributions are found to be similar, and therefore we present the mean value of these contributions together in Fig. 5.8. We recognize a plug-type electroosmotic contribution, which slightly dips in the channel center. The amplitude of this electroosmotic contribution is around 0.7 mm/s, taken near the walls.

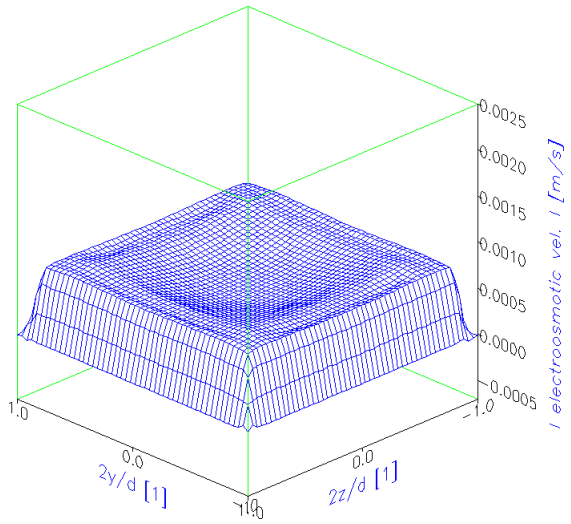

Figure 5.8: Axial mean velocity contribution due to electroosmosis, for $\mid E \mid = 14.68\ V/mm$.

5.2.1 Effects of electrical field strength

From Eq. (2.6) it follows that the amplitude of the electroosmotic velocity is directly proportional to the electrical field strength. Therefore, it is reasonable to investigate the effect of the electrical field strength onto the velocity field. For this purpose we set up a pressure-driven flow with $Re = 0.18$ and superimpose an oscillatory electrical field at a frequency of $0.5Hz$ and amplitudes of 7.23 V/mm, 14.5 V/mm, and 25.0 V/mm. The parameters for the optics and PIV evaluation for this investigation deviate from the parameters defined for section 5.2 in a few points: microscope objective 40×, 30 double frames are taken at the mid-height level ($2z/d = 0$) and are ensemble averaged, the time interval between two

images of a double frame is $\Delta t = 3.5\ ms$. The axial velocity profiles for all cases are given in Fig. 5.9.

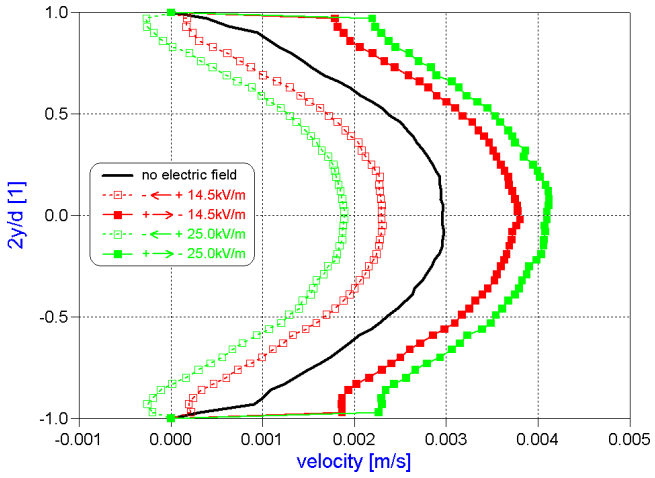

Figure 5.9: Axial velocity profiles of the flow at Re=0.18 (black curve), at the mid-height level ($2z/d = 0$). For a superimposed electrical field, the axial velocity profile oscillates between the green squares (for $E = 25.0\ kV/m$), or between the red squares (for $E = 14.5\ kV/m$).

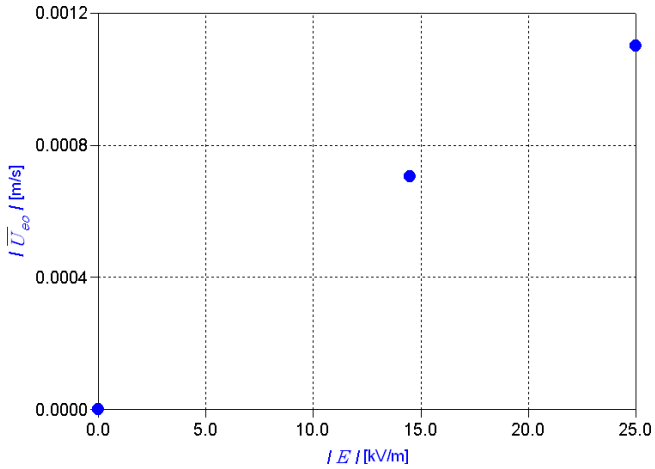

Figure 5.10: Electroosmotic velocity amplitude as function of the electrical field amplitude.

In absence of any electrical field, we measure the profile given as black curve. This profile appears parabolic and is associated with the pressure-driven flow. If we apply a strong electrical field of amplitude $25.0\ V/mm$, oscillating in a square fashion between the positive and negative x-direction, we find the axial velocity profile likewise oscillating between the curves coded with green squares (open/closed). This oscillation of the axial velocity profile

appears to be symmetric around the pressure-driven flow profile (black curve). The weaker field amplitude of 14.5 V/mm causes a weaker oscillation of the velocity profile, between the profiles encoded by red squares (open/closed) in Fig. 5.9. Likewise this oscillation of the axial velocity profile appears to be symmetric around the pressure-driven flow profile (black curve), with clearly reduced amplitude. If we, finally, take the absolute values of the axial velocity oscillation and plot them against the amplitude of the electrical field, we arrive at Fig. 5.10. The data at field strength 14.5 V/mm and 25.0 V/mm are present, as well as a velocity amplitude of zero at zero field strength. The data at reasonable accuracy follow a linear dependency, as predicted by Eq. (2.6).

5.2.2 Effects of pressure-driven flow strength

It is further of interest, how the strength of the pressure-driven flow influences the flow field. The strength of the pressure-driven flow is characterized by the Reynolds number. In these experiments we set up a pressure-driven flow with $Re = 0.0035$, 0.061, and 0.23, and superimpose an oscillatory electrical field at a frequency of $0.5Hz$ and a moderate amplitude of 14.5 V/mm. The parameters for the optics and PIV evaluation for this investigation deviate from the parameters defined for section 5.2 in a few points: microscope objective 63×, 30 double frames are taken at the mid-height level ($2z/d = 0$) and ensemble averaged, the time interval between two images of a double frame is varied, depending on the Reynolds number and electrical field, in the range of $0.3 \leq \Delta t \leq 12$ ms. The axial velocity profiles are summarized in Fig. 5.11.

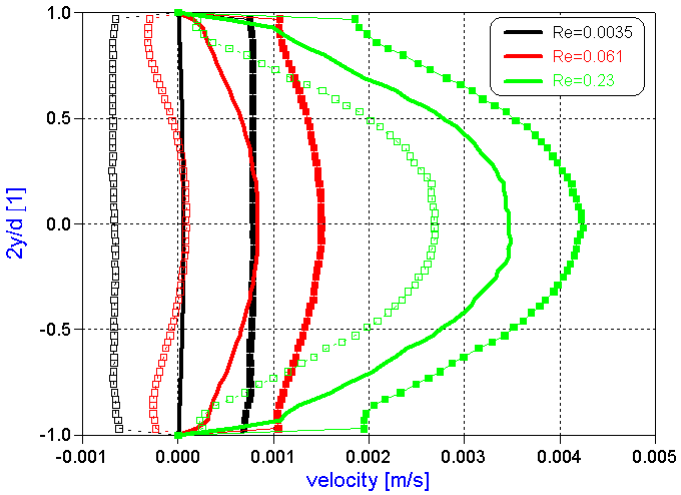

Figure 5.11: Velocity profiles of the flows at Re=0.0035, 0.061, and 0.23, subject to an oscillatory electrical field of amplitude 14.5 V/mm *and frequency* 0.5 Hz.

For a Reynolds number of $Re = 0.23$ we recognize without an electrical field a roughly parabolic profile, as given by the green line in Fig. 5.11. If the oscillatory electrical field is superimposed, the axial velocity profile oscillates between the extremes, given in Fig. 5.11 by open/closed green squares. Again, the extreme velocity profiles due to the electrical field oscillation appear symmetric around the pure pressure-driven flow (green line). If we reduce the Reynolds number, we find the pure pressure-driven flow to retain a roughly parabolic profile with decreasing amplitude (red and black lines). The oscillating electrical field, however, still leads to a symmetric oscillation of the axial velocity profiles (red and black squares) around the respective pressure-driven profiles (red and black curves). The absolute value of the axial velocity oscillations is taken from all three cases and averaged across the channel. The results are plotted in Fig. 5.12 as function of the Reynolds number. As expected, we do not see a significant dependency, as the data suggest a constant value of the electroosmotic velocity amplitude of about 0.72 mm/s. This confirms the superposition principle, i.e. the (variable) pressure-driven flow and the (constant) electroosmotic flow oscillations are independent.

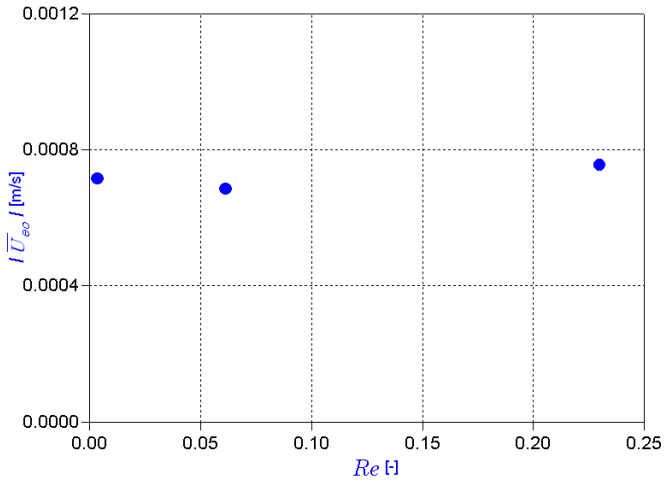

Figure 5.12: Electroosmotic velocity amplitude as function of the Reynolds number.

5.2.3 Effects of oscillating electrical field

Within sections 5.2.1 and 5.2.2 we engaged an oscillating electrical field with an oscillation frequency of 0.5 Hz, superimposed to a pressure-driven flow. The oscillation occurs due to switching between an electrical field in positive and negative $x-$direction, i.e. in a square

fashion. For this oscillation each direction of the electrical field is maintained for 1 s before it is inverted. Here, the question arises, whether the oscillation is slow enough that the flow can adjust to the new field direction. For that reason we have likewise tested a slower oscillation frequency, namely 0.1 Hz. The constant parameters of these investigations are a Reynolds number of $Re = 0.07$ for the pressure-driven flow and an electrical field strength of 58.0 V/mm. Optically, we use the 40× microscope objective, register 40 double frames at a time period of $\Delta t = 2.0$ ms between two images of a double frame, and ensemble averaged these velocity fields. The sampling of the double frames is done at 4 Hz. The results are summarized in Fig. 5.13.

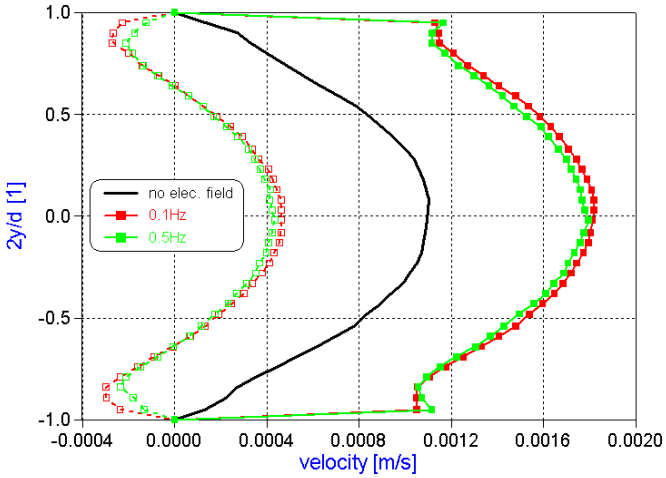

Figure 5.13: Velocity profiles of the flow at Re=0.07 (black curve), subject to an oscillating electrical field of amplitude 58.0 V/mm *and frequency* 0.1 Hz *(red symbols) or* 0.5 Hz *(green symbols).*

From the extreme profiles of the axial velocity oscillation (red and green squares) in Fig. 5.13 we recognize that the flow oscillation around the pressure-driven profile at both frequencies appears almost identical. During the positively-directed electrical field both axial velocity profiles (closed red and closed green squares) are almost identical, apart from very small differences in the channel center. During the negatively-directed electrical field (open red and open green squares), there remain small but distinct differences close to the walls. In essence, for the lower frequency the flow has obviously more time (5 s) to adjust to the actual electrical field, which results in slightly more developed electroosmotic velocity profiles. Nevertheless, the differences are minor and we appear to be far from electrical oscillation frequencies, for which the flow cannot follow the electrical field.

5.3 Electrically-excited flow within the meander

We have in section 5.1 discussed the pressure-driven flow through the meander at various Reynolds numbers. As (Meisel and Ehrhard 2005) have proposed an electrically-excited micromixer with a meander geometry, it is of interest how the flow through the meander is affected by an electrical field. For that reason we run a set of experiments, in which we impose a pressure-driven flow (defined by Re) and superimpose an oscillatory electrical field of amplitude 14.5 V/mm at a frequency of 0.1 Hz. As discussed earlier, the field vector is roughly tangential to the meander channel axis, with a sudden inversion of the direction each 5 s (according to 0.1 Hz). The optical and PIV parameters are chosen as follows: microscope objective 10×, 40 double frames are taken and ensemble averaged, the time interval between two images of a double frame is $\Delta t = 10\ ms$, and the interrogation areas are of size $16 \times 16\ pixels$.

In Fig. 5.14a the streamlines at the level $2z/d = -0.37$ are given for a pure pressure-driven flow with $Re = 0.07$. We recognize a steady flow, tangentially through the meander, with velocities in the channel center reaching 0.55 mm/s. For electrical excitation two electrodes are immersed into the inlets and outlet of the micromixer and a square-shape high-voltage signal is applied. This results in an electrical field vector, which is roughly in the direction of the pressure-driven flow, for the first half of the oscillation period. During the second half of the oscillation period the electrical field vector is inverted, i.e. it is directed against the pressure-driven flow. Multiple measurements, required for ensemble averaging, are taken in-phase with the oscillation, typically synchronized before the switch of polarity. Fig. 5.14b gives the flow field for the electrical field vector pointing in the direction of the pressure-driven flow. We see a flow tangentially, through the meander, which is faster due to the electrical field, if compared to the pure pressure-driven flow (Fig. 5.14a). Velocities in the channel center reach about 1.2 mm/s, which is more than double the value of the pressure-driven flow. The flow field for an electrical field vector directed against the pressure-driven flow is given in Fig. 5.14c. The electrical field for this situation causes forces at the walls (EDL), which are directed against the pressure-driven flow. The liquid movement at the walls in opposite direction, in turn, is responsible for the creation of vortices within the meander (cf. Fig. 5.14c). Such vortices are certainly helpful to improve mixing, as discussed in section 2.2.

The creation of vortices, as obvious in Fig. 5.14c, certainly deserves more attention, since it is highly relevant for the mixing process in such a meander. For that reason, we conduct a more thorough investigation on this situation by applying a greater magnification (microscope objective 20×, $\Delta t = 2\ ms$). We pick a stronger pressure-driven flow with $Re = 0.11$ and superimpose an electrical field of strength 14.5 V/mm, which is directed against the

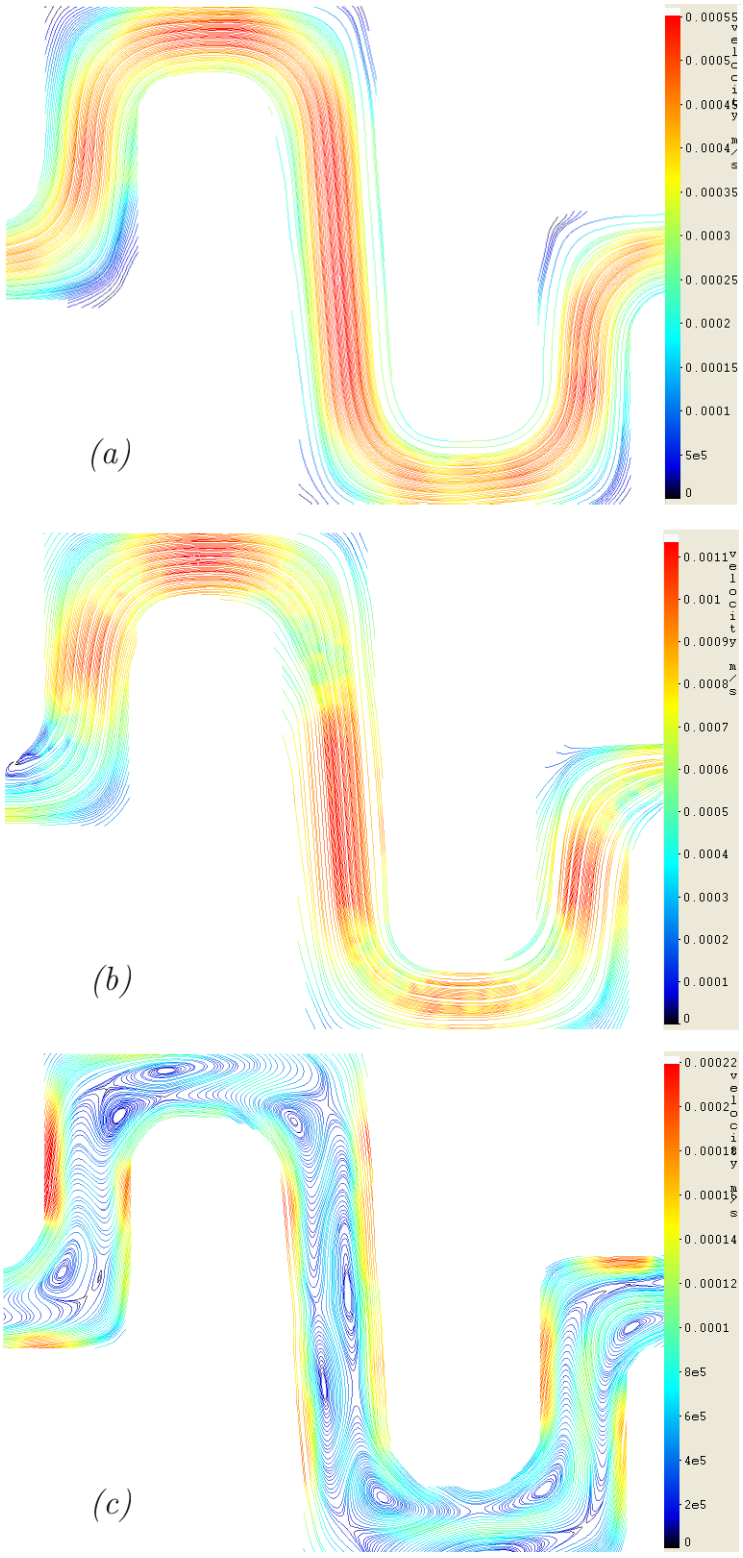

Figure 5.14: Streamlines of (a) a pressure-driven flow for Re=0.07 at level $2z/d = -0.37$. *(b) and (c) are obtained with an additional electrical field of amplitude* $14.5\ V/mm$. *The electrical field is either (b) in the direction of the pressure-driven flow or (c) against the direction of the pressure-driven flow.*

pressure-driven flow. Moreover, we capture the flow field in 15 levels across the complete depth of the microchannel. $-1 \leq 2z/d \leq 1$. In Fig. 5.15 the velocity fields in four different levels are collected. From the mid-height level ($2z/d = 0$), we see in the middle of the channel a flow in direction of the pressure-driven flow, while vortices are present in a narrow zones adjacent to the walls. Going downwards to the level $2z/d = -0.63$, the vortices occupy a much wider zone and the flow in the middle of the channel towards the outlet is hardly visible at this level. Moving even further towards the bottom wall ($2z/d = -0.75, -0.87$), the vortices disappear and the flow is against the direction of the pressure-driven flow everywhere. This observation is coherent with the physics of the electrokinetic flow: since the electrical field vector, and hence electrical forces are directed against the pressure-driven flow, the liquid at all four walls of the channel should move into this direction. Therefore, near to the bottom (or top) wall the electroosmotic flow becomes dominant.

The findings from Fig. 5.15 can be supported by plotting the normal velocity profiles along the line OI for different levels z. These profiles are given in Fig. 5.16. At the mid-height level ($2z/d = 0$) we recognize in the middle of the channel positive velocities, indicating a flow in the direction of the pressure-driven flow. At the walls a layer of negative velocities is obvious, i.e. a flow directed against the pressure-driven flow. There is a distinct difference between the inner (I) and the outer (O) wall region: the inner region is narrow with large negative velocities, the outer region is wide with small negative velocities. If we move towards the bottom ($2z/d = -0.12, -0.25$, etc.), we recognize that the flow in the middle with positive velocities gets weaker and finally disappears beyond the level $2z/d = -0.63$. In parallel, the flow with negative velocities at the walls becomes stronger. Close to the bottom level ($2z/d = -0.87$), across the complete channel negative velocities are observed, i.e. a flow in the opposite direction than the pressure-driven flow. In summary, in the mid-height level, both the pressure-driven flow (positive velocities) and the electroosmotic flow (negative velocities) interact. Close to the bottom (or top) wall, however, the situation is dominated by the electroosmotic flow (with negative velocities).

The flow topology, in general, can be understood from the location of singular points, such as e.g. vortex points or saddle points. If we inspect the right bend in Fig. 5.15 (region $I - O$) in level $2z/d = 0$, we can identify both a vortex (vortex point in the center) and a saddle point. The vortex point is located close to the inner wall (close to I) and the saddle point is located close to the outer wall (close to O).

A principle sketch of the situation is given in Fig. 5.17. An inspection of the flow field at different levels in Fig. 5.15 reveals that both the vortex point and the saddle point change location from level to level, and even disappear. We have extracted this information on the singular points from our velocity measurements at all levels and present the results in Fig.

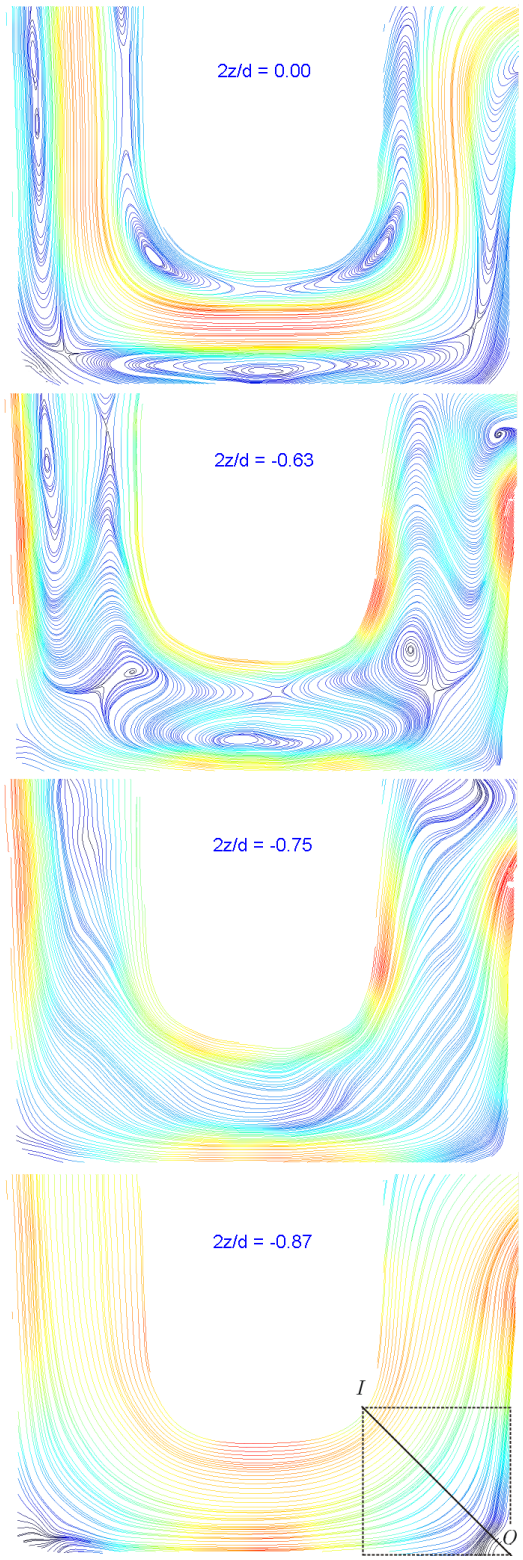

Figure 5.15: Streamlines of the flow at Re=0.11 and an electrical field of amplitude 14.5 V/mm *at levels* $2z/d = 0.00, -0.63, -0.75,$ *and* -0.87. *The electrical field is directed against the pressure-driven flow.*

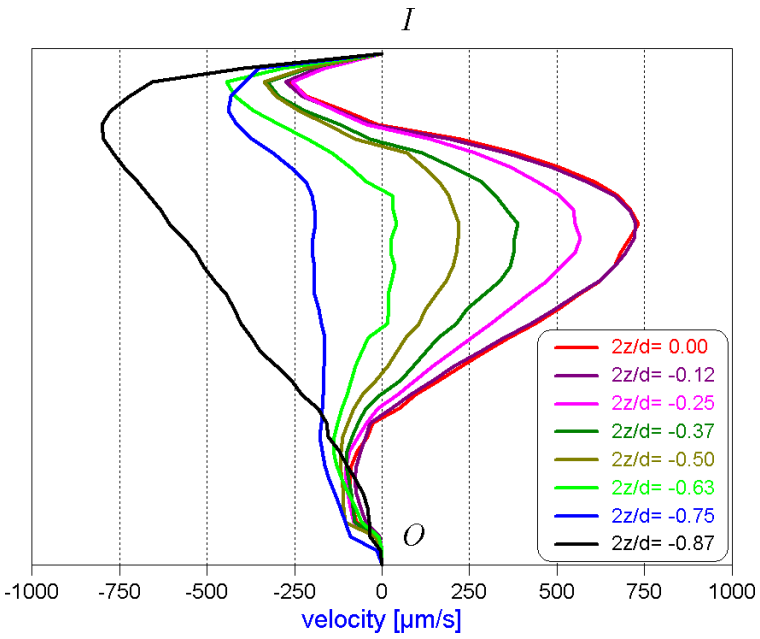

Figure 5.16: Velocity profiles at various levels z for Re=0.11, and an electrical field of amplitude $E = 14.5\ V/mm$. The electrical field is directed against the pressure-driven flow.

5.18. In the identical view as in Fig. 5.17 ($x-y$ plane), we see both the vortex point (closed circle) and the saddle point (closed square) located close to the walls at the mid-height level ($2z/d = 0$). As we move towards the bottom ($2z/d = -0.12, -0.25$, etc.), both singular points move essentially inwards until they disappear beyond $2z/d = -0.63$. The movement of both singular points from the wall regions into the middle with decreasing z is likewise visible in the $x-z$ plane. Again, for $2z/d < -0.63$ neither a vortex point nor a saddle point is found.

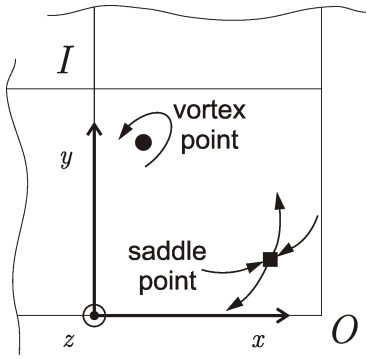

Figure 5.17: Flow topology in the bend region, characterized by a vortex point and a saddle point.

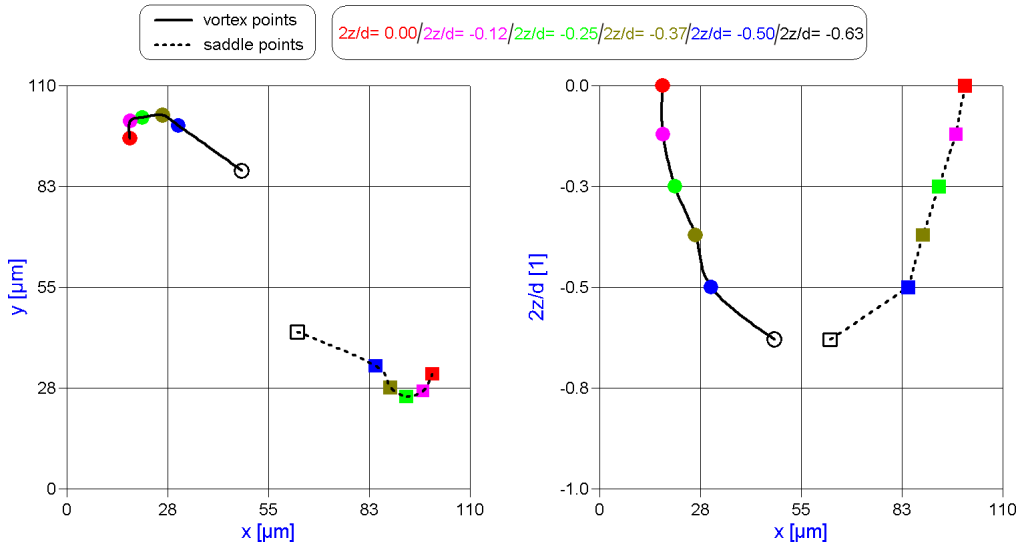

Figure 5.18: Location of singular points, i.e. vortex point (closed circles) and saddle point (closed squares), in the bend. Upon a pressure-driven flow (Re=0.11) an electrical field of 14.5 V/mm *is superimposed, directed against the pressure-driven flow.*

5.4 Mass transport through the electrically-excited micromixer

The flow field investigations, presented for the electrically-excited flow within the meander in section 5.3, certainly provide valuable information. For a judgment on the overall mixing performance of the device, however, a detailed study of the mass transport, and hence the concentration field is necessary. Therefore, we use the μLIF measuring technique, outlined in section 4.4, to obtain information on the height-averaged concentration field within the complete micromixer. The channel and most parameters are chosen identical as for the flow investigations in section 5.3. In detail, we use the glass micromixer with $X = 130\ \mu m$ (cf. section 3.2) and establish gravity-driven flows of identical flow rates through both inlets. The liquids are deionized water and a solution of Rhodamine B in deionized water at a concentration of 0.21 g/l. The optical parameters are: microscope objective 5×, sampling of images is done at 4 Hz, and and exposure time is 2 ms. Two (averaged) images, namely for pure water ($\overline{I}_{min}$) and for the pure Rhodamine B/water solution ($\overline{I}_{max}$) are recorded prior to the measurements, to allow for the computation of the normalized fluorescence intensity G, defined by Eq. (4.32). These calibration images are both based on the ensemble average of 15 single images.

We shall, firstly, concentration on the mixing in absence of the electrical field. The normalized fluorescence intensity G for such a gravity-driven flow at $Re = 0.1$ is given in Fig. 5.19. We recognize at this small Reynolds number considerable mixing, as both liquids

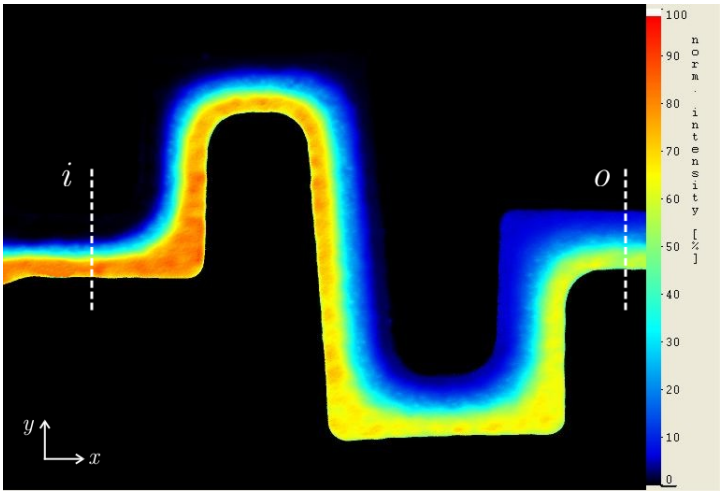

Figure 5.19: Normalized fluorescence intensity for the flow at Re=0.1, without electrical excitation.

flow through the meander. The concentration contrast, present at the inlet (line i), clearly reduces towards the outlet (line o). To quantify mixing through the meander, we extract profiles of the normalized fluorescence intensity G along line i and line o, and use Eq. (4.34) to convert to concentration. For more reliable profiles, we average three rows of pixels during this extraction. The resulting concentration profiles in the center region of the channel are given in Fig. 5.20. Again, we recognize that the concentration gradient is degraded as the liquids move from the inlet (red symbols) to the outlet (green symbols).

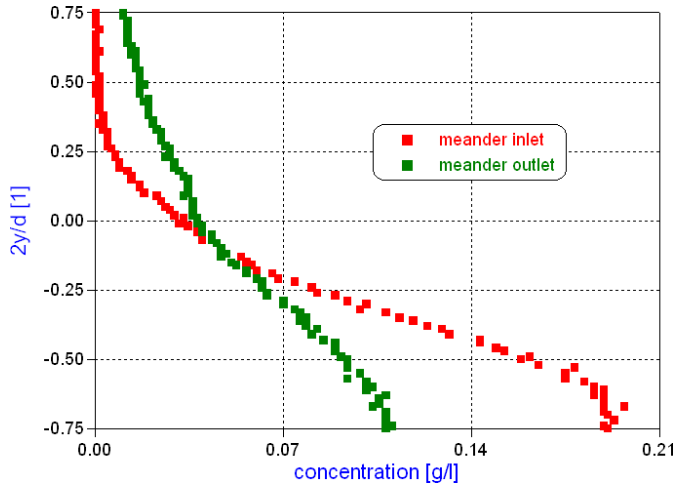

Figure 5.20: Concentration profiles at the meander inlet (line i, red) and the meander outlet (line o, green) for a gravity-driven flow at Re=0.1.

At this point it appears useful to introduce an objective measure for mixing. Following e.g. (Stroock and McGraw 2004), we use a measure based on the standard deviation from the ideal mixture, namely

$$\eta_M = \frac{1}{n}\sum_{i=1}^{n}\{1 - \frac{\sqrt{(C_i - 0.5)^2}}{0.5}\}. \tag{5.1}$$

We term η the mixing quality. The value of η is in the range $0 \leq \eta \leq 1$, whereas $\eta = 0$ is associated with no mixing and $\eta = 1$ is associated with perfect mixing. The summation is taken over n data points of the respective profile, e.g. over the inlet or the outlet profile in Fig. 5.20. For the inlet profile in Fig. 5.20 we find $\eta_i = 0.23$; for the outlet profile we find $\eta_o = 0.48$. This means that the mixing quality η has been improved substantially due to the presence of the meander, even at forced-flow conditions.

In the next step we apply an oscillatory electrical field of amplitude 14.5 V/mm and frequency 0.1 Hz, while we maintain the forced flow at $Re = 0.1$. This flow with identical parameters has been investigated in section 5.3 with regard to the flow field. Similarly as for the flow field, we expect an oscillation of the concentration field, caused by the oscillatory electrical field. Two instantaneous fields of the normalized fluorescence intensity G, depicted during one period of oscillation, are given in Fig. 5.21.

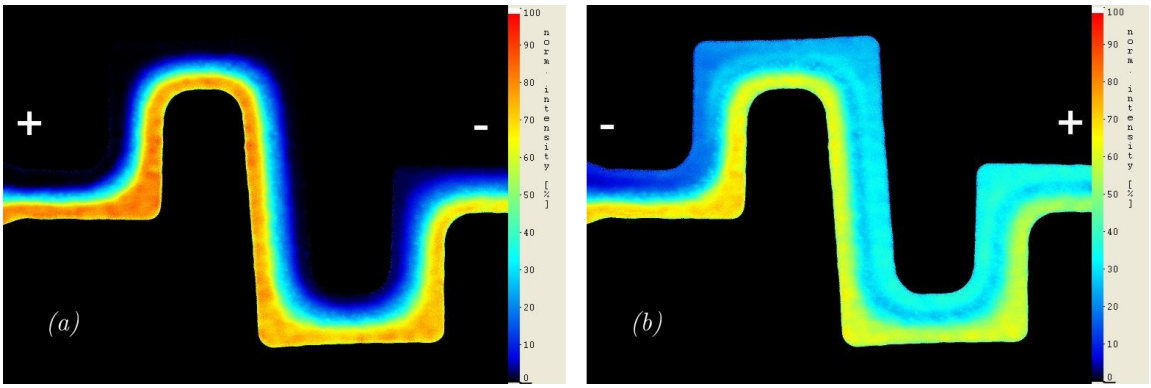

Figure 5.21: Normalized fluorescence intensity for the forced flow with Re=0.1 at an applied electrical field of (a) $E = +14.5\ V/mm$ and (b) $E = -14.5\ V/mm$.

Fig. 5.21a is taken at the end of the first half period, during which a positively-directed electrical field, $E = +14.5\ V/mm$, is applied. Fig. 5.21b is taken at the end of the second half period, at an electrical field of $E = -14.5\ V/mm$. We recognize, that particularly during the period of an electrical field directed against the forced flow (Fig. 5.21b), the fluorescence contrast is clearly reduced. A reduced fluorescence contrast is, of course, related to improved mixing.

The above observation can be cast quantitatively by extracting the inlet and outlet profiles of concentration, at two instances of one period of excitation. These profiles are summarized in Fig. 5.22. Firstly, we recognize that the electrical field even modifies the inlet concentration field upstream of the meander: the inlet profile oscillates between the curves marked by red open and closed squares. Secondly, the outlet profile oscillates between the curves marked by green open and closed squares, indicating an improved homogeneity of concentration downstream of the meander.

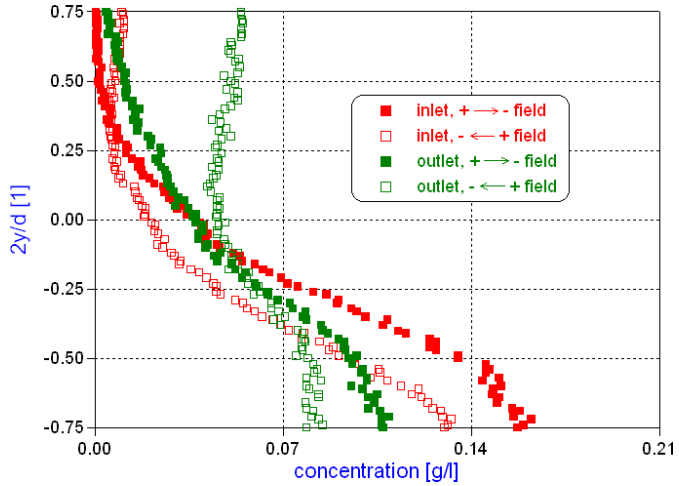

Figure 5.22: Concentration profiles at the meander inlet (line i, red) and at the meander outlet (line o, green) for a gravity-driven flow at Re=0.1 and electrical excitation. The profiles are taken during $E = +14.5\ V/mm$ (closed symbols) and $E = -14.5\ V/mm$ (open symbols) of the oscillation (Fig. 5.21).

The instantaneous values of mixing quality give $\eta_{op} = 0.45$ during $E = +14.5\ V/mm$ (closed green squares) and $\eta_{on} = 0.67$ during $E = -14.5\ V/mm$ (open green squares). Particularly the value η_{on}, obtained during the period of a negatively-directed electrical field (against the forced flow), indicates a significantly-improved mixing. It should be kept in mind, however, that all above fields, profiles and values of mixing quality present instantaneous information.

For a complete judgment on the mixer performance at electrical excitation, it appears useful to infer the time-averaged mixing quality, since the instantaneous mixing quality is of limited value only. For that reason we extract the time-dependent concentration profiles at the meander outlet, resolved in time steps $\Delta t = 0.25\ s$. A selection of such profiles for both half periods of excitation is presented in Fig. 5.23. The time information given for the profiles is relative to the moment, at which the electrical field switches to $E = -14.5\ V/mm$. In Fig. 5.23a we see the response of the concentration profile at the meander outlet to this change of polarity. The induced secondary flow causes a homogenization of the profile, which needs

about 3 seconds to develop. After this transition, the outlet profiles remain unchanged for the rest of the first half period of excitation. The electrical field then switches polarity to $E = +14.5\ V/mm$ at $t = 5\ s$. Again, it takes about 2 seconds before the concentration profile develops towards a less homogeneous form, as can be seen in Fig. 5.23b, and for the rest of this second half period no further change of the concentration profile is observed. The process repeats after 10 seconds, as soon as the electrical field changes polarity again.

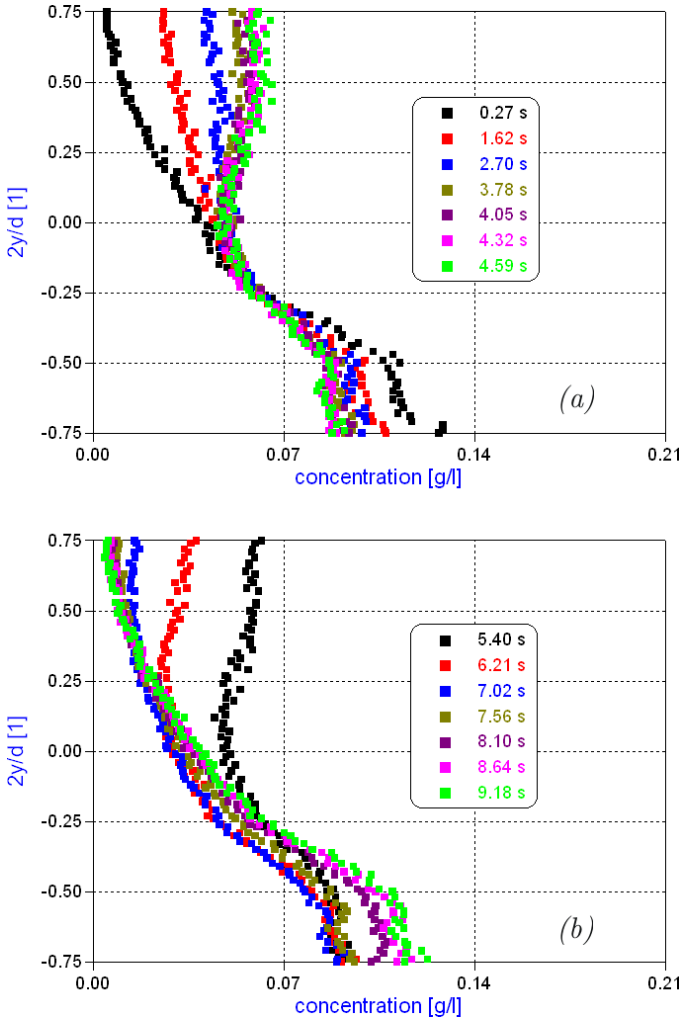

Figure 5.23: Concentration profiles at the meander outlet as function of time for one period of electrical excitation. The parameters are Re=0.1, (a) $E = -14.5\ V/mm$, (b) $E = +14.5\ V/mm$, the frequency of oscillation is $0.1\ Hz$.

Based on all concentration profiles during one period of excitation, we infer values for the mixing quality, which are averaged subsequently. From that procedure we find the time-averaged mixing quality at the outlet to be $\overline{\eta}_o = 0.55$. This means a significant improvement of the mixing quality due to electrical excitation. For comparison, the mixing quality due

to the forced flow is $\eta_o = 0.48$.

applied flow	η_i (inlet)	η_o (outlet)
forced flow	0.23	0.48
$E = +14.5\ V/mm$ (instantaneous)	—	0.45
$E = -14.5\ V/mm$ (instantaneous)	—	0.67
$\mid E \mid = 14.5\ V/mm$ (time-averaged)	—	0.55

Table 5.1: Mixing quality for various situations.

We summarize by collecting the values obtained for the mixing quality in table 5.1. While the gravity-driven flow through the meander achieves an increase of mixing quality of $\Delta\eta = 0.25$, with electrical excitation we obtain (time averaged) an increase of $\Delta\eta = 0.32$. This presents an improvement of 28% due to the electrical excitation. This evaluation, therefore, proves the principle of an electrically-excited micromixer to be useful and effective.

Chapter 6

Summary and outlook

The present work aims to experimentally validate the predictions for the flow and mass transport in an electrically-excited micromixer. Such a micromixer has been proposed by (Meisel and Ehrhard 2005), based on an appropriate model and on numerical simulations. The basic idea of such a micromixer is to induce electroosmotic forces within the electrical double layer to excite a secondary flow. This requires, firstly, a liquid containing charges (e.g. ions), and secondly, electrically-insulating channel walls. Thirdly, an external oscillating electrical field has to be applied. For the validation, obviously, the predicted quantities, namely velocity and concentration fields, need to be measured. This presents a real challenge for microchannels of typically a few ten microns channel width. Integral quantities as volumetric flow rate, pressure drop, or exit composition of the micromixer, although valuable to measure, are certainly not sufficient for validation purposes.

For the measurement of the local quantities, namely for the flow field and for the concentration field, we engage the available method of micro particle image velocimetry (μPIV) and develop the micro laser-induced fluorescence (μLIF) method. Both methods are carefully validated for well-known velocity and concentration fields. For the velocity field data we ensure a typical accuracy of ± 5 % at a spatial resolution of 4 μm. For the height-averaged concentration field, measurement accuracy is around ± 6 % at a spatial resolution down to 0.5 μm. Finally, we engage time-resolved precision weighting to measure the volumetric flow rate at an accuracy (due to evaporation) of better than 20 nl/s. The applied measuring techniques provide two components of the velocity field (μPIV), for the entire volume of liquid. For that purpose the μPIV is applied via the depth of field in different levels of the cross section. The measuring volume in the third direction has a thickness of down to 5 μm. Further, the height-averaged concentration field (μLIF), resolved in two dimensions, is obtained. All measurements are taken time-resolved at time-steps of down to 0.25 s.

For pure forced flow through the meander part of the micromixer, we find particularly for large Reynolds numbers that the concentration field appears strongly influenced by secondary flows. A more detailed study of the flow field clarifies that Dean vortices behind each bend are responsible for this effect. Such Dean vortices, however, are restricted to the range of large Reynolds numbers.

Turning to the electrically-excited flow within the straight channel part of the micromixer, we have been able to measure electroosmotic flow profiles within the complete cross section. For the electroosmotic forces acting in the direction of the forced flow, the flow appears strongly accelerated towards the outlet. For the electroosmotic forces acting against the forced flow, we find backwards flow at the walls and flow towards the outlet in the channel center. All electroosmotic effects are observed in a very thin layer at all walls, whereas velocity profiles within these layers (of several ten nanometer thickness) cannot be resolved. Instead, the first measurement point from the wall shows the integral effect of these layers. For this straight channel part we further demonstrate the effect of the electrical field strength, of the pressure-driven flow strength, and of the oscillation frequency. In detail, the electrical field strength increases the amplitude of the electroosmotic flow, the pressure-driven flow has no effect onto the electroosmotic flow, and oscillation frequencies below $0.5\ Hz$ are slow enough for the flow to follow.

Further, we investigate the electrically-excited flow through the meander, again by velocity measurements within the complete cross section. Within the mid-height plane both the forced flow towards the outlet and the electroosmotic flow in opposite direction are observed. Close to both the bottom and top walls, however, the flow is dominated by electroosmotic effects and the forced flow cannot be observed. The flow structure in a single bend can be characterized by means of one vortex point and one saddle point, which can be followed through the complete cross section. Based on the time-dependent and height-averaged concentration fields, we infer a quantitative measure for mixing quality. Comparing the values at the mixer inlet ($\eta_i = 0.23$) and, time-averaged, at the mixer outlet ($\overline{\eta_o} = 0.55$), we can demonstrate that in comparison to a forced flow the increase of the mixing quality is improved by about 30 %. To derive such a time-averaged measure for mixing quality, it is necessary to compute mixing quality from time-dependent outlet profiles of the concentration fields for one complete period of excitation.

Our experiments - of course - suffer from several imperfections. Firstly, we measure by μLIF a height-averaged concentration field. This averaging along the optical path, certainly, is problematic if layers of different concentrations are present along the optical path. Here, the arrangement of confocal microscopy, which presents a non-trivial modification of the μLIF method, would give substantial improvement. Based on such a method, the concen-

tration field within the entire cross section could be measured. Secondly, our experiments in two important aspects differ from the simulations by (Meisel and Ehrhard 2005): (a) The electrical field in the experiments is spanned up between the electrodes in the inlet and the outlet reservoirs, while (Meisel and Ehrhard 2005) use an ideal parallel electrical field. (b) Within the experiments electroosmosis appears at all four walls of the channel, while within the two-dimensional simulations the top and bottom walls are ignored. For that reason a quantitative comparison, hence a validation, is not really possible at the moment. For this purpose it appears necessary to run simulations, exactly suitable for the experimental situation. This includes the computation of the complete electrical field, as well as fully three-dimensional flow and concentration fields.

Several conclusions may be drawn with regard to a further optimization of the discussed micromixer. One route points towards an arrangement of multiple meanders in series, which certainly will increase mixing quality further. Here, the optimization of the meander distance plays an important role, in particular if spatial or temporal resonance is envisioned. A second route points towards an alternating flow through either of the inlet channels, which should result in further interfaces between separated liquid plugs. Given the electrodes positioned within the inlet and outlet reservoirs, such an alternating flow can be easily excited by fixing the outlet potential (e.g. negative) and by connecting the inlet potential (e.g. positive) to one of the two electrodes in the inlet reservoirs, alternating in time.

Chapter 7

Note of thanks

I graciously thank my supervisor Prof. Dr.-Ing.habil. Peter Ehrhard for his extensive and energetic support, as well as his persistent readiness for discussion during my PhD studies. I thank Prof. Dr.rer.nat. V. Saile for accepting the responsibility as the second examiner and also for his readiness to discuss and guide this research. I'd like to thank Prof. Dr.-Ing. H.-J. Bauer for accepting the task as examination chairman. Especial thank you goes to entire of my family, my dearest parents and all brother and sisters in *Takye Hazrat Khidr* for their faith in me, and for giving me strength and love. I also thank my dear wife for her incredible patient and encouragement.

Bibliography

Adamson, A. W. and Gast, A. P.: 2004, *Physical Chemistry of Surfaces*, John Wiley and Sons, Inc.

Adrian, R. J.: 1991, Particle image techniques for experimental fluid mechanics, *Ann Rev Fluid Mech.* **23**, 261–304.

Auroux, P. A., Iossifidis, D., Reyes, D. R. and Manz, A.: 2002, Micro total analysis systems. 2. analytical standard operations and applications, *Journal of Analytical Chemistry* **74**, 2637–2652.

Bakker, A., LaRoche, R. D. and Marshall, E. M.: 1998, *Modelling of the Turbulent Flow in HEV Static Mixers, The online CFD book*.

Beale, S. C.: 1998, Capillary electrophoresis, *Journal of Analytical Chemistry* **70**, 279R–300R.

Bertsch, A., Heimgartner, S., Cousseau, P. and Renaud, P.: 2001, 3D micromixers-downscaling large scale industrial static mixers, *Proc. IEEE MEMS Workshop*, Interlaken, Switzerland, 507–510.

Bindhu, C. V. and Harilal, S. S.: 2001, Effect of the excitation source on the quantum yield measurements of Rhodamine B laser dye studied using thermal-lens technique, *Anal. Science* **17**, 141–144.

Blakebrough, N.: 1967, *Biochemical and Biological Engineering Science, Vol. 1*, Academic Press.

Bottausci, F., Cardonne, C., Mezic, I. and Meinhart, C.: 2003, An actively controlled micromixer: 3-D experiments and simulations, *The APS 56th annual meeting*, NYC/New Jersey.

Branebjerg, J., Gravesen, P., Krog, J. P. and Nielsen, C. R.: 1996, Fast mixing by lamination, *Proc. IEEE MEMS Workshop*, San Diego, CA, 441–446.

Campbell, C. J. and Grzybowski, B. A.: 2004, Microfuidic mixers: from microfabricated to self-assembling devices, *Philosophical Transactions of the Royal Society of London. Ser.A* **362**, 1069–1086.

Charrier, J.: 1996, *Polymeric materials and processing: plastics, elastomers, and composites*, Kluwer Academic/Plenum Publishers.

Chaté, H., Villermaux, E. and Chomez, J. M.: 1996, *Mixing: Chaos and Turbulence*, Oxford University Press.

Chiem, N., Colyer, C. and Harrison, J. D.: 1997, Microfluidic systems for clinical diagnostics, *Proc. Int. Solid-State Sens. Actuators Conf.*, Chicago, IL, 183–186.

Cho, S. K. and Kim, C.-J.: 2003, Particle separation and concentration control for digital microfluidic circuits, *Proc. IEEE Micro Electro Mechanical Systems Conf.*, 686–689.

Cho, S. K., Moon, H. and Kim, C. J.: 2003, Creating, transporting, cutting and merging liquid droplets by electrowetting-based actuation for digital microfluidic circuits, *IEEE J. Microelectromech. Syst.* **12**, 70–80.

Choi, J. W. and Ahn, C. H.: 2000, An active micro mixer using electrohydrodynamic (EHD) convection, *Proc. Solid-State Sens. and Actuator Workshop*, Hilton Head Island, SC, 52–55.

Dalziel, S. B., Hughes, G. O. and Sutherland, B. R.: 2000, Method and apparatus for obtaining images and measurements of density fluctuations in transparent media, *Disclosure for U.S. Provisional Patent Application [No. 60/170,928]*.

Deshmukh, A. A., Liepmann, D. and Pisano, A. P.: 2001, Characterization of a micromixing, pumping and valving system, *Proc. 11th Int. Solid-State Sens. and Actuators*, Munich, Germany, 950–953.

Deval, J., Tabeling, P. and Ho, C.-M.: 2002, A dielectrophoretic chaotic mixer, *Proc. IEEE Micro Electro Mechanical Systems Conf.*, Munich, Germany, 36–39.

Ehrfeld, W., Golbig, K., Hessel, V., Lowe, H. and Richter, T.: 1999, Characterization of mixing in micromixer by a test reaction: Single mixing units and mixer arrays, *Industrial and Engineering Chemistry Research* **38**, 1075–1082.

Einstein, A.: 1905, On the movement of small particles suspended in a stationary liquid demanded by the molecular-kinetic theory of heat, *in* A. Einstein (ed.), *Theory of Brownian Movement*, New York: Dover.

Espinosa-Solares, T., Brito-De la Fuente, E., Tecante, A., Medina-Torres, L. and Tanguy, P.: 2002, Mixing time in rheologically evolving model fluids by hybrid dual mixing systems, *7th UK Conference on mixing*.

Evans, J., Liepmann, D. and Pisano, A. P.: 1997, Planar laminar mixer, *IEEE Proc. MEMS*, Piscataway, NJ.

Fan, S.-K., Hashi, C. and Kim, C.-J.: 2003, Manipulation of multiple droplets on N×M grid by cross-reference EWOD driving scheme and pressure contact packaging, *Proc. IEEE Micro Electro Mechanical Systems Conf.*

Fletcher, P., Haswell, S. and Zhang X.: 2003, Monitoring of chemical reactions within microreactors using an inverted Raman microscopic spectrometer, *Electrophoresis* **24**, 3239–3245.

Floyd, T. M., Schmidt, M. A. and Jensen, K. F.: 2001, A silicon microchip for infrared transmission kinetics studies of rapid homogeneous liquid reactions, *Proc. Micro Total Analysis Systems*, The Netherlands, 277–279.

Fogler, H.: 1993, *Elements of chemical reaction engineering*, Prentice Hall.

Freitag, A., Dietrich, T. and Scholz, R.: 2000, Glass as a material for microreaction technology, *Proc. of IMRET 4, Topical Conference*, 48–54.

Fuhr, G., Schnelle, T. and Wagner, B.: 1994, Travelling wave-driven microfabricated electrodynamic pumps for fluids, *Journal of Micromechanics and Microengineering* **4**, 217–226.

Gaskey, S., Vacus, P., David, R., Villermaux, J. and André, J.: 1990, A method for the study of turbulent mixing using fluorescence spectroscopy, *Experiments in Fluids* **9**, 137–147.

Gendrich, C. P., Koochesfahani, M. M. and Nocera, D. G.: 1997, Molecular tagging velocimetry and other novel applications of a new phosphorescent supramolecule, *Experiments in Fluids* **23**, 361–372.

Hari-Prajitno, D.: 1999, *An experimental study of single, double and triple wide-blade hydrofoil impellers: power and homogenisation characteristics, PhD thesis*, The University of Birmingham, UK.

Hatch, M. S., Sowa, W. A., Samuelson, G. S. and Holdeman, J. D.: 1995, Geometry and flow influences on jet mixing in cylindrical ducts, *Journal of Propulsion and Power* **11**, 402.

Heckele, M., Bacher, W. and Müller, K. D.: 1998, Hot embossing -the molding technique for plastic microstructures, *Microsystem Technologies* **4**, 122–124.

Henry, A. C., Waddell, E. A., Shreiner, R. and Locascio, L. E.: 2002, Control of electroosmotic flow in laser-ablated and chemically modified hot imprinted poly (ethylene terephthalate glycol) microchannels, *Electrophoresis* **23**, 791–798.

Hinsamann, P., Frank, J., Svasek, P., Harasek, M. and Lendl, B.: 2001, Design, simulation and application of a new micromixing device for time resolved infrared spectroscopy of chemical reactions in solution, *Lab on a chip* **1**, 16–21.

Holden, M., Kumar, S., Castellana, E., Beskok, A. and Cremer, P.: 2003, Generating fixed concentration arrays in a microfluidic device, *Sensors and Actuators B* **92**, 199–207.

Holden, P., Wang, M., Mann, R., Dickin, F. J. and Edwards, R. B.: 1998, Imaging stirred-vessel macromixing using electrical resistance tomography, *AIChE Journal* **44**, 780.

Hong, C. C., Choi, J. W. and Ahn, C. H.: 2004, A novel in-plane passive microfluidic mixer with modified tesla structures, *Lab on a chip* **4**, 109–113.

Hong, S., Thiffeault, J. L., Fréchette, L. and Modi, V.: 2003, Numerical study of mixing in microchannels with patterned zeta potential surfaces, *Proc. IMECE*, Washington.

Hosokawa, K., Fujii, T. and Endo, I.: 1999, Droplet-based nano/picoliter mixer using hydrophobic microcapillary vent, *Proc. IEEE MEMS Workshop*, Orlando, FL, 388–393.

Houcine, H., Vivier, H., Plasari, E., David, R. and Villermaux, J.: 1996, Planar laser induced fluorescence technique for measurements of concentration fields in continuous stirred tank reactor, *Experiments in Fluids* **22**, 95–102.

Hu, H. and Koochesfahani, M. M.: 2002, A novel method for instantaneous, quantitative measurement of molecular mixing in gaseous flows, *Experiments in Fluids* **33**, 202–209.

Hughes, M. P., Morgan, H. and Rixon, F. J.: 2001, Dielectrophoretic manipulation and characterization of herpes simplex virus-1 capsids, *European Biophysics Journal* **30**, 268–272.

Inoué, S. and Spring, K. R.: 1997, *Video Microscopy: The Fundamentals*, Plenum Publisher.

Jen, C. P., Wu, C. Y., Lin, Y. C. and Wu, C. Y.: 2003, Design and simulation of the micromixer with chaotic advection in twisted microchannels, *Lab on a chip* **3**, 77–81.

Kakuta, M., Bessoth, F. G. and Manz, A.: 2001, Microfabricated devices for fluid mixing and their application for chemical synthesis, *The Chemical Record* **1**, 395–405.

Kateman, G. and Buydens, L.: 1993, *Quality Control in Analytical Chemistry*, John Wiley and Sons, Ltd.

Kling, K. and Mewes, D.: 2003, Visualization of micro- and macromixing in liquid mixtures of reacting components, *Proc. of the 4th ASME-JSME Joint Fluids Engineering Conference*, USA, FEDSM2003–45216.

Knight, J.: 2002, Honey, i shrunk the lab, *Nature* **418**, 474–475.

Knight, J. B., Vishwanath, A., Brody, J. P. and Austin, R. H.: 1998, Hydrodynamic focusing on a silicon chip: Mixing nanoliters in microseconds, *Physical Review Letters* **80**, 3863–3866.

Koochesfahani, M. M. and Dimotakis, P. E.: 1986, Mixing and chemical reactions in a turbulent liquid mixing layer, *Journal of Fluid Mechanics* **170**, 83–112.

Kramers, H., Baars, G. M. and Knoll, W. H.: 1953, A comparison study on the rate of mixing in stirred tank, *Chemical Engineering Science* **2**, 35–42.

Kuo, K.: 1986, *Principles of Combustion*, John Wiley and Sons, Ltd.

Lee, Y. K., Deval, J., Tabling, P. and Ho, C. M.: 2001, Chaotic mixing in an electrokinetikally and pressure driven micro flow, *Proc. IEEE MEMS Workshop*, Interlaken, Switzerland.

Lee, Y. K., Tabling, P., Shih, C. and Ho, C. M.: 2000, Characterization of a mems-fabricated mixing device, *Proc. MEMS*, New York.

Legge, C.: 2001, Lab-on-a-chip: scaling down, *Chemical Engineering*.

Liu, Y. Z., Kim, B. J. and Sung, H. J.: 1993, Two-fluid mixing in microchannel, *International Journal of Heat and Fluid Flow*.

Lu, L., Ryu, K. and Liu, C.: 2002, A magnetic microstirrer and array for microfuidic mixing, *Journal of Microelectromechanical Systems* **11**, 462–469.

Maruyama, T., Suzuki, S. and Mizushina: 1981, Pipeline mixing between two fluid streams meeting at a T-junction, *Int. Chem. Eng.*

Matsumoto, R., Farangis Zadeh, H. and Ehrhard, P.: 2005, Quantitative measurement of depth-averaged concentration fields in microchannels by means of a fluorescence intensity method, *Experiments in Fluids*, in press.

Meinhart, C. D., Wereley, S. T. and Santiago, J. G.: 1999, PIV measurements of a microchannel flow, *Experiments in Fluids* **27**, 414–419.

Meinhart, C. D., Wereley, S. T. and Gray, M. H. B.: 2000a, Volume illumination for two-dimentional particle image velocimetry, *Meas. Sci. Tech.* **11**, 809–814.

Meinhart, C. D., Wereley, S. T. and Santiago, J. G.: 2000b, Micro-resolution velocimetry techniques, *Laser Techniques Applied to Fluid Mechnics*, *in* R. J. Adrian. et al. (ed.), Springer-Verlag.

Meinhart, C., Wang, D. and Turner, K.: 2003, Measurement of AC electokinetic flow, *Biomedical Microdevices* **5**, 139–145.

Meisel, I. and Ehrhard, P.: 2005, Electrically-excited (electroosmotic) flows in microchannels for mixing applications, *European Journal of Mechanics-B/Fluids*, in press.

Melcher, J. R. and Firebaugh, M. S.: 1967, Traveling-wave bulk electroconvection induced across a temperature gradient, *Physics of Fluids*.

Melton, L. A., Lipp, C. W., Spradling, R. W. and Paulson, K. A.: 2002, DISMT - determination of mixing time through color changes, *Chemical Engineering Communications* **189**, 322–338.

Mensinger, H., Richter, T., Hessel, V., Döpper, J. and Ehrfeld, W.: 1994, Microreactor with integrated static mixer and analysis system, *Proc. Micro Total Anal. Syst. Workshop*, Enschede, The Netherlands, 237–243.

Mitchell, M. C., Spikmans, V., Bessoth, F., Manz, A. and de Mello, A.: 2000, Toward organic synthesis in microfluidic devices: multicomponent reactions for the construction of compound libraries, *Proc. Micro Total Analysis Systems*, The Netherlands, 463–465.

Miyake, R., Lammerink, T. S. J., Elwenspoek, M. and Fluitman, J. H. J.: 1993, Micro mixer with fast diffusion, *Proc. IEEE MEMS Workshop*, Ft. Lauderdale, FL, 248–253.

Müller, U. and Bühler, L.: 2001, *Magnetofluiddynamics in channels and containers*, Springer.

Moon, H., Cho, S. K., Garrell, R. L. and Kim, C.-J.: 2002, Low voltage electrowetting-on-dielectric, *Journal of Applied Physics*.

Moroney, R. M., White, R. and Howe, R. T.: 1991, Ultrasonically induced microtransport, *Proc. IEEE MEMS Workshop*, Amsterdam, The Netherlands, 277–282.

Nguyen, N. and Werely, S.: 2002, *Fundamentals and applications of microfuidics*, Artech House.

Oddy, M., Santiago, J. and Mikkelsen, J.: 2001, Electrokinetic instability micromixing, *Journal of Analytical Chemistry* **73**, 5822–5832.

Oldshue, J. Y.: 1983, *Fluid mixing technology*, McGraw-Hill.

Olsen, M. G. and Dutten, J. C.: 2003, Planar velocity measurements in a weakly compressible mixing layer, *Journal of Fluid Mechanics* **486**, 51–77.

Ottino, J.: 1988, *The kinematics of mixing: stretching, chaos and transport*, Cambridge University Press.

Park, S. J., Kim, J. K., Park, J., Chung, S., Chung, C. and Chang, J. K.: 2004, Rapid three-dimensional passive rotation micromixer using the breakup process, *Journal of Micromechanics and Microengineering* **14**, 6–14.

Paul, P. H., Garguilo, M. G. and Rakestraw, D. J.: 1993, Imaging of pressure- and electrokinetically-driven flows through open capillaries, *Journal of Analytical Chemistry*.

Plumb, A.: 1993, Atmospheric dynamics. mixing and matching, *Nature* **365**, 489.

Pohl, H.: 1978, *Dielectrophoresis*, Cambridge University Press.

Probstein, R. F.: 2003, *Elements of chemical reaction engineering*, John Wiley and Sons, Inc.

Radovanovic, M.: 1986, Fluidized bed combustion, *Proceedings of the International Centre for Heat and Mass Transfer, 21*.

Ramos, A., Morgan, H., Green, N. G. and Castellanos, A.: 1998, AC electrokinetics: a review of forces in microelectrode structures, *Journal of Physics D: Applied Physics* **31**, 2338–2353.

Ramsey, J. M.: 1999, The burgeoning power of the shrinking laboratory, *Nature Biotech.* **17**, 1061–1062.

Reyes, D. R., Iossifidis, D., Auroux, P. A. and Manz, A.: 2002, Micro total analysis systems. 1. introduction, theory, and technology, *Journal of Analytical Chemistry* **74**, 2623–2636.

Robin, H. L., Stremler, M. A., Sharp, K. V., Olsen, M. G., Adrian, R. J., Santiago J. G., Aref, H. A. and Beebe, D. J.: 2000, Passive mixing in a three-dimentional serpentine microchannel, *Journal of Microelectromechanical Systems* **9**, 190–197.

Rost, F.: 1991, *Quantitative Fluorescence Microscopy*, Cambridge University Press.

Rost, F.: 1992, *Fluorescence Microscopy*, Cambridge University Press.

Santiago, J. G., Wereley, S. T., Meinhart, C. D., Beebe, D. J. and Adrian, R. J.: 1998, A particle image velocimetry system for microfluidics, *Experiments in Fluids* **25**, 316–319.

Schwesinger, N., Frank, T. and Wurmus, H.: 1996, A modular microfluid system with an integrated micromixer, *Journal of Micromechanics and Microengineering* **6**, 99–102.

Stroock, A. D. and McGraw, G. J.: 2004, Investigation of the staggered herringbone mixer with a simple analytical model, *Philosophical Transactions of the Royal Society of London. Ser.A* **362**, 971–986.

Stroock, A. D., Dertinger, S. K., Ajdari, A., Mezic, I., Stone, H. A. and Whitesides, G. M.: 2002, Chaotic mixer for micro channels, *Science* **295**, 647–651.

Suzuki, H. and Ho, C. M.: 2002, A magnetic force driven chaotic micro-mixer, *Proc. 15th Int. Conf. on Micro Electro Mechanical Systems, MEMS'02*, Las Vegas, NV, 40–43.

Truckenmüller, R., Henzi, P., Herrmann, D., Saile, V. and Schomburg, W. K.: 2004, A new bonding process for polymer micro- and nanostructures based on near surface degregation, *The 17th IEEE Inter. Conf. On Micro Electro Mechanical Systems*, Masstricht, NL.

Tsai, J. H. and Lin, L.: 2001, Thermal bubble powered microfluidic mixer with gas bubble filter, *Proc. 11th Int. Solid-State Sens. and Actuators*, Munich, Germany, 966–969.

Veenstra, T. T., Lammerink, T. S. J., Elwenspoek, M. C. and van den Berg, A.: 1999, Characterization method for a new diffusion mixer applicable in micro flow injection analysis systems, *Journal of Micromechanics and Microengineering* **9**, 199–202.

Walker, D.: 1987, A fluorescence technique for measurement of concentration in mixing liquids, *J. Phys. E: Sci. Instrum.* **20**, 217–224.

Walsh, G.: 1998, *Biopharmaceuticals: biochemistry and biotechnology*, John Wiley and Sons, Ltd.

Wang, H., Iovenitti, P., Harvey, E. and Masood, S.: 2003, Numerical investigation of mixing in microchannels with patterned grooves, *Journal of Micromechanics and Microengineering* **13**, 801–808.

Wang, T. H., Wong, P. K. and Ho, C.-M.: 2002, Electrical molecular focusing for laser induced fluorescence based single DNA detection, *Proc.IEEE Micro Electro Mechanical Systems Conf.*, 15–18.

Weigl, B. H., Holl, M. R., Schutte, D., Brody, J. P. and Yager, P.: 1996, Diffusion-based optical chemical detection in silicon flow structure, *Proc. Micro Total Analysis Systems*, Basel, Switzerland, 174–184.

West, A.: 1984, *Solid state chemistry and its applications*, John Wiley and Sons, Ltd.

Woias, P., Hauser, K. and Yacoub-George, E.: 2000, An active silicon micromixer for μTAS application, *Proc. Micro Total Analysis Systems Symp.*, Enschede, The Netherlands, 277–282.

Wong, P. K., Wang, T. H., Deval, J. H. and Ho, C.-M.: 2004a, Electrokinetics in micro devices for biotechnology applications, *IEEE/ASME transactions on mechatronics* **9**, 366–376.

Wong, S. H., Ward, M. C. L. and Wharton, C. W.: 2004b, Micro T-mixer as a rapid mixing micromixer, *Sensors and Actuators B* **100**, 359–379.

Yamaguchi, Y., Takagi, F., Yamashita, K., Nakumura, H., Maeda, H., Sotowa, K., Kusakabe, K., Yamasaki, Y. and Morooka, S.: 2004, 3-D simulation and visualization of laminar flow in a microchannel with hair-pin curves, *AIChE Journal* **50**, 1530–1535.

Yang, R.-J., Fu, L.-M. and Lee, G.-B.: 2002, Variable-volume-injection methods using electrokinetic focusing on microfluidic chips, *Journal of Separation Science* **25**, 996–1010.

Zalc, J. M., Szalai, E. S., Alvarez, M. M. and Muzzio, F. J.: 2002a, Using CFD to understand chaotic mixing in laminar stirred tanks, *AIChE Journal* **48**, 2124–2134.

Zalc, J. M., Szalai, E. S., Muzzio, F. J. and Jaffer, S.: 2002b, Characterization of flow and mixing in an SMX static mixer, *AIChE Journal* **48**, 427–436.

Zeng, S., Chen, C.-H., Jr., J. C. M. and Santiago, J. G.: 2001, Fabrication and characterization of electroosmotic micropumps, *Sensors and Actuators B* **79**, 107–114.

Zhang, S., Schneider, S. P. and Collicott, S. H.: 1995, Quantitative molecular mixing measurements using digital processing of absorption images, *Experiments in Fluids* **19**, 319–327.

Zhu, X. and Kim, E. S.: 1998, Microfluidic motion generation with acoustic waves, *Sensors and Actuators A: Physics* **66**, 355–360.

Resume

Name:	Hamid Farangis Zadeh
Date of birth:	09.22.1969
Place of birth:	Sanandaj, Iran
Nationality:	Iranian (Kurd)
Marital status:	married
Education:	1975-1980
	Milad Elementary School; Sanandaj, Iran
	1980-1983
	Khaghani Guidance School; Sanandaj, Iran
	1983-1987
	Ranjavari High School, Math/Phys; Sanandaj, Iran
	1988-1993
	1st B.Sc. Applied Chemistry, Sharif University of Technology, Teheran, Iran
	1998-2000
	2nd B.Sc. Chemical Engineering, Friedrich Alexander University, Erlangen, Germany
	2000-2001
	M.Sc. Chemical Engineering, Friedrich Alexander University, Erlangen, Germany
	2002-2005
	PhD Mechanical Engineering, University Karlsruhe, Karlsruhe, Germany
Experience:	1995-1998
	Working on measuring systems at Mehr Kanaz Co. , Iran
Languages:	Kurdish, Persian, Arabic, English, German